UNIVERSIDADE FEDERAL DE MINAS GERAIS
DEPARTAMENTO DE FÍSICA

THIAGO HENRIQUE RODRIGUES DA CUNHA

Chemical Vapor Deposition of Graphene at Very Low Pressures

Minas Gerais – Brasil
Outubro - 2014

THIAGO HENRIQUE RODRIGUES DA CUNHA

Chemical Vapor Deposition of Graphene at Very Low Pressures

Tese apresentada à Universidade Federal de Minas Gerais como requisito parcial para a obtenção do grau de Doutor Em Física.

Área de Concentração: Física da Matéria Condensada
Orientador: André Santarosa Ferlauto

Belo Horizonte
Departamento de Física da UFMG
2014

Agradecimentos

Aos meus pais que sempre primaram pela minha educação, me oferecendo oportunidades e incentivo.

Ao meu orientador André Ferlauto pelas palavras lúcidas e de estímulo que contribuíram tanto para o meu amadurecimento profissional quanto pessoal. O desfecho deste trabalho se deve em muito as suas críticas e sugestões.

Ao Sérgio pela atenção e paciência em compartilhar seu vasto conhecimento prático. A qualidade dos resultados apresentados neste trabalho não seria a mesma sem seus conselhos e auxilio.

Aos professores Rodrigo Gribel e Luís Orlando pelas sugestões, apoio e amizade.

À minha companheira Jaqueline pelo carinho, companheirismo e por me inspirar até o desfecho desta tese.

Aos meus amigos de Piumhi, Viçosa e Belo Horizonte, os quais não irei citar aqui por medo de cometer uma injustiça esquecendo de algum nome.

A elaboração desta pesquisa representa uma conquista para mim, principalmente pelo amadurecimento pessoal e intelectual. Ainda que o destino inexorável deste trabalho seja mofar nas estantes da biblioteca da física, gostaria de expressar toda minha gratidão a quem participou, direta ou indiretamente, desta etapa da minha vida.

Contents

List of Figures

Resumo

A deposição química de vapor (CVD) de hidrocarbonetos vem se tornando um paradigma para a produção de grafeno em larga escala. No entanto, os mecanismos de crescimento associados ao processo ainda não são totalmente compreendidos, de forma que ainda não é possível um controle sistemático da qualidade dos filmes sintetizados. Nesta tese, apresentamos uma investigação detalhada do crescimento de grafeno por CVD à baixa pressão em um reator de parede fria, utilizando substratos de cobre. Uma combinação de imagens de microscopia electrônica de varredura e de espectroscopia Raman demonstrou que a síntese é fortemente influenciada pela temperatura e pela natureza do precursor de carbono. Utilizando um precursor líquido de carbono e temperaturas próximas do ponto de fusão do cobre, sintetizamos monocristais de grafeno relativamente grandes (~ 300 µm) a taxas muito elevadas (até 3 $\mu m^2.s^{-1}$). Sob tais condições, as formas dos domínios de grafeno apresentaram uma clara dependência com a orientação cristalográfica do cobre. Além disso, verificamos através de um gráfico de Arrhenius da *densidade de nucleação vs. temperatura* que a síntese de grafeno exibe dois regimes distintos: para temperaturas variando de 900° C a 960° C, a energia de ativação foi estimada em (6±1) eV; enquanto que para temperaturas acima de 960° C, a energia de ativação foi calculada em (9±1) eV. A comparação de tal dependência com a dependência da autodifusão do cobre com a temperatura sugere que o crescimento de grafeno é fortemente influenciado pelo rearranjo da superfície de cobre. Propomos um modelo que incorpora a auto-difusão de superfície do cobre como um processo essencial para explicar a relação entre a orientação dos monocristais de grafeno cristais e do cobre. Este modelo também é capaz de explicar as diferenças observadas entre as formas dos domínios de grafeno crescidos à pressão atmosférica e os crescidos a baixas pressões. Por fim, mostramos que *strain* é induzido nos filmes durante a coalescência dos domínios individuais de grafeno.

Abstract

The chemical vapor deposition (CVD) of hydrocarbons appears as the most suitable graphene production method for large area applications such as flexible displays and photovoltaics. However, the CVD mechanisms have not been fully understood and therefore a complete control over the morphology of the produced sheets has yet to be achieved. In this thesis we report a systematic investigation of graphene CVD at very low pressures performed on a cold wall reactor using copper substrates. A combination of scanning electron microscopy images and Raman spectroscopy measurements had demonstrated that the initial stages of graphene growth is strongly dependent of the growth temperature (T) and the nature of the carbon precursor. By using a high molecular weight liquid carbon precursor, growth of large graphene crystals (~up to 300 µm) at very high rates (up to 3 $\mu m^2.s^{-1}$) was achieved. For high temperature growth (T>900ºC), the shape and symmetry of the grains were found to depend on the underlying symmetry of the Cu crystal, whereas for lower temperatures (<900ºC), mostly rounded grains are observed. The temperature dependence of graphene nucleation density was determined, showing two thermally activated regimes, with activation energy values of (6±1) eV for 900 ºC < T < 960 ºC and (9±1) eV for T > 960 ºC. The comparison of such dependence with the temperature dependence of Cu surface self-diffusion suggests that graphene growth at high temperatures and low pressures is strongly influenced by copper surface rearrangement. A growth model was propose that incorporates Cu surface self-diffusion as an essential process to explain the orientation correlation between graphene and Cu crystals, and which can clarify the difference generally observed between graphene domain shapes in atmospheric-pressure and low-pressure chemical vapor deposition. In addition, we show that strain is induced over the graphene films during the coalescence of graphene individual domains.

1 Introduction

Graphene is, in simple terms, a single atomic layer of graphite. The existence of graphene itself is remarkable because before it "discovery" in 2004, when Novoselov and Geim [1] used adhesive tape to separate graphene sheets from graphite flakes, the stability of 2D crystals was uncertain. In fact, it was theoretically predicted [2, 3] that thermal fluctuations would destroy the long-range order of such crystals at non-zero temperature. The discovery of this 2D material triggered thousands of publications, largely because of its so-called extraordinary properties: high electron mobility [4], mechanical strength 200 times greater than steel [5], high thermal conductivity [6], and substantial absorption of white light, *i.e.* 2.3% (which is very high considering it is only one atom thick) [7]. Therefore, graphene have potential to be integrated into a huge number of applications. However, it has yet to be developed a production method that yields graphene layers with of well-defined properties in large quantities with competitive costs.

The current interest in chemical vapor deposition (CVD) of graphene is fueled by the prospect of producing high quality and economically viable materials for next generation electronic devices, such as solar cells, touchscreen displays, and chemical sensors, among other applications. [8] Graphene growth on copper foils by CVD has proven to be the most promising, inexpensive and readily accessible approach for fabrication of large-area mono or few layer graphene. [9, 10] However, large-scale production of films with suitable performance characteristics requires good understanding of the multiple processes involved in growth, as well as development of methods for systematic control of the growth dynamics. The synthesis of monolayer graphene having large grain size with well-defined shape is very important since grain boundaries strongly influence both transport and mechanical properties. [11] Investigation of copper-catalyzed graphene CVD has thus far suggested that parameters such as pressure, substrate quality, and precursor concentration, strongly dictate the graphene growth mechanism. In particular, the deposition pressure has a strong effect on graphene shape. Hexagonal islands with well faceted edges are usually observed in atmospheric pressure CVD (APCVD), [12, 13] in which carbon attachment processes are the rate-limiting growth step. In contrast, low pressure CVD (LPCVD) typically produces flower-shaped domains having lobes and dendritic features, which are related to diffusion limited growth [12, 14, 15]. Unlike APCVD, wherein resulting graphene domains are usually found to be randomly orientated over the substrate, there have been various LPCVD studies that provide evidence of a relationship between the shape, symmetry and orientation of graphene domains and the underlying lattice of Cu grains. [16, 17, 18, 19]

Until now, the proposed growth models to explain the observed relationship between the graphene domains and the underlying Cu crystals in LPCVD were based either on anisotropic attachment of carbon species to the graphene edges [16, 18, 20] or on anisotropic carbon diffusion over the substrate surface [21] or both [22].However, in these descriptions, Cu surface self-diffusion was not taken into account, even though it is expected to be considerable at typical growth temperatures, which are close to the Cu melting point. Thus, despite the considerable number of theoretical and experimental efforts since the pioneer work of Ruoff's group in 2009, [9] yet there is not a consensus about the ruling mechanisms of graphene CVD on Cu due the lack of a single theory which explains features observed in LPCVD that are not present in APCVD.

In this thesis, we have performed a study of very low pressure CVD of graphene on Cu using a liquid source in a cold wall reactor. In chapter 2, we provide a brief description of the graphene structure, followed by an overview of the potential methods for scale-production of graphene. We emphasize in the chemical vapor deposition, treating either the general aspects of the CVD process as the growth models that were invoked to explain the growth mechanism of graphene. We also present some interesting findings from the literature concerning the CVD of graphene over different metals.

In chapter 3 we provide details of the CVD system that we built in order to grow graphene. We also explain the main characterization tools and methods utilized in this work, i.e. Raman spectroscopy, electron backscatter diffraction, special considerations for imaging of graphene using optical microscopy, graphene transfer and electrical measurements. In chapter 4 we present and discuss our results. We also propose a model for graphene growth that incorporates Cu diffusion. Our conclusions are given in chapter 5.

2 Bibliography Review

2.1 Graphene Fundamentals

2.1.1 Graphene Chemistry

Carbon, the basic building block of graphene, has six electrons arranged in the $1s^2\ 2s^2\ 2p^2$ configuration, wherein 2 electrons fill the inner shell $1s$ and 4 electrons occupy the outer shell of $2s$ and $2p$ orbitals. It turns out, however, that the presence of other atoms in the neighborhood of the C atom (*e.g.*, hydrogen, oxygen, carbon) induces the hybridization of the $2s$ and $2p$ states. In particular, the superposition of the $2s$ orbital with two $2p$ orbitals, say $2p_x$ and $2p_y$, leads to the formation of the Φ bond responsible for the hexagonal planar structure of graphene. The remained unhybridised p_z orbital is perpendicular to the plane and bind with the neighboring carbon atoms, forming a π band. A typical manner of parameterize these orthogonal hybridized s-p states is the following [23]:

$$|sp_1^2\rangle = \frac{1}{\sqrt{3}}|2s\rangle + \sqrt{\frac{2}{3}}|2p_x\rangle \qquad \text{eq. 2-1}$$

$$|sp_2^2\rangle = \frac{1}{\sqrt{3}}|2s\rangle - \sqrt{\frac{1}{6}}|2p_x\rangle - \sqrt{\frac{1}{2}}|2p_Y\rangle \qquad \text{eq. 2-2}$$

$$|sp_3^2\rangle = \frac{1}{\sqrt{3}}|2s\rangle - \sqrt{\frac{1}{6}}|2p_x\rangle + \sqrt{\frac{1}{2}}|2p_Y\rangle \qquad \text{eq. 2-3}$$

These atomic orbitals (AOs) are shown in Figure 2-1. In free space, the orbitals $|sp_1^2\rangle$, $|sp_2^2\rangle$ and $|sp_3^2\rangle$ are degenerated [23]:

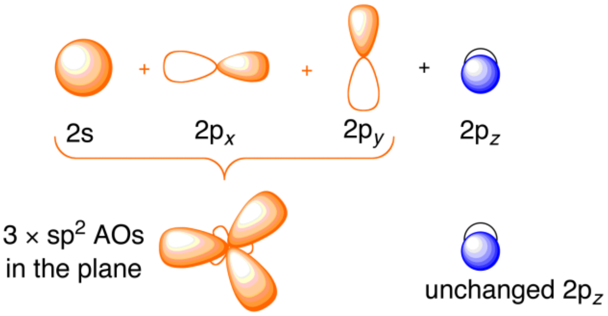

Figure 2-1 – sp^2 hybridization. Reproduced from [24].

Carbon atoms condense in graphene in a honeycomb lattice because three hybrid *sp*^{2} orbitals, having a mutual 120^o angle in the xy-plane, are induced in each atom. The honeycomb lattice is not a Bravais lattice since two neighboring sites are not equivalent, *i.e.* they cannot be connected by a lattice vector. Nevertheless, the honeycomb lattice can be viewed as a triangular Bravais lattice with a two-atom basis (A and B) as depicted in Figure 2-2.

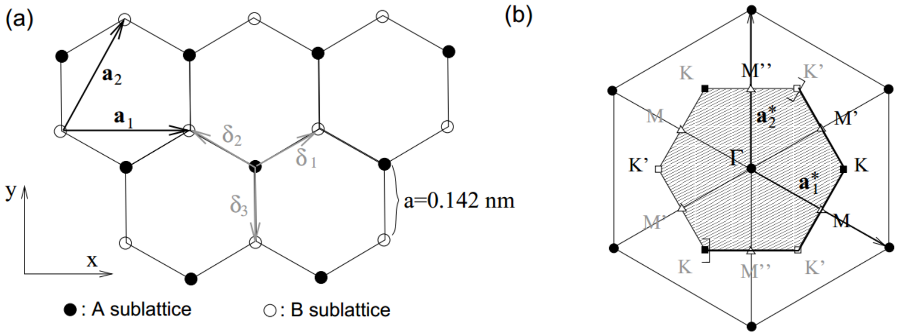

Figure 2-2 - (a) Graphene honeycomb lattice. (b) Reciprocal lattice of the triangular lattice. The shaded region represents the first Brillouin zone (BZ), withits centre $\mathbf{\Gamma}$ and the two inequivalent corners K (black squares) and K′(white squares). Reproduced from [25].

The triangular Bravais lattice shown in Figure 2-2(a) is spanned by the basis vectors:

$$\boldsymbol{a_1} = \sqrt{3}a\mathbf{e}_{\boldsymbol{x}} \qquad \text{and} \qquad \boldsymbol{a_2} = \frac{\sqrt{3}}{2}a\left(\mathbf{e}_{\boldsymbol{x}} + \sqrt{3}\mathbf{e}_{\boldsymbol{y}}\right) \qquad \text{eq. 2-4}$$

whilst the nearest neighbors vectors are denoted by:

$$\boldsymbol{\delta_1} = \frac{a}{2}\left(\sqrt{3}\mathbf{e}_{\boldsymbol{x}} + \mathbf{e}_{\boldsymbol{y}}\right), \quad \boldsymbol{\delta_2} = \frac{a}{2}\left(-\sqrt{3}\mathbf{e}_{\boldsymbol{x}} + \mathbf{e}_{\boldsymbol{y}}\right) \quad \text{and} \quad \boldsymbol{\delta_3} = -a\mathbf{e}_{\boldsymbol{y}} \qquad \text{eq. 2-5}$$

The first Brillouin zone is the region enclosed by the sets of planes that are perpendicular bisectors to the reciprocal lattice vectors:

$$\boldsymbol{a}_{\mathbf{1}}^* = \frac{2\pi}{\sqrt{3}a}\left(\mathbf{e}_{\boldsymbol{x}} - \frac{\mathbf{e}_{\boldsymbol{y}}}{\sqrt{3}}\right) \quad \text{and} \quad \boldsymbol{a}_{\mathbf{2}}^* = \frac{4\pi}{3a}\mathbf{e}_{\boldsymbol{y}} \qquad \text{eq. 2-6}$$

which connect the origin in k-space to its nearest neighbor reciprocal lattice points. In graphene, one may distinguish two inequivalent points, K and K’, alternating at the six corners of the hexagonal Brillouin zone shown in Figure 2-2(b). These points play a critical role in the electronic properties of graphene because low-energy excitations are centered around them.

2.1.2 Electronic Band Structure of Graphene

In graphene, three electrons per carbon atom are involved in the formation of strong covalent σ bonds (in three hybridized sp^2 states), and one electron per atom yields the π bonds (in a non-hybridised p_z state). Since the π electrons are the ones responsible for the electronic properties at low energies (the σ electrons form energy bands far away from the Fermi energy), in this section, we will restrict our discussion to the energy bands of π electrons within the tight binding approximation.

The Hamiltonian for an arbitrary electron in a solid, labelled by the integer *l*, is given by:

$$H_l = -\frac{\hbar^2}{2m}\nabla_l^2 + \sum_{n=1}^{N} V(\boldsymbol{r}_l - \boldsymbol{R}_n) \qquad \text{eq. 2-7}$$

where each ion on a site R_n produces an electrostatic potential felt by the electron. In the tight-binding approach, however, one assumes that electrons are tightly bound to the atom to which they belong, *i.e.*, they can be described with great accuracy by a bound state of the atomic Hamiltonian

$$H_l^a = -\frac{\hbar^2}{2m}\nabla_l^2 + V(\boldsymbol{r}_l - \boldsymbol{R}_n) \qquad \text{eq. 2-8}$$

The contributions to the potential energy $\Delta V = \sum_{n\neq l}^{N} V(\boldsymbol{r}_l - \boldsymbol{R}_n)$ from the other ions at the sites $\boldsymbol{R}_n$, with $n \neq l$, is treated perturbatively. The total Hamiltonian is the sum over all electrons:

$$H = \sum_{l}^{N} H_l^a\,(\boldsymbol{r}_l - \boldsymbol{R}_n) + \Delta V \qquad \text{eq. 2-9}$$

A trial wave function $\psi_k(r)$ for this Hamiltonian must be a linear combination of the atomic orbitals, $\varphi^{(j)}(\boldsymbol{r} - \boldsymbol{R}_n)$, which respect the lattice translation symmetry required by the Bloch's theorem. A wavefunction that fulfils this requirement is:

$$\psi_k^{(j)}(\boldsymbol{r}) = \sum_{\boldsymbol{R}_n} e^{i\boldsymbol{k}\cdot\boldsymbol{R}_n}\varphi^{(j)}\big(\boldsymbol{r} + \boldsymbol{\delta}_j - \boldsymbol{R}_n\big), \qquad \text{eq. 2-10}$$

where j = A/B labels the atoms on the two sublattices A and B and $\boldsymbol{\delta}_j$ is the nearest neighbor vector which connects atoms within the unit cell. By taking $\varphi^{(j)}(\boldsymbol{r}-\boldsymbol{R}_n)$ as eigenfunctions of the *$2p_z$* orbital and considering only the interaction of C atom with its first neighbors, the band structure of graphene obtained from the diagonalization of the Hamiltonian of eq. 2-9 is depicted in Figure 2-3.

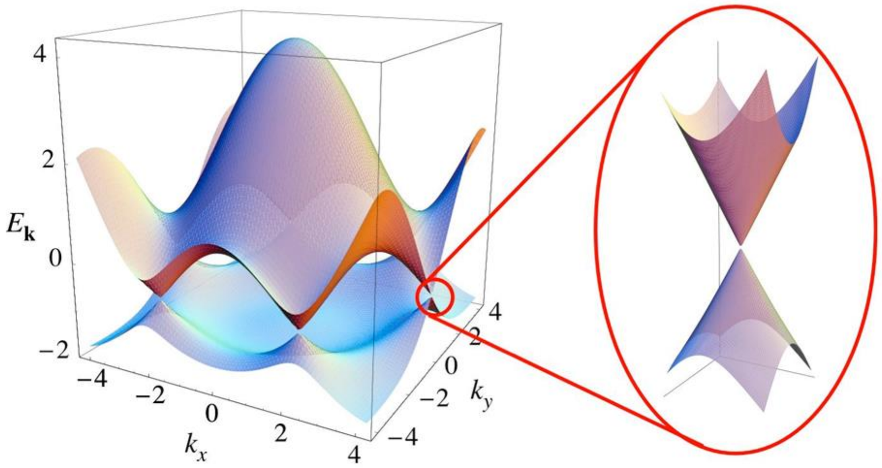

Figure 2-3 - Electronic dispersion of graphene. The conduction band and the valence band touch each other at K and K' points. The zoom shows that the dispersion relation close to these points resembles the energy spectrum of massless Dirac particles. Reproduced from [26].

The band structure nearby the K and K' points has a linear dispersion behavior, as highlighted in the inset of Figure 2-3. In this region, the dynamics of the charge carriers is governed by a Hamiltonian which is very similar to the Dirac Hamiltonian (massless). In fact, charge carriers located around the K and K' points behave as relativistic particles, whose energy dispersion is given by [26]:

$$\epsilon(k) = \pm\hbar\nu_F|k| = \pm\hbar\nu_F\sqrt{k_x^2 + k_y^2} \qquad \text{eq. 2-11}$$

2.1.3 Graphene Production

Mechanical exfoliation of graphite has enabled many fundamental studies of graphene proprieties due the high quality of the samples produced. However, the lateral dimensions of the exfoliated graphene are at most tens of micrometers, which make unfeasible the scalable production of graphene structures through this method. Therefore, the development of cost-effective fabrication methods is required in order that the unique combination of graphene properties can be effectively integrated into modern products. At present, dozens of methods to achieve large-scale production of defect-free graphene are being investigated; some of them are depicted in Figure 2-4.

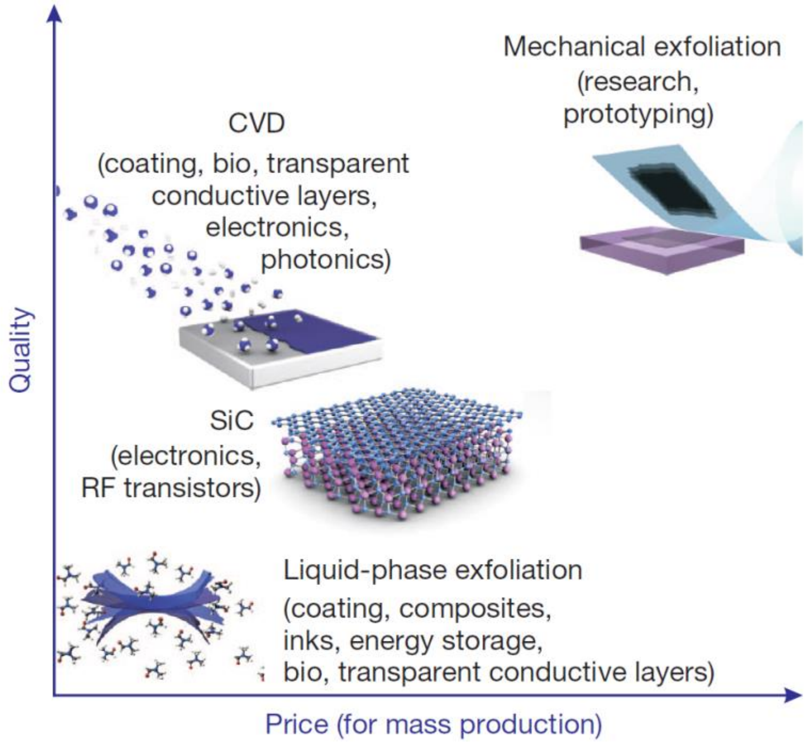

Figure 2-4 - Several methods of mass-production of graphene which allow a wide choice in terms of size, quality and price for any particular application. Reproduced from [8].

Liquid-phase exfoliation of graphite oxide consists in exposing graphite to a strong oxidizing agent which promotes the increase of the interplanar space between the graphite layers. A prolonged ultrasonically treatment is then employed to aid graphite to splits into layers, thereby yielding a significant fraction of monolayer flakes in suspension. The reduction of the obtained graphene oxide pellets to its parent graphene state can be achieved by either thermal or chemical approaches. Some of these methods may yield very high quality of the reduced graphene oxide (rGO), similar to pristine graphene, but they can demand the use of large quantity of hazardous agents or can be time consuming to carry out. Viable commercial applications based on liquid-phase exfoliation of graphite such as graphene-based paints and inks have already been demonstrated [8].

The controlled silicon sublimation from SiC crystals at high temperatures and ultrahigh vacuum conditions can also be employed to produce graphene layers. The quality of such graphene strongly depends on the growth conditions (pressure, temperature) and SiC characteristics (face and orientation), however, epitaxial graphene grown on SiC has the critical advantage to be compatible with standard lithography procedures already used by the semiconductor industry. The two major drawbacks of this technique are the cost of the SiC wafers and the high temperatures (above 1000 ºC) needed for the growth of high quality graphene. Nonetheless, investigations had demonstrated that the UHV Si sublimation process can be improved to produce monolayer graphene films with high mobilities, which may find applications within years when the existing high-frequency transistors, based on III–V materials (InGaAs, GaN, etc.), reaches their limit [8].

Another promising technique to produce graphene is based on the chemical vapor deposition of graphene from a gaseous carbon source onto the surface of a metal catalyst. The production of square meters of uniform polycrystalline graphene films has already been achieved via CVD of graphene [9, 10], which is fundamental for many applications. The transfer of the graphene from the metal catalyst to a target substrate is the major drawback of this method, though improvements had been made over the last years [27]. We discuss this method in details in the next sections.

2.2 Crystal Growth

In this section, a brief background of the exiting crystal growth theories is provided and the application of the concepts presented to the graphene case is highlighted.

2.2.1 Chemical Vapor Deposition of Thin Films

Chemical vapor deposition (CVD) is one of the major methods of film deposition for the semiconductor industry as it yields high throughput of high quality films at relative low costs. In a typical CVD process, volatile precursors are transported in the vapor phase to decompose on a heated substrate mounted inside a reactor chamber. During the reactant pyrolysis, several transport and reaction steps occur simultaneously as schematically indicated by the model depicted in Figure 2-5. The relative importance of each process depends on the chemical nature of the species involved and the design of the reactor used. Processes primarily involving the diffusion of species in the gas phase, through the boundary layer (Figure 2-5), are associated to the so-called *mass transport regime.* Processes which take place in the boundary layer or closer to the catalytic surface, on the other hand, fall into the *surface reaction regime.* It is possible to model these processes by considering the flux of active species through the boundary layer and the rate at which the active species are consumed at the surface of the catalyst. These fluxes are [28]:

$$F_{mass\ transport} = h_g(C_g - C_s) \qquad \text{eq. 2-12}$$

$$F_{surface\ reaction} = K_s C_s \qquad \text{eq. 2-13}$$

where, $F_{mass\ transport}$ is the flux of active species through the boundary layer, $F_{surface\ reaction}$ is the flux of consumed active species at surface, h_g is the mass transport coefficient, K_s is the surface reaction constant, C_g is the concentration of gas in the bulk, and C_s is the concentration of the active species at the surface. At steady state, theses fluxes are equal to each other and to the total flux. The elimination of C_s in eq. 2-12 and eq. 2-13, leads to:

$$F_{mass\ transport} = F_{surface\ reaction} = F_{total\ flux} = \frac{h_g K_s}{(h_g + K_s)C_g} \qquad \text{eq. 2-14}$$

The above equation states the existence of three growth regimes: the surface reaction controlled regime, $h_g \gg K_s$, the mass transport limited regime, $h_g \ll K_s$ and the mixed regime, $h_g \sim K_s$. Synthesis under atmospheric conditions and relative low temperatures (Figure 2-6) are usually limited by diffusion of the gas molecules through the boundary layer as transport reactions occur much more slowly than surface reactions due to the Arrhenius dependence of the later ($h_g \ll K_s$). This essentially leads to gas phase reactions in the bulk gas flow, which are often associated with thickness nonuniformity of the as grown films. This occurs because a small variation in the thickness of the boundary layer can induce a variation in the amount of active species that are diffusing through it.

In order to minimize flow effects and nonuniformity across the sample, one must designed experiments wherein the heterogeneous chemical reactions, which occur on surface reaction regime and are primarily dependent on the temperature of the substrate, should be favored, whereas homogeneous chemical reactions, which occur in the gas phase, avoided [29].

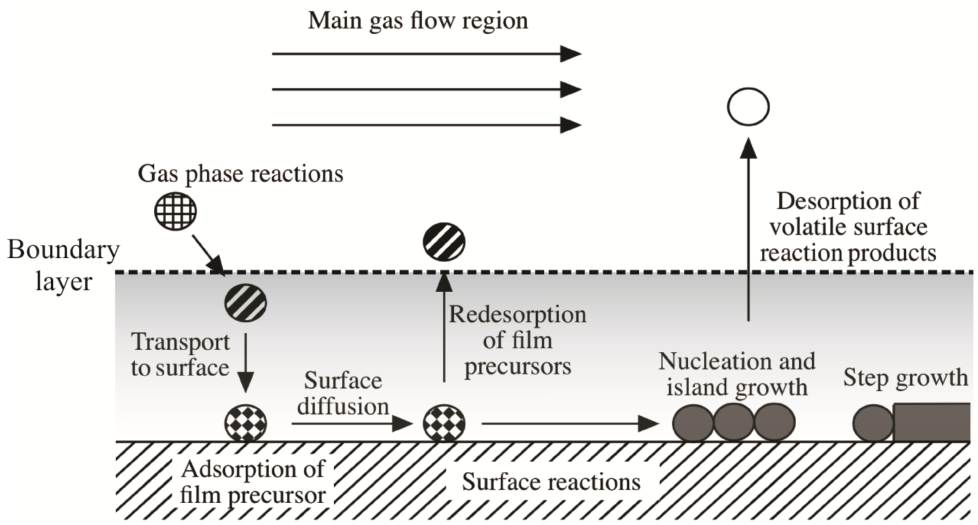

Figure 2-5. Schematic representation of the fundamental transport and reaction steps underlying CVD. Since no dissolution of carbon is considered, this model can be only applied to metals with low carbon solubility such as Cu or for lower temperature CVD in which carbon solubility is also insignificant. Reproduced from [30].

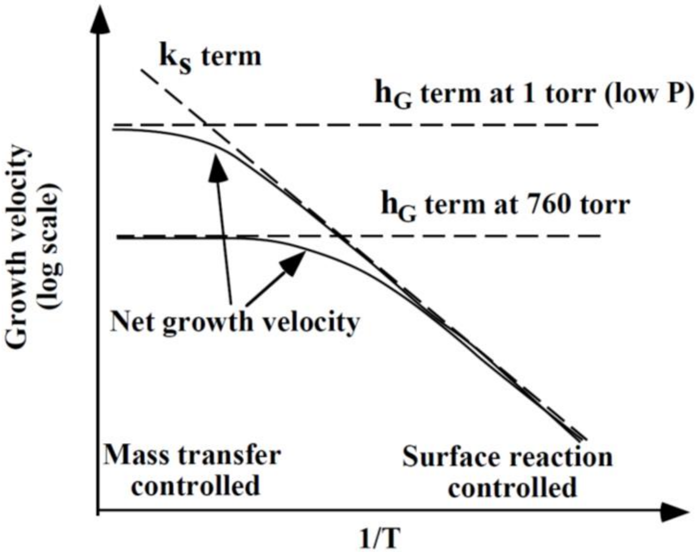

Figure 2-6 - Deposition rate as a function of temperature. Reproduced from [31].

Surface reaction limited regime can be achieved by lowering the pressure of the CVD reactor. At low pressures, the flux of active species is lower, essentially leading to fewer collisions and a higher diffusivity coefficient in the gas phase, D_g,

$$D_g \propto \frac{1}{P}; \qquad h_g = \frac{D_g}{\delta}; \qquad \text{eq. 2-15}$$

where P is the total pressure and δ is the boundary layer thickness. Both the diffusivity (D_g) and the mass transport coefficient (h_g) increase as the total pressure decrease. Hence, under appropriate synthesis conditions, the diffusion through the boundary layer is enhanced, and it is no longer the rate limiting step ($h_g \gg K_s$). As a result, the growth is limited by surface reactions which generally lead to better film uniformity as long as the temperature is held uniform across the substrate.

Graphene synthesis under atmospheric pressure conditions using Cu foils as catalyst usually leads to monolayer graphene at low methane partial pressures and to multilayer domains at higher methane partial pressures. [12, 13] Low pressure CVD in contrast, normally yields monolayer graphene that is uniform over large areas, and is nearly independent of methane partial pressure. [12, 14, 15] This suggests that graphene growth mechanism is kinetic controlled at the surface and self-limiting under low pressure conditions.

2.2.2 Crystal Growth Theories

Under appropriated synthesis conditions, graphene growth is governed by surface dynamics and can be viewed in the framework of existing crystallization theories. Here we discuss the several crystal growth theories that had been put forward over the years, emphasizing the application of their fundamental concepts to the 2D case of graphene. This provides a useful insight regarding the mechanisms and the kinetics related to the graphene growth.

2.2.2.1 Surface Energy Theory

The conglomeration of atoms which give rise the formation of the first sub-microscopic nucleus of the solid crystal is triggered by fluctuations within the precursor supersaturation (or solution supercooling) in a process known as nucleation (Figure 2-7). The probability of such small clusters grow to form a stable nucleus depends on the temperature, degree of supersaturation and change in free energy associated with its formation. The growth of stable nucleus leads to the formation of a crystal. The microscopic conditions of the growing surface, such as surface discontinues, have a critical effect over the evolution of the growing crystal as showed by Kossel and others [32, 33, 34]. However, the first theories of heterogeneous nucleation treated the formation of stable nuclei on flat surfaces from the thermodynamic point of view.

The early attempts to model crystal growth were based on the assumption that the equilibrium form of a crystal is the one which its surface free energy is minimal for a given volume. This concept was originally introduced by Gibbs [35] who believed that crystal growth was governed by the same mechanism responsible for the formation of water droplets in mist. Wulff [36] extended Gibbs's ideas by proposing that anisotropic growth rates could be related to the different surface free energies at the different faces of a growing crystal, *i.e* the equilibrium shape of a crystal is the one which minimizes the function:

$$\Delta G = \sum_i \gamma_i A_i \qquad \text{eq. 2-16}$$

where A_i is the area of the *i-th* plane with an interfacial energy of γ_i. The interfacial energy or surface energy gives a measure of the disorder of intermolecular bonds at a given surface. Since γ_i depends on the crystallography of the growing crystal, it can be very low for some crystal planes, making faceting energetically favored. The surface constructed from the inner envelope of planes perpendicular to the γ_i vector is known as Wulff construction and gives the equilibrium shape of the given crystal as illustrated in Figure 2-8.

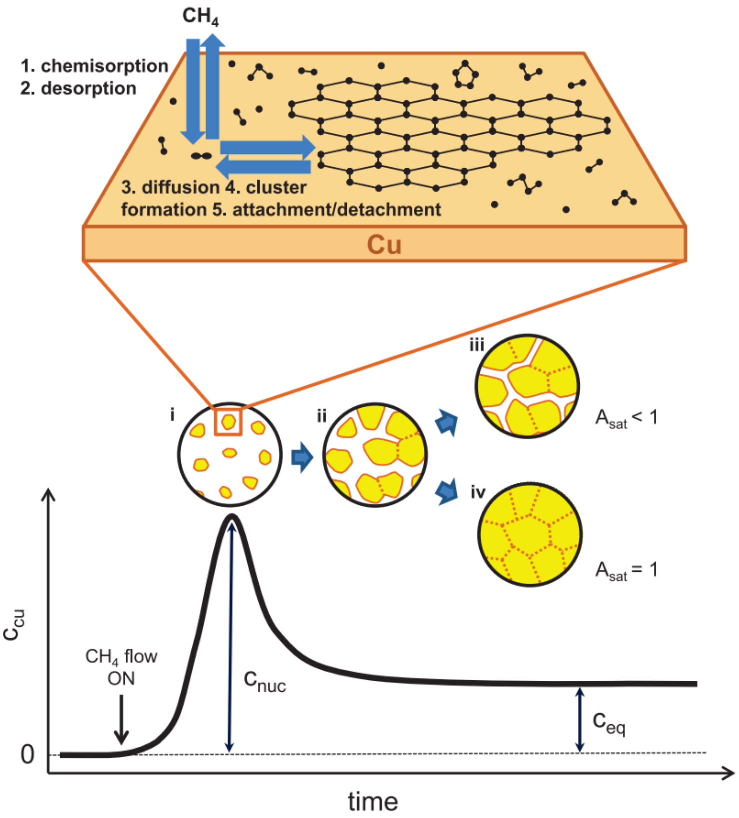

Figure 2-7. Nucleation and growth mechanism of graphene on Cu. The decomposition of methane leads to supersaturation of carbon adspecies at the Cu surface. When c_{cu} reaches a critical supersaturation point (c_{nuc}) graphene domains nucleate and begin to grow (i). The growth proceeds (ii) until the amount of superstaurated

carbon species are consumed (iii) or until the domains merge together full covering the surface of Cu (iv). Reproduced from reference [37]

In general, the Wulff construction provide a good agreement with the experimentally observed crystal shapes as long as the growth occurs near to equilibrium, with the attachment of adatoms at the edge of the growing island being the limiting step. Indeed, it was experimentally observed (see section 2.4.3.1) that atmospheric pressure and low carbon feedstock concentration yields regular hexagonal graphene with edges dominated by the zigzag direction in accordance with Wulff theory. The reason for that is the uneven attachment of the diffusive carbon adspecies at graphene's armchair and zigzag edges. As armchair edges have a higher density of unterminated carbon atoms (4.7 nm^{-1}) than the zigzag edges (4.1 nm^{-1}), it is expected that the former grows faster than the latter, resulting in the conversion of all armchair edges to zigzag by the attachment of new carbon atoms [38].

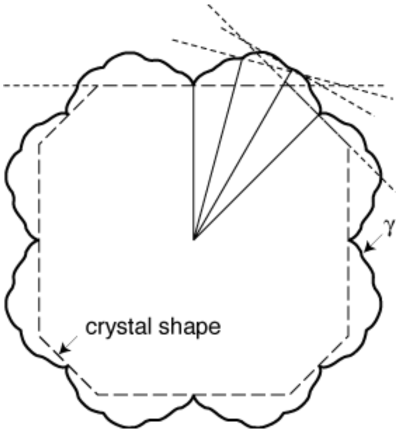

Figure 2-8 - Surface free energy γ plotted as a function of the angle θ describing the normal directions to the {hkl} planes in the Wulff construction. The equilibrium shape of the crystal is given by the dash-dotted curve. Reproduced from [39].

2.2.2.2 Surface Nucleation Model

The role of inhomogeneities at the growth surface is the basis of the model proposed by Kossel, Volmer and Stranski (KVS theory) [32, 33, 34]. According to them, the most energetically favorable site for the incorporation of a migrating adatom to an existing island is a kink site at the surface ledge. In fact, an adatom is attracted by at least three neighbors atoms at a kink site, whereas at a ledge it is attracted by two and on a terrace site, such bond is one (Figure 2-9). Therefore, it should be expected that island growth occurs mainly by incorporation of adatoms at the kinks of the ledge surface (step). Under ideal conditions, the step advances uninterruptedly until the whole layer is completed. The rate of this advance is proportional to the adatom supersaturation, S, and to the mean surface diffusion distance, x_s, [40]:

$$V = 2 \cdot S \cdot x_s \cdot v \cdot exp\left(\frac{-E_a}{K_B T}\right) \qquad \text{eq. 2-17}$$

where v is a frequency factor and E_a is the total evaporation energy. The migration distance x_s of an adsorbed atom is given by ${x_s}^2 = D_s \tau_a$ where D_s is the surface diffusion coefficient and τ_a is the mean life time of an adantom.

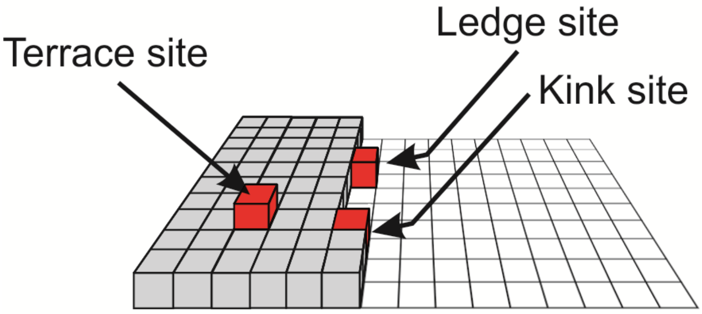

Figure 2-9 - The various atomic positions in the KVS model.

Burton, Cabrera and Frank [41] systematically studied this stepwise stacking, emphasizing the role of screw dislocations as continuous sources of steps on the surface of the crystal. The so called BCF theory views systems as composed of a staircase of terraces, wherein adatoms diffuse until they encounter a step along which they continue to diffuse until they are assimilated by a kink site. On terraces, the local mass conservation of mobile atoms leads to:

$$\frac{\partial c}{\partial t} = D\nabla^2 c + F - \frac{c}{\tau} \qquad \text{eq. 2-18}$$

where D is the diffusion coefficient of mobile atoms adsorbed on terraces, c is their surface concentration, F is the incoming flux, and τ is the typical adatom desorption time. Since adatom concentration in the vicinity of steps is not equal to the equilibrium concentration under nonequilibrium growth conditions, the diffusion mass flux arriving at the steps defines the boundary conditions for eq. 2-18. Thus, by denoting the upper and lower sides of a step by ±, the equation for the flux of adatoms coming from the upper and lower terraces are respectively given by [42]:

$$J_- = -D\left(\frac{\partial c_-}{\partial t}\right) = v_-\left(c_- - c_{eq}^*\right) + v_0(c_- - c_+) \qquad \text{eq. 2-19}$$

$$J_+ = D\left(\frac{\partial c_+}{\partial t}\right) = v_+\left(c_+ - c_{eq}^*\right) + v_0(c_+ - c_-) \qquad \text{eq. 2-20}$$

where $c_\pm$ denote the adatom concentration on the lower and upper terraces Figure 2-10 (a) and c_{eq}^* refers to the local equilibrium concentration. The attachment-detachment kinetics of adatoms to the step edge is governed by the kinetic coefficients, $v_\pm$ (Figure 2-10 (b)), whilst the direct exchange of adatoms between terraces is related to the transparency coefficient, v_0 (step crossing probability).

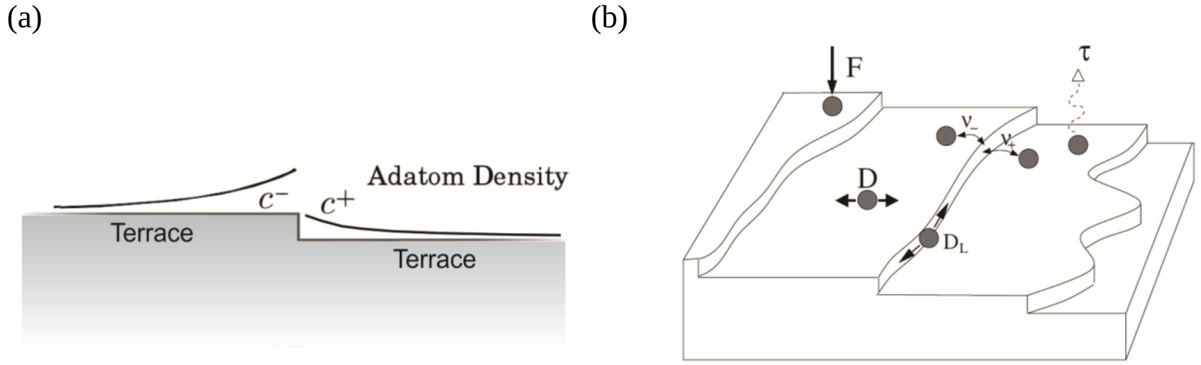

Figure 2-10 – Vicinal surface considered in BCF theory. (a) The values $c_\pm$ are the adatom densities on the right (+) and left (−) sides of the step; (b) Kinetic mechanisms governing the growth; D is the diffusion constant, F is the deposition flux, τ is the desorption time, and $v_\pm$ are step attachment coefficients from the lower and upper sides, respectively. Reproduced from [43, 44].

The equilibrium concentration, c_{eq}^*, has the Arrhenius form:

$$c_{eq}^* = c_{eq} exp(\mu / k_B T) \qquad \text{eq. 2-21}$$

where c_{eq} is the reference equilibrium concentration and μ is the chemical potential. The later depends of the step curvature, κ, and of the step stiffnes, $\tilde{\gamma} = \gamma + \gamma''$, where γ is the free energy per step length. Thus, the chemical potential can be expressed by:

$$\mu = \Omega \tilde{\gamma} \kappa \qquad \text{eq. 2-22}$$

where Ω is the area occupied by an adatom. When the radius of curvature of the step $1/\kappa$ is much larger than $\Gamma = \Omega \tilde{\gamma} / k_B T$, eq. 2-21 can be linearized and write as:

$$c_{eq}^{*} = c_{eq}(1 + \Gamma\kappa) \qquad \text{eq. 2-23}$$

where the constant Γ gives a measure of the edge energy of the step. The growth velocity can be obtained by considering the total flux of adatoms arriving at a step:

$$\frac{\mathrm{v}_n}{\Omega} = J = J_+ + J_-$$

$$= D\left(\frac{\partial c_+}{\partial t}\right) - D\left(\frac{\partial c_-}{\partial t}\right)$$

$$= \upsilon_+\left[c_+ - c_{eq}(1 + \Gamma\kappa)\right] + \upsilon_-\left[c_- - c_{eq}(1 + \Gamma\kappa)\right] \qquad \text{eq. 2-24}$$

The parameters $\upsilon_{\pm}$ and υ_0 determines the nature of the growth. When steps are perfectly permeable, $\upsilon_0 \to \infty$, and $c_+ = c_- = c_{eq}(1 + \Gamma\kappa) + \mathrm{v}_n/\Omega(\upsilon_+ + \upsilon_-)$. The critical consequence of this condition is that atoms may diffuse through many steps before they are incorporated to the crystal lattice, thereby making step dynamics non-local on stepped surfaces. This boundary condition is often used for solidification fronts and was invoked by Meca *et al.* [22] to describe the “epitaxial” growth of graphene on copper foils (Figure 2-11).

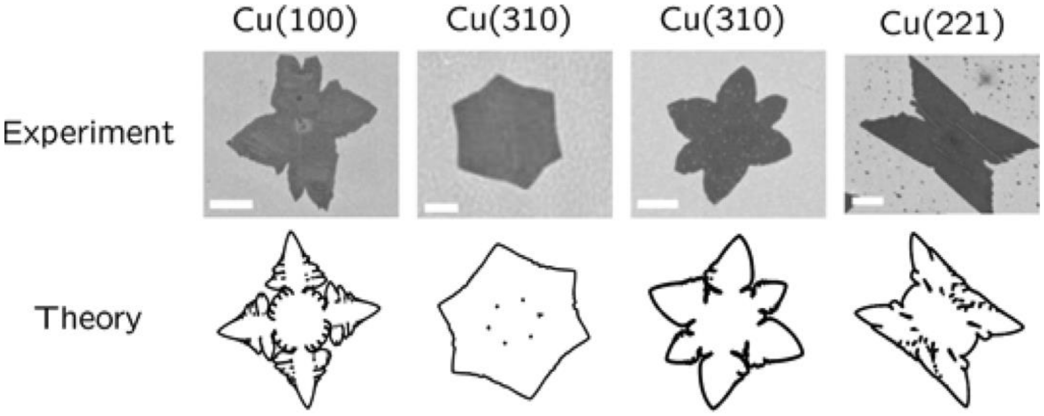

Figure 2-11 – Graphene nuclei shapes obtained on different copper facets and the corresponding shapes obtained from simulations using the BFC model. In this work was considered the anisotropic diffusion of carbon atoms induced by the crystallinity of the underlying substrate and the anisotropy of carbon attachment at the graphene edge. Reproduced from [22].

Another important effect arises when completely asymmetric boundary conditions, $\upsilon_0 \to 0,\ \upsilon_+ \to \infty,\ \upsilon_- \to 0$, are assumed. The so-called Ehrlich–Schwoebel effect accounts for the fact that an atom approaching the step from the upper terrace experiences an additional energy barrier, ΔE_{ES}, to descend to the lower terrace. This is because an atom crossing a step edge passes through an area with a low number of nearest neighbors. These boundary conditions is known as “one sided-model” and is frequently used to describe the step flow (or step motion) induced on vicinal surfaces heated to high temperatures under ultrahigh vacuum conditions (UHV). In this regime, the sublimation of the surface atoms result in macroscopic mass fluxes which leads to surface morphological transitions such as mound formation and step bunching (Figure 2-12). In chapter 4, we invoke these concepts to model the growth of graphene at high temperatures and under LPCVD conditions.

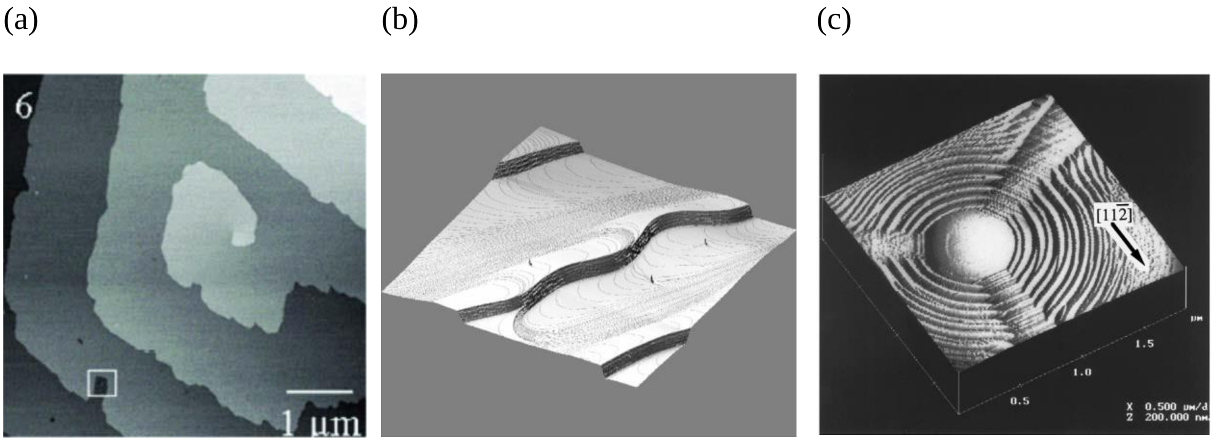

Figure 2-12 – (a) AFM image of a screw dislocation during the growth of an insulin crystal; (b) STM image of Si(111) surface showing three macrosteps formed from bunching of many monatomic steps; (c) Hole created on Si by a lithographic process and filled in after a annealing step at 1300ºC. The 3-fold crystallographic symmetry of the substrate is expressed in the pattern of steps generated around the filled hole. Reproduced from [42, 45]

2.2.2.3 Reaction Rate Theory

As discussed in section 2.2.1, the growth rate can be limited by surface reactions depending on the synthesis conditions. Processes such as reactant adsorption, dissociation, migration, desorption and incorporation at the lattice sites (Figure 2-5) can be related to characteristic times that depend on the concentration of adspecies and/or the percentage coverage of the substrate. Moreover, if these processes are thermally activated, their characteristic times are controlled by activation energies and frequency factors. As an example, the process of re-evaporation of adatoms from the substrate surface back to the gas phase can be characterized by the time τ_a [46]:

$$\tau_a = v^{-1}\exp(E_a/kT_s) \qquad \text{eq. 2-25}$$

where T_s is the substrate temperature, v is the surface vibration frequency and E_a is the re-evaporation energy. Similarly, one can assign characteristic times for the adatom diffusion and for the binding rate between individual atoms and small i-clusters. The characteristic parameters of each material together with the independent experimental variables (P and T_s) are essential to describe the nucleation and growth at the early stages.

As an example, the growth of graphene on Ru(0001) was explored by Zangwill and Vvedensky [47] using a simple rate model based on the experiments of Loginova *et al.* [48]. Starting from the assumption that precursor atoms arrive at the substrate at a rate R and stay in a state of mobile adsorption characterized by a life time τ_a and a diffusion constant D, the authors of this work stated that migrating adatoms attach directly to the edges of an existing islands or combine with other adatoms forming mobile clusters. In the latter case, clusters composed of $i = 5$ atoms [48] diffuse across the surface with a diffusion constant D' until $j = 6$ of them combine yielding an immobile island of size $i\times j$ [49, 50]. Islands such that continue to grow predominantly by the incorporation of 5-atoms clusters, albeit adatoms attachment at island edges cannot be completely ignored. The rate equations for these kinetic steps are expressed in terms of the homogeneous densities of adatoms n, 5-atoms clusters c, and islands N as [47]:

$$\frac{dn}{dt} = R - iDn^i + iKc - DnN + K'N - \frac{n}{\tau_a} \qquad \text{eq. 2-26}$$

$$\frac{dc}{dt} = Dn^i - Kc - D'cN - jD'c^j \qquad \text{eq. 2-27}$$

$$\frac{dN}{dt} = D'c^j \qquad \text{eq. 2-28}$$

where K is the rate of dissociation of clusters and K' is the detachment rate of adatoms from islands. In eq. 2-26, the adatom population density (n) increases due to atom adsorption from the gaseous phase (at rate R), dissociation from 5-atoms clusters (at rate iKc), and detachment from island edges (at rate $K'N$). It decreases due cluster formation (at rate iDn^i), adatom incorporation at islands edges (at rate DnN) and re-evaporation (at rate n_1/τ_a). The density of 5-atoms clusters (c) in eq. 2-27 increases due to cluster formation (at rate Dn^i), and decrease due cluster dissociation (at rate Kc), cluster incorporation at island edges (at rate $D'cN$), and clusters combination (at rate $jD'c^j$). The density of islands (N) in eq. 2-28 increases by the combination of 5-atoms clusters as discussed before.

The parameters D, D', K and K' have the Arrhenius form previously discussed (eq. 2-25). This set of rate equations retains enough physical content to enable the modeling of a realistic growth process as depicted in Figure 2-13.

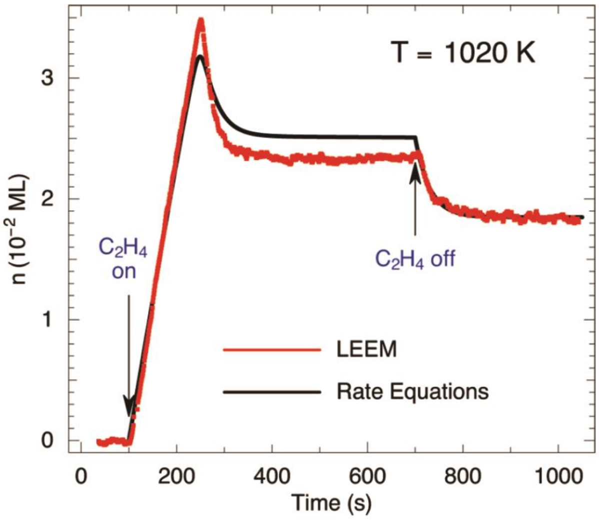

Figure 2-13. Carbon adatom density modeled using rate equations (black curve) compared with the corresponding LEEM data of Loginova *et al.* [48] (red data points). Reproduced from [47].

2.3 Precursor Catalysis

2.3.1 General Aspects of the Catalytic Mechanism

Hydrocarbon-based reactants are widely used as C source during graphene CVD synthesis. It turns out, however, that the pyrolysis of these precursors may require extreme levels of heat (*i.e.*, the methane molecule breakdown demands temperatures above 1200 °C due to strong C-H bonds [51]), thereby requiring decomposition to be carried out on the surface of a metal catalysts (*e.g.*, Fe, Co, Ni, Cu) which significantly lowers the energy barrier of the chemical reaction. Moreover, the metal substrate also determines the graphene deposition mechanism, which ultimately affects the quality of graphene. Monolayer graphene is obtained when the overall process is performed on the surface (*i.e.* adsorption, decomposition, and diffusion of molecules) and has only been observed in Cu so far. For Ni and other common transition metals (Co, Ru, Ir, etc.) that have high carbon solubility it has been demonstrated that hydrocarbon decomposes and carbon atoms dissolve into the metal film to form a solid solution. In this case, CVD growth of graphene occurs by carbon bulk diffusion and precipitation during the cooling step [52].

It is highly desirable to understand the underlying atomic details of the precursor pyrolysis in hope to optimize graphene growth conditions. Unfortunately, this knowledge is still very limited, and even the most fundamental question, what the active surface species is at the initial stage of growth, remains unclear. Nevertheless, several attempts had been made to explain the reaction mechanism as discussed by Muñoz and Gómez-Aleixandre in reference [29]. A model based on spectroscopic ellipsometry (SE) experiments [53] and theoretical calculations [54, 55] is schematized in Figure 2-14.

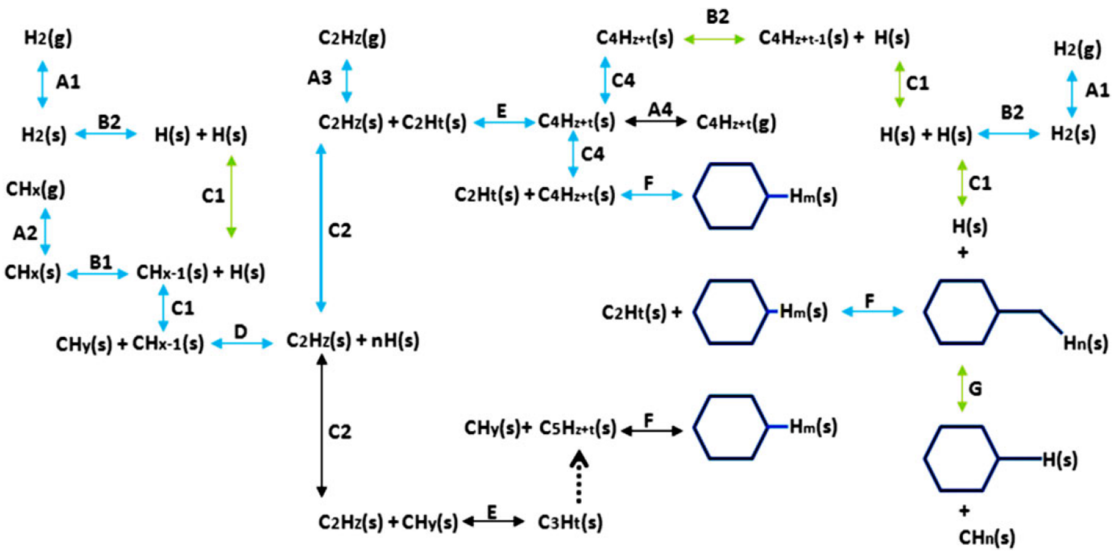

Figure 2-14 - Reaction mechanisms in CVD graphene. The blue arrows indicate the more probable (but not unique) reaction mechanisms. Reaction of type A: adsorption-desorption. B: dehydrogenation-hydrogenation. C: surface diffusion or migration (more favorable for dimers C_2). D: dimerization with or without simultaneous dehydrogenation (Dimers with hydrogen are not stable at high temperatures). E: polymerization - (cracking) decomposition. F: aromatization – decomposition. G: decomposition of aromatics. The green arrows indicate reactions with hydrogen. Reproduced from reference [29].

The thermal annealing of the metal substrate in a reducing atmosphere (*i.e.* hydrogen) is usually considered the first chemical reaction in a typical graphene CVD process. This procedure serves to remove surface impurities via oxygen reduction and to improve the surface roughness, through elimination of structural defects and increase of the substrate grains size (considering a polycrystalline substrate). Throughout this stage, the dissociative chemisorption of the H_2 molecules at the bare metal surface also occurs (Reaction B2), thus for metals that exhibit high hydrogen solubility, such as Cu, the surface is expected to be saturated by hydrogen [53, 56], whereas the recombination and desorption of the hydrogen atoms is more likely to occur at metal surfaces which show low hydrogen solubility, such as Ni (Reactions B2, A1). Therefore, in the case of Cu, the *hydrocarbon* molecules which are introduced in the subsequent step should face a surface partially covered with atomic hydrogen. The resulting competitive mechanisms between the dissociative chemisorption of H_2 (reactions A1-B2) and the physical adsorption and dehydrogenation of CH_4 (reactions A2-B1) on the metal surface is outlined in Figure 2-14.

According to theoretical calculations [54, 57], dehydrogenation reactions of methane into CH_x radicals possibly take place up to x = 2, with CH monomer dissociation being the rate-limiting step in case of Cu catalyst. Molecular dimers are formed by the binding of two of CH compounds in a reaction which is possibly accompanied by simultaneous dehydrogenation (Reaction D). Indeed, it was suggested [55] that C-C dimers are stable on all sites of Cu surface whereas carbon dimers containing hydrogen are very unfavorable on surfaces with low adsorption energies, desorbing or decomposing even at very low temperatures, as experimentally demonstrated [58]. Hence, in the case of Cu, the product of reaction D (Figure 2-14), C_2H_z with z = 0, must be considered the most probable end for the dehydrogenation cycle, signaling the formation of C-C bonds with sp^2-hybridization. In contrast, complete monomer dehydrogenation and carbon bulk diffusion can be expected in the case of high-solubility metals such Ni.

The role of mobile carbon dimers during the growth of graphene on Cu (111) was also investigated by Riikonen *et al.* [59] on basis of theoretical calculations. In their work, several competing processes were taken into account, such as dimer formation, dimer migration, dimers back dissociation into individual atoms, migration of carbon along the surface, and migration of carbon atoms into the bulk. They found that dimer creation and migration are the dominant processes since carbon dimers formation is a exothermic reaction and the migration barrier for the dimer to diffuse along the Cu(111) surface is small (E_a = 0.27 eV). Therefore, it is energetically favorable for dimers migrate around the surface than dissociate back into individual atoms. Other routes that include carbon trimmers, tetramers and pentamers as a result of carbon atom-by-atom incorporation have been also studied [59, 60], and are depicted in Figure 2-14 (Reactions E,F).

The size of the stable nuclei is subject of controversy. Despite the lack of direct experimental measurements of the cluster's atomic structure, *Ab initio* calculations indicate that shell structured C_{21} is a very stable cluster over Rh(111), Ru(0001), Ni(111) and Cu(111) [61]. Nevertheless, once nucleated the growth of a stable island must proceeds by the attachment of carbon species onto graphene edges. Theoretical analysis of graphene-edge reconstruction showed that C insertion into the front of a growing graphene nucleated on Cu (111) should occur preferentially (but not exclusively) in the form of dimers to armchair (AC) edges [62]. Other possibility was raised by Loginova *et al.* [48] who monitor the evolution of the density of carbon adatoms on Ru(0001) using the reflectivity of low energy electrons. According to these authors, graphene islands must grow mainly by the addition of 5-carbon atoms clusters instead of the standard monomer attachment. This conclusion was derived from the results described in section 2.4.2.

2.3.2 Activation Energy of Precursor Decomposition

Various gas, liquid, and solid precursors (C- and H-based compounds) have been used for graphene synthesis [63, 64, 65]. Zhancheng Li *et al.* [66] studied the mechanisms of graphene growth related with different carbon sources by dividing the CVD process into three stages. At stage I, precursor molecules collide with the surface, adsorbing on it, or scattering back to the gas phase. If they adsorb, stage II takes place and carbon source molecules dehydrogenate or partially dehydrogenate, forming active surface species which coalesce, nucleate, and grow to graphene at the stage III.

According to Jin-Ho Choi *et al.* [67], the magnitude of the adsorption energy plays an important role in the competition between desorption and dehydrogenation. It is more probable for an adsorbed molecule to desorb from the surface back to the gas phase than to dehydrogenate if its adsorption energy is much less than the potential energy barrier against dehydrogenation. For example, the high binding energies calculated for C_6H_6 and $C_{18}H_{14}$ molecules (0.67 and 1.93 eV, respectively) should facilitate their dehydrogenation by prohibiting their easy desorption from the surface, principally for the latter specie, which have a lower dehydrogenation barrier than desorption. On the other hand, small molecules such as CH_4 are more difficult to dehydrogenate because their desorption barrier of 0.17 eV is one order of magnitude smaller than the dehydrogenation barrier. Consequently, graphene growth using CH_4 as the carbon source can only proceed at much higher temperatures and supersaturated gas pressures since it is less favorable for CH_4 molecule to stay adsorbed on the catalyst surface.

2.4 Graphene Growth on Metal Surfaces

The ability of transition metals to provide low activation energy pathways for reactions resides in the fact that their outermost *d* orbitals are incompletely filled with electrons. This makes transition metals prime candidates for catalysis since they can easily give and take electrons, either by the facile change of oxidation states or by the formation of intermediate compounds.

Graphene CVD was first reported on Ni and Cu substrates [52, 68], then followed by intense research activities and publications using a variety of other transition metal substrates such as Ru and Ir [69], Pd [70] and Pt [71]. Hereafter, we will discuss the general aspects related to the graphene CVD on metal substrates.

2.4.1 Graphene Growth on Ni

Graphitic carbon formation on nickel was intensively studied owing the suitability of Ni as catalyst for high quality graphite and nanotubes [72]. Polycrystalline Ni was also found to be a good substrate for graphene synthesis, although the percentage and size of monolayer graphene region are often limited by the quality of Ni films, especially by the size of the Ni grains after the thermal annealing. Therefore, the adoption of single-crystalline Ni is a recurrent solution in order to improve graphene uniformity. This aspect is evidenced in Figure 2-15 which compares graphene CVD on single and polycrystalline Ni substrate. While as-grown graphene on Ni(111) exhibits a smooth surface with relatively uniform color as depicted in Figure 2-15b, graphene on polycrystalline Ni displays a rough surface with many dark regions (Figure 2-15e) which represent multiple graphene layers. Complementary characterization using micro-Raman surface mapping reveals that the area percentage of monolayer/bilayer graphene on Ni(111) substrate is 91.4% (Figure 2-15c), whereas the percentage on the polycrystalline Ni is of just 72.8% (Figure 2-15f). In addition, was found that most of the multilayer nucleation occur at the grain boundaries in the polycrystalline Ni substrates as depicted in Figure 2-15d

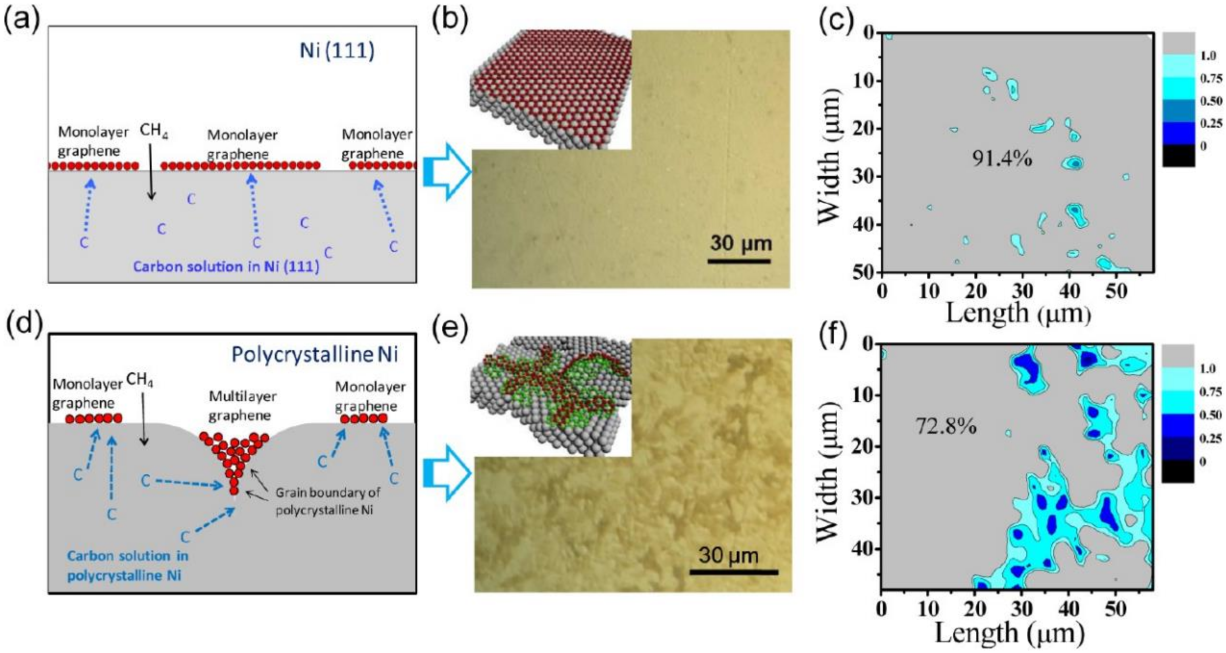

Figure 2-15. Schematic diagrams of graphene growth mechanism on Ni(111) (a) and polycrystalline Ni surface (d). Optical image of graphene grown on Ni(111) (b) and polycrystalline Ni (e). Maps of I_{2D}/I_G of Raman spectra collected on the Ni(111) surface (c) and on the polycrystalline Ni surface (f). Reproduced from reference [73]

Other important aspect of CVD graphene on Ni is that the thickness and quality of the films are strongly affected by the carbon segregation process, which ultimately depends on the cooling rate. Medium cooling rates are found to lead to optimal carbon segregation and produce continuous few layer graphene. The specific growth parameters used by several groups are summarized in Table 1 reproduced from ref. [73].

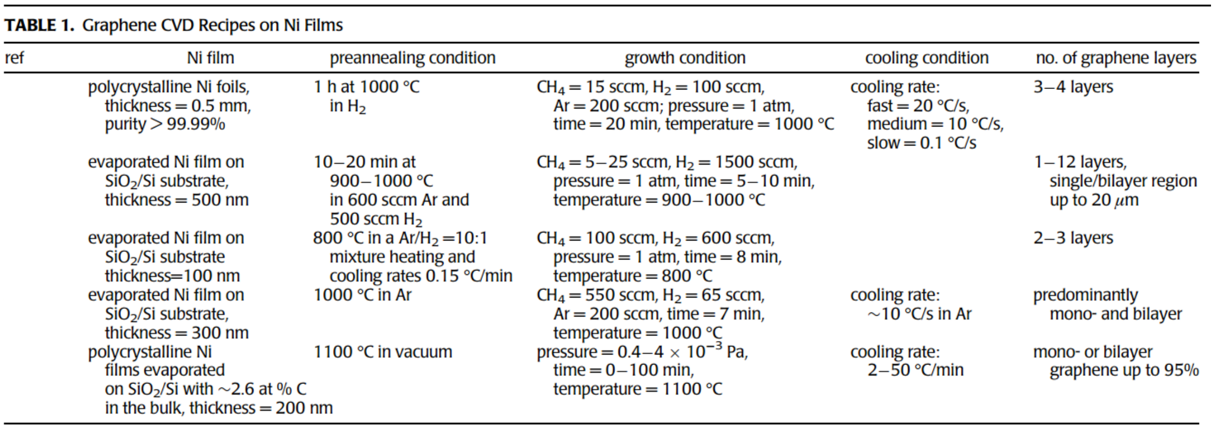

TABLE 1. Graphene CVD Recipes on Ni Films

ref	Ni film	preannealing condition	growth condition	cooling condition	no. of graphene layers
	polycrystalline Ni foils, thickness = 0.5 mm, purity > 99.99%	1 h at 1000 °C in H_2	CH_4 = 15 sccm, H_2 = 100 sccm, Ar = 200 sccm; pressure = 1 atm, time = 20 min, temperature = 1000 °C	cooling rate: fast = 20 °C/s, medium = 10 °C/s, slow = 0.1 °C/s	3–4 layers
	evaporated Ni film on SiO_2/Si substrate, thickness = 500 nm	10–20 min at 900–1000 °C in 600 sccm Ar and 500 sccm H_2	CH_4 = 5–25 sccm, H_2 = 1500 sccm, pressure = 1 atm, time = 5–10 min, temperature = 900–1000 °C		1–12 layers, single/bilayer region up to 20 μm
	evaporated Ni film on SiO_2/Si substrate thickness=100 nm	800 °C in a Ar/H_2 =10:1 mixture heating and cooling rates 0.15 °C/min	CH_4 = 100 sccm, H_2 = 600 sccm, pressure = 1 atm, time = 8 min, temperature = 800 °C		2–3 layers
	evaporated Ni film on SiO_2/Si substrate, thickness = 300 nm	1000 °C in Ar	CH_4 = 550 sccm, H_2 = 65 sccm, Ar = 200 sccm, time = 7 min, temperature = 1000 °C	cooling rate: ~10 °C/s in Ar	predominantly mono- and bilayer
	polycrystalline Ni films evaporated on SiO_2/Si with ~2.6 at % C in the bulk, thickness = 200 nm	1100 °C in vacuum	pressure = 0.4–4 × 10^{-3} Pa, time = 0–100 min, temperature = 1100 °C	cooling rate: 2–50 °C/min	mono- or bilayer graphene up to 95%

2.4.2 Graphene growth on Ru

As already mentioned in section 2.3.1, the data for graphene growth rate as function of C adatom supersaturation obtained during the growth of graphene on Ru(0001) suggest that the active surface species driving graphene domain growth is 5-C clusters [48]. This supposition was made by noting that the growth velocity of the graphene front, v, is a highly nonlinear function of the supersaturation. Indeed, the adjust of the experimental curves of *Graphene Growth rate vs. C monomer coverage* shown in Figure 2-16(a) leads to:

$$v = k\left[\left(n/n_{eq}\right)^5 - 1\right] \qquad \text{eq. 2-29}$$

where n is the carbon adatoms density and n_{eq} is its equilibrium density.

In addition, it was demonstrated that graphene first nucleates at step edges, which are believed to lower the barrier to graphene nucleation. However, as the C monomer concentration increases, multiple nucleation events take place at the terraces of the Ru substrate, as depicted in Figure 2-16(b).

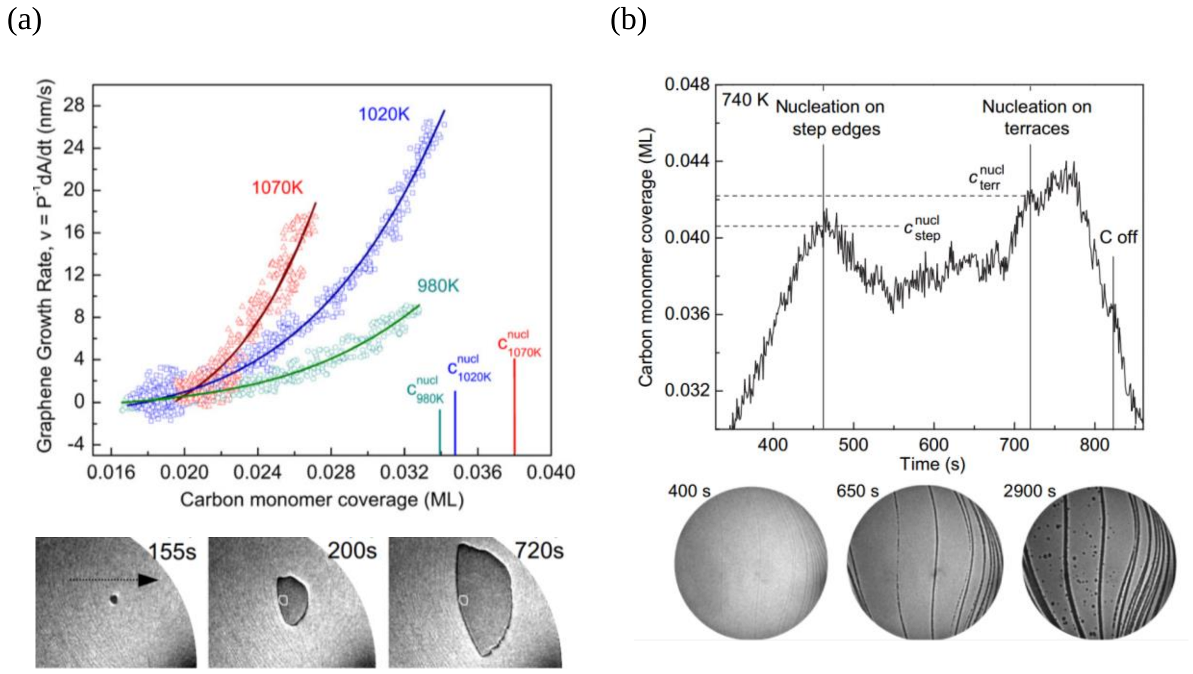

Figure 2-16 – (a) Island growth rate as function of monomer concentration; (b) Time evolution of C monomer concentration during C deposition. Nucleation start to occur at the steps edges of Ru substrate, and then it takes place at the Ru terraces at higher C concentrations. Reproduced from [48].

The growth of graphene on Ru(0001) was also explored by Günther *et al.* [74] who investigated the epitaxial growth of graphene via ethylene-based CVD at ultrahigh vacuum (UHV) conditions. Sequential images obtained by in-situ scanning tunneling microscopy showed that at relatively low temperatures, the front of a graphene island can expands through the uncovered parts of Ru surface, crossing the typical distribution of terraces and monatomic steps of single crystal metal surfaces. At lower pressures or higher temperatures, however, it was observed that graphene no longer traverses the atomic steps, but continues growing on the same terrace level, i.e. together with the Ru terrace. According to the authors, this can only mean that Ru atoms are transported to the growing step edge where they enter underneath the graphene layer. Both growth modes are presented in Figure 2-17. This work provides a noteworthy evidence of the influence of the substrate dynamics during the graphene growth.

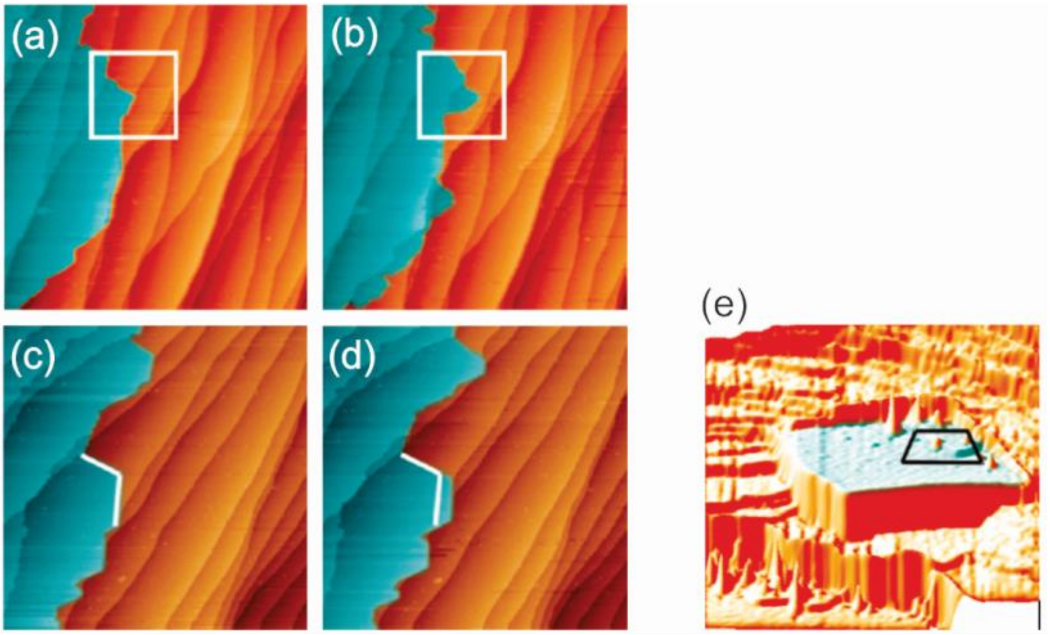

Figure 2-17 - In situ STM scans showing: (a-b) the growth of graphene (blue) across the steps of the Ru(0001) surface (orange) at 665º C; (c-d) graphene growth at higher temperatures (or low pressures) accompanied by the extension of the underneath Ru terrace. e) Extensive faceting of the Ru surface induced by the above graphene layer. Reproduced from [74].

2.4.3 Graphene growth on Cu

CVD of graphene on Cu has been intensely investigated with the aim of consistently producing uniform, high-quality graphene. The synthesis conditions were found to strongly dictate the growth mechanism of graphene individual domains. Pressure, for example, has a key role in the determination of shape and morphology of these domains. Therefore, in this section we will discuss separately the foremost results obtained from atmospheric pressure and low pressure CVD of graphene on Cu.

2.4.3.1 Atmospheric pressure CVD – APCVD

The controlling and characterization of single-crystal graphene grains, prior to the coalescence of a complete monolayer, was the subject of the work of Qingkai Yu *et al.* [12]. In their study, carried out at 1050 ºC under atmospheric pressure of a gas mixture of CH_4 diluted in Ar (concentration 8 ppm) and H_2, they synthesized hexagonally shaped single-crystal grains. They found that the junction formed between coalescing domains deteriorate the electrical transport, even when the edges of the individual graphene domains were aligned and parallel to zigzag directions. Moreover, it was shown that graphene grains do not have well-defined epitaxial relationship with the Cu substrate and that spatially ordered arrays of graphene domains can be artificially initiated by pre-patterned growth seeds, as shown in Figure 2-18.

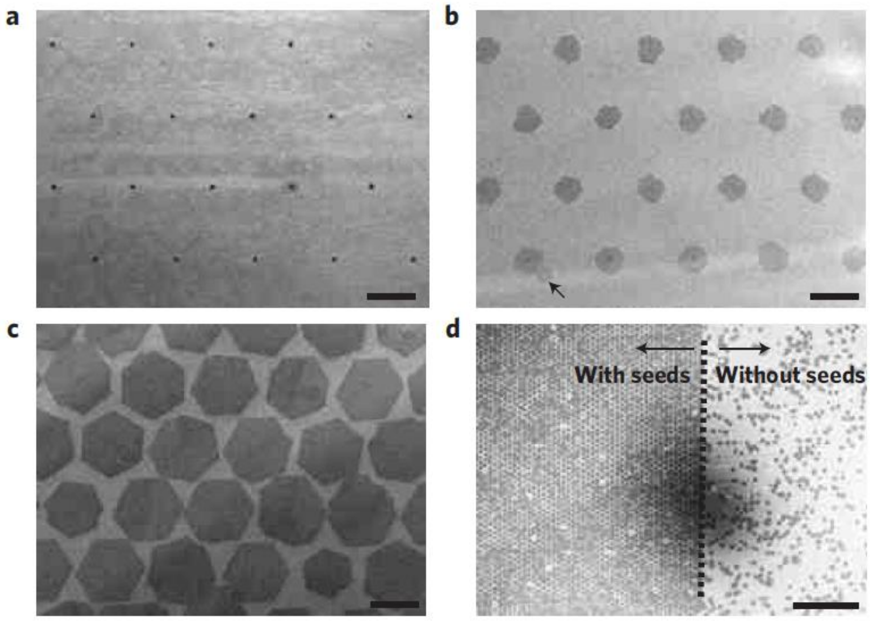

Figure 2-18. (a-c) SEM image showing an array of seed crystals patterned on Cu foil by e-beam lithography. (d) SEM image of a seeded array of graphene domains next to a randomly-nucleated set of graphene domains in an area without seeds. Scale bars in (a-c) are 10 µm and the scale bar in (d) is 200 µm. Reproduced from [12].

Other study [65] demonstrated the synthesis of graphene domains with millimeter size by continuously adjusting the concentration of the precursor feedstock during the growth. This has been done by controlling the temperature of a solid polystyrene source, which sublimate under a background flow of Ar/H_2 carried through the reactor. In the process shown in Figure 2-19, the carbon feedstock is gradually increased until it reaches a critical supersaturation value which triggers graphene nucleation. Once graphene islands starts to form, the reactant flow is decreased to below the nucleation threshold in order to prevent further nucleation. As the growth progresses, the feeding flow is then increased to provide continuous growth for the graphene domains. It was demonstrated that through this process the nucleation density of graphene domains can be lower as ~100 nuclei/cm^2 and the dimension of single crystal grain up to ~1.2 mm. According to the authors, the electro-polishing of the Cu substrate, followed by a long thermal pre-treatment, is also an important step for the growth of these large graphene domains.

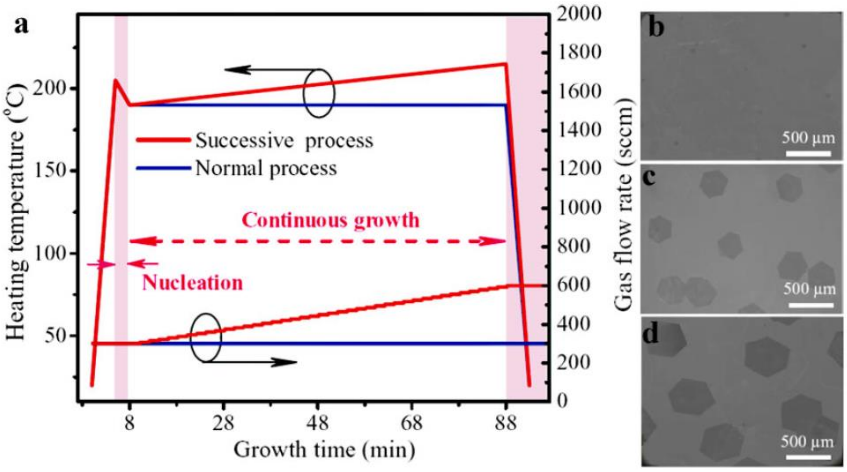

Figure 2-19. (a) APCVD growth of graphene at 1050 °C with a linear increase of temperature of the polystyrene source and total reactant gas flow. (b-d) SEM image of the obtained hexagon-shaped graphene domains. Reproduced from [65].

The morphological evolution of graphene crystals in atmospheric pressure CVD on ultra-smooth, epitaxial Cu(100), Cu(110), and Cu(111) thin films, was also investigated. The growth of large graphene domains at low density was achieved on the inside of an enclosure formed by bending a thick copper foil to form an envelope [9]. It was speculated that the inside of the enclosure offers a much lower partial pressure of methane and a “better” environment during growth, providing a much lower pressure of unwanted species and a quasi-static background of Cu vapor.

Jacobberger and Arnold [16] found no clear relationship between the APCVD graphene and the underneath Cu substrate. However, they shown that the dendritic nature of the growth can be enhanced or suppressed by controlling the H_2:CH_4 ratio. According to them, the morphology trends with varying H_2:CH_4, depicted in Figure 2-20, can be possibly explained by: (a) a change in the concentration of C_xH_y surface species involved in growth; (b) a change in the dominant C_xH_y species involved in growth as a result of (a); (c) an increase of the mobility of the growth species around the nucleus perimeter; (d) anisotropic hydrogen etching of graphene domains.

Moreover, the trend displayed in Figure 2-20 suggests that hydrogen shifts the growth kinetics from edge-attachment-limited to diffusion-limited. In other words, if the attachment of carbon at graphene edge is the fastest reaction, the growth of graphene nuclei will be limited by the rate at which diffusive carbon adspecies reach the graphene border. This growth mode is much more common during LPCVD process, which is discussed in the next section.

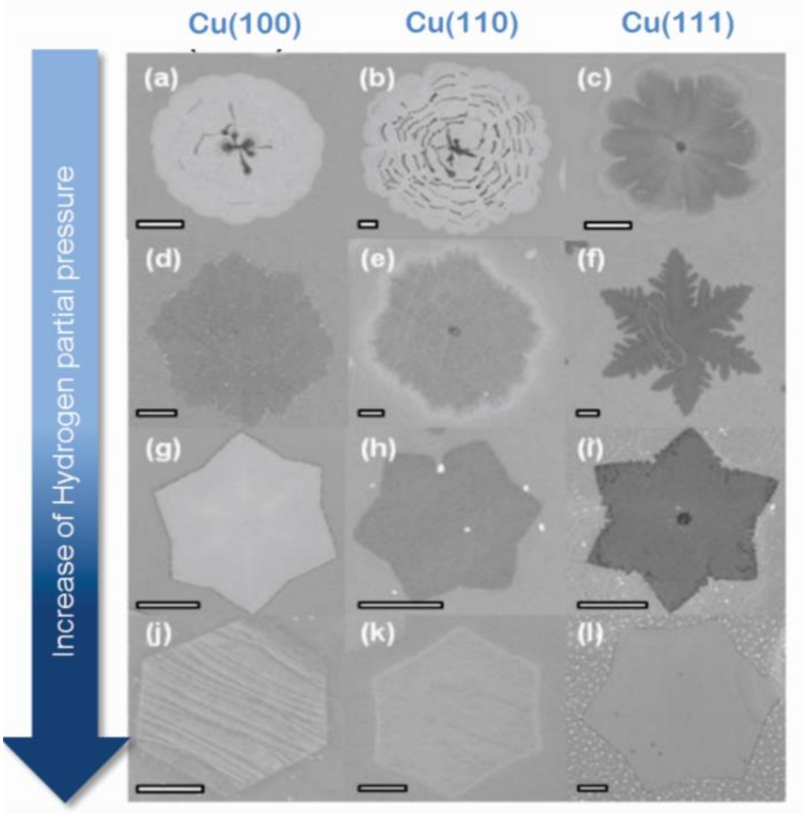

Figure 2-20. Graphene island morphology dependence on H_2:CH_4 in APCVD. First, second, and third columns represent the island structure on Cu(100), Cu(110), and Cu(111). Reproduced from [16].

2.4.3.2 Low pressure CVD – LPCVD

The main reason for using LPCVD instead of APCVD is that the first usually yields better outcomes in terms of uniformity of the deposited film, substrate step coverage and contamination by unwanted particles [30]. The deposition process occurs predominantly in the surface reaction limited regime, as discussed in section 2.2.1, and the rate at which molecules from the gas phase arrives at the surface increases proportionally to the pressure, *i.e.*, $R =$

$(2\pi mkT)^{-1/2}$ P. In the particular case of graphene synthesis, it was additionally found a relationship between the grown graphene and the underneath substrate crystallography.

Wood *et al.* [17], combining electron backscatter diffraction with spatial Raman techniques, studied the effects of polycrystalline Cu on graphene growth. They verified that Cu(100) surfaces often causes slow growth of multilayer graphene, whereas high index Cu facets frequently induces fast growth of compact graphene islands with anisotropic lobed shapes. On the other hand, Cu (111) surface was found to promote fast growth of monolayer graphene with few defects. They concluded that the growth mechanism of graphene was crystallographically dominated, strongly depending on the surface energy of the Cu crystal structure and little affected by the surface roughness. These results triggered the attention of other research groups for the largely neglected influence of the Cu substrate in graphene nucleation and growth.

Zang *et al.* [14] reported the growth of large-grain, single-crystalline graphene flowers with grain size up to 100 μm using a vapor trapping LPCVD method. Controlled growth of graphene flowers with four lobes and six lobes had been achieved by varying the growth pressure and the methane to hydrogen ratio. However, electron backscatter diffraction characterization revealed that the graphene morphology had little correlation with the crystalline orientation of the underlying copper substrate. According to the authors, graphene morphology mostly relates to the local environment around the growth area (i.e. temperature, total pressure and H_2:CH_4 ratio) rather than the crystalline structure of the underneath copper crystal.

Contradicting the study mentioned above, Wofford *et al.* [20] showed that 4-fold-symmetric graphene islands nucleate and grow preferentially on the Cu (100)-textured surface, though each of the four lobes of these graphene domains had a different crystallographic alignment with respect the underlying Cu. According to the authors, this well-ordered "polycrystalline" islands form only above ∼790 °C and its shape evolution is related to complex heterogeneous nucleation events at the imperfections of the substrate surface. In addition, it was observed that sublimation-induced motion of Cu steps at higher temperatures at UHV conditions also creates a rough surface, where large Cu mounds form under the graphene islands, as depicted in Figure 2-21.

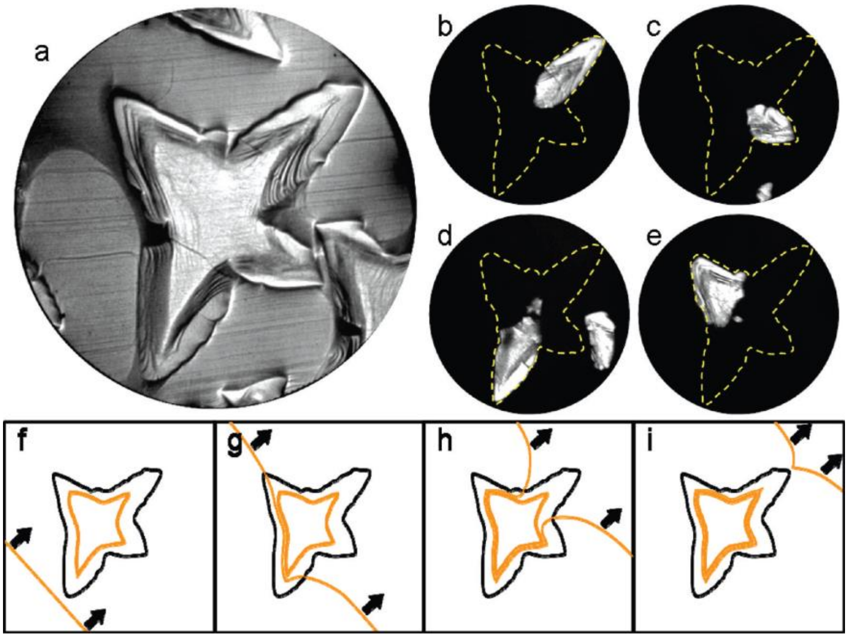

Figure 2-21. Bright (a) and dark field (b-e) LEEM images showing the spatial distribution of lobes of 4-fold-symmetric graphene islands nucleated on Cu(100). Copper step edge accumulation (hillock formation) is illustrated in (f-i). Reproduced from [20].

The complex interplay between graphene and the underneath substrate was also subject of others studies [22, 16] where shape, orientation, edge geometry, and thickness of the graphene domains were found to be controlled by the crystallographic orientations of Cu substrates. In fact, it was demonstrated that flower-like graphene islands develop dendritic branches which extend hundreds of microns in the ⟨001⟩, ⟨111⟩ and ⟨101⟩ directions on Cu(100), Cu(110), and Cu(111), respectively. Jacobberger and Arnold [16] attributed this phenomenon to the development of Mullins-Sekerka morphological instabilities [75] during the growth. *Meca et al.* [22], on the other hand, relate the morphological evolution of the graphene islands to the anisotropic diffusion of carbon atoms induced by the crystallinity of the underlying substrate and to the anisotropy of carbon attachment at the graphene edges (see Figure 2-11).

A similar morphology trend was reported by another study [16] during the growth of graphene using electro-polished copper foils (Figure 2-22). Under low-pressure conditions, it was observed that single-layer graphene domains align with zigzag edges parallel to a single ⟨101⟩ direction on Cu(111) and Cu(101), while bilayer domains align to two directions on Cu(001). According to Murdock *et al.* [18], the origin of this relationship is based on the minimization of the lattice mismatch between graphene and the underneath Cu. Using computational modelling, the authors calculate the most stable position at which a nanoscale nucleating domain (C_{28}) may preferentially locate above each Cu surface. Their results are shown in Figure 2-23.

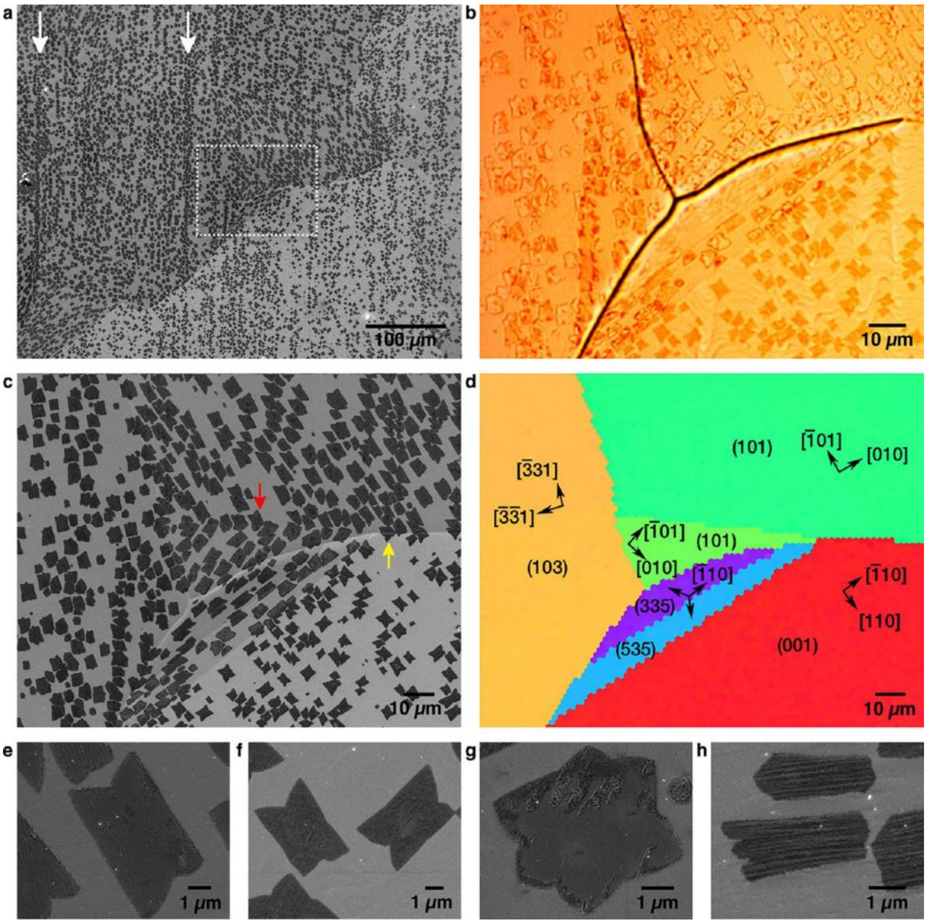

Figure 2-22. (a-d) Shape and orientation dependence of LPCVD graphene domains on polycrystalline Cu. (e,f,g,h) SEM images of representative LPCVD graphene domain shapes grown on Cu{101}, Cu{001}, Cu{103}, and orientations close to Cu{111}, e.g., Cu{769}, respectively.

According to Figure 2-23(a-b), the graphene C_{28} cluster is stabilized on Cu surfaces (101) and (001) when its dangling bonds at the zigzag edge form directional bonds with the Cu surface atoms along the ⟨101⟩ directions. On Cu(111), however, the C_{28} become stable when its atoms at the zigzag edge hybridize with two neighboring Cu surface atoms as depicted in Figure 2-23 (c). In all these cases, the armchair edge atoms hybridize mainly among themselves, enhancing electron density near the corner of the C_{28} cluster (Figure 2-23-(g-i)) and promoting the growth in the [-101] direction.

In summary, shapes of individual graphene domains obtained by LPCVD process are frequently diverse and included polygon and multi-lobed flower-like structures depending on the growth conditions and/or crystallographic orientations of the substrate. Atmospheric pressure CVD, meanwhile, generally led to graphene domains of six-fold-symmetric hexagons.

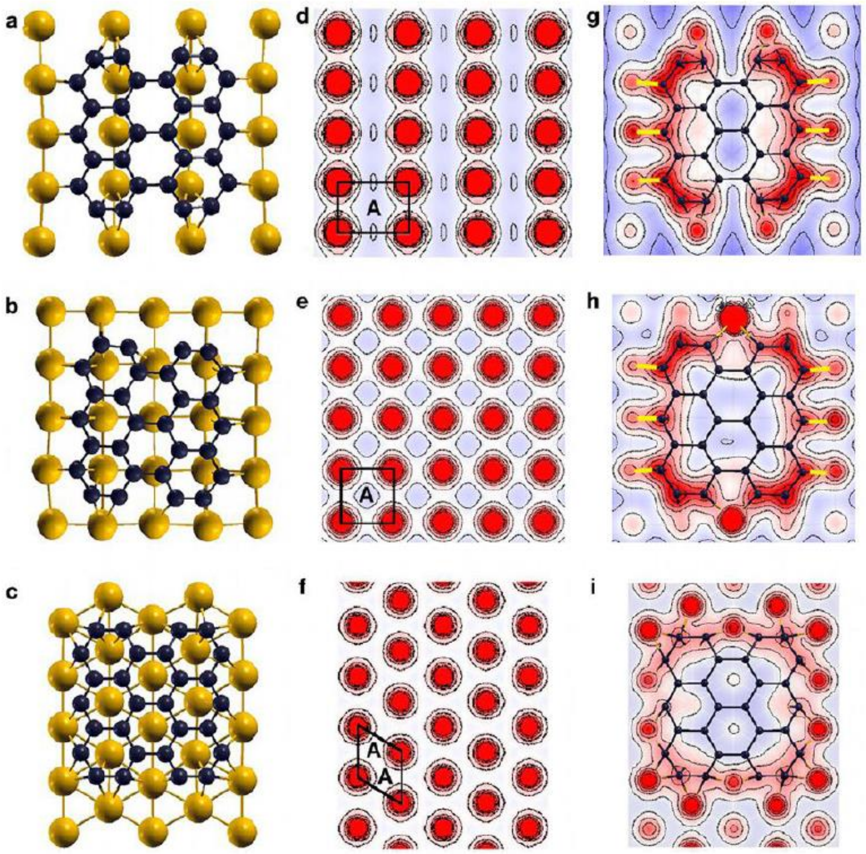

Figure 2-23. Computational modeling of graphene clusters on Cu{101}, Cu{001}, and Cu{111}. Red circles correspond to the surface atoms (high electron density), while regions with depleted electron density are equivalent to available adatomsites (labeled A). Strong one-to-one hybridization occurs along the Cu ⟨101⟩ direction between the electron orbitals of the zigzag edge atoms of C_{28} and Cu surface atoms on Cu(101) and Cu(001) indicated by yellow lines in g and h. Weaker one-to-two atom bonding between one C and two Cu atoms is observed on Cu(111). Reproduced from [18].

3 Experimental Setup and Characterization Tools

3.1 CVD Reactor

All graphene growth experiments presented in this thesis were carried out in a cold-wall reactor which operates under high vacuum conditions. I actively participated in the construction project, being responsible for all assembly and initial testing, as well as the project of complementary components. Services of welding and fabrication of parts such as ducts and connections were made in the machine shop of the physics department of UFMG.

The system consists of a cylindrical stainless steel chamber (*SS316)* with an internal diameter of 250 mm and height of 300 mm. It is connected to a turbo-molecular pump (Edwards HFA 301/451), which in turn is connected to a mechanical rotary pump (Edwards RV12). Note, however, that although the pumps are connected in series, the chamber can be pumped directly by the mechanical rotary pump as depicted in the diagram of Figure 3-1. This allows one to operate in low vacuum, 10^{-3} Torr, which is pretty much the ultimate limit of the mechanical pump. Naturally, when the mechanical pump is connected directly to the chamber, the turbo-molecular pump is isolated from the system by a Gate valve coupled to a *cf* flange 4-1/2". This operation is done manually.

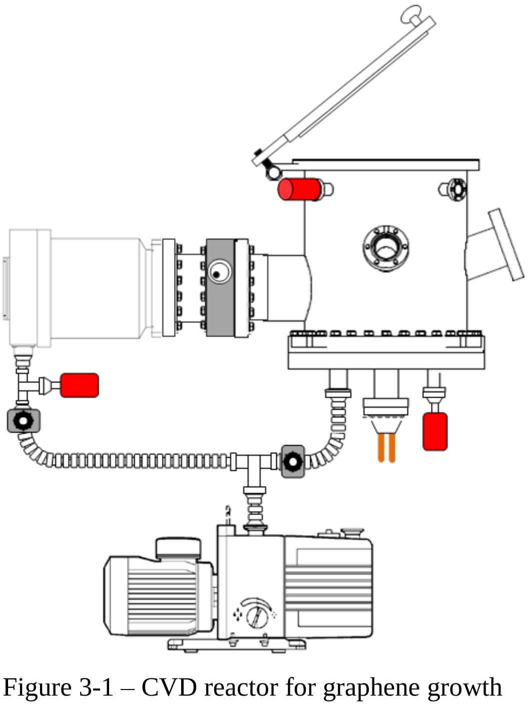

Figure 3-1 – CVD reactor for graphene growth

The pressure is monitored at the outlet of the turbo-molecular pump by a Pirani pressure gauge, and inside the chamber by another Pirani, and by a cold cathode gauge, which are connected as diagrammed in Figure 3-1(in red). Operating in high vacuum, with the two pumps working in series, it is possible to achieve pressures below 5×10^{-6} Torr in a short period of time (~ 30 min).

Inside the chamber, a resistive heater is suspended by two copper cylinders which are attached to an electrical feedthrough installed on a *cf* flange at the base of the chamber. Apart from serving as support for the heater, the copper pieces are also used to transfer the electrical power from an AC voltage source (which is connected to a voltage transformer) through the vacuum system wall, to the electrodes (carbon screws) connecting the heater (Figure 3-2)

Originally, the CVD reactor was put in operation using a commercial resistive heater made of pyrolytic graphite covered with pyrolytic boron nitride (Boralectric® Sample Heater, purchased from Tectra, Germany). However, after few months of usage, the heating element stoped working due the degradation of pyrolytic graphite in the contact. The perspective of the long waiting time that would be necessary to import another component encouraged us to produce our own heater. To this end, we carved in a graphite bar a very thin region which came to be the ohmic heater displayed in Figure 3-2 (b). The working area of this resistive circuit is 1 cm^2 and its thickness is approximately 0.5 mm. It can achieve temperatures up to 1300 ºC with currents near to 90 A. The effects of heat transfer by irradiation on sensors and connectors are attenuated by two concentric heat shields (confectioned in tantalum) surrounding the base of the heater. Air coolers are positioned on the outer walls of the chamber to help cool the system.

The sample temperature is monitored by a k-type thermocouple positioned under the surface of the heater. An optical pyrometer is also used to monitor the temperature uniformity over the surface. Radiation devices such this have the advantage of not having to touch the material being measured. Proper calibration permits the measure of temperatures with 5º C of precision.

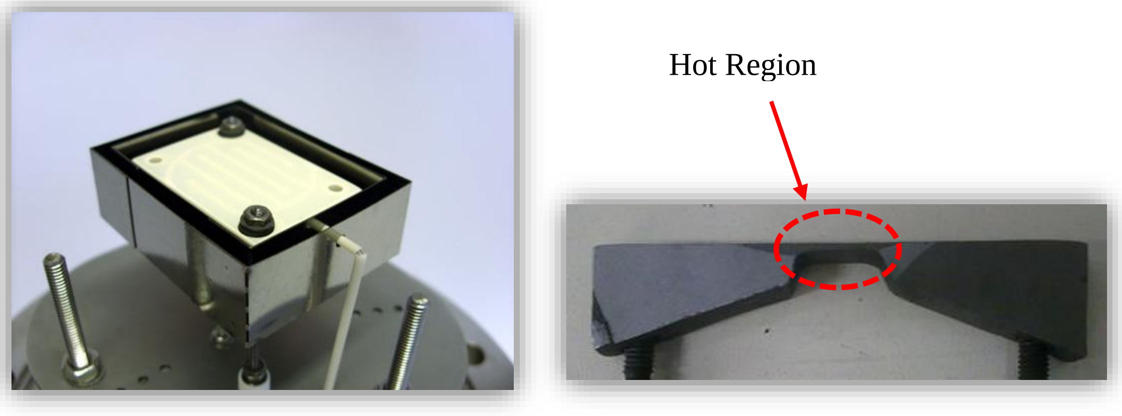

Figure 3-2 – (a) Commercial sample heater; (b) Homemade graphite heater.

Gaseous reactants are admitted into the reactor *via* a gas feedthrough connected to a gas mixer which is coupled to mass flow controllers (M100B MASS-FLO®) through a pipeline. Flow controllers for the gases methane, hydrogen and argon are currently installed, but a small change in the gas line allows the replacement of methane by ethylene. A photograph of the complete system is shown in Figure 3-3.

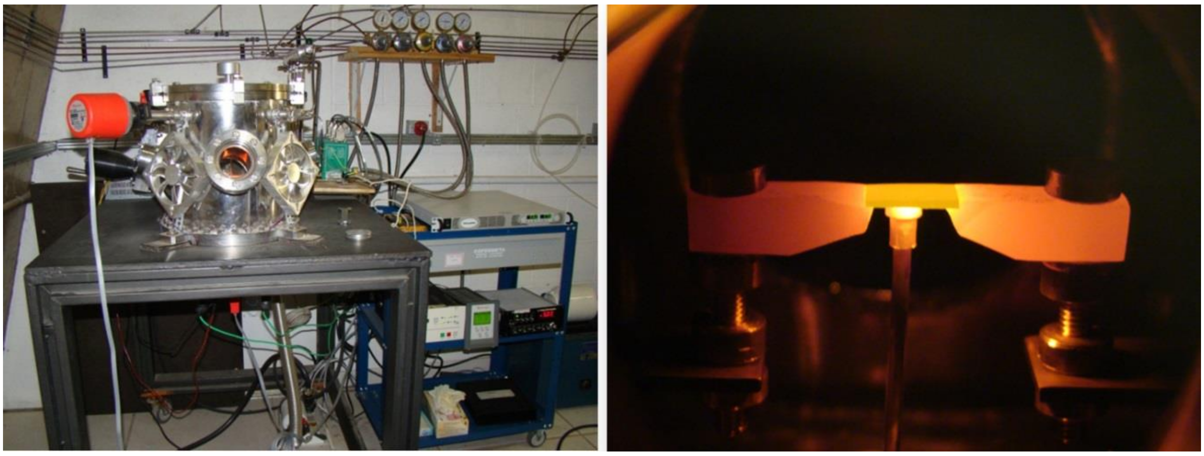

Figure 3-3 – Photography of the system built for graphene chemical vapor deposition.

Copper foils were placed on the heater mounted inside the chamber in order to serve as metal catalyst and substrate in the chemical vapor deposition of graphene. The growth routine and parameters sets are discussed in details in the following sections. However, it is worth to mention here that during the growth, graphene domains nucleated on the Cu surface and merge together to form a uniform graphene sheet as depicted in Figure 3-4. One can investigate either the film proprieties as well as graphene single-domains characteristics (before full surface coverage) by controlling the synthesis time. Both studies are presented in the next sections.

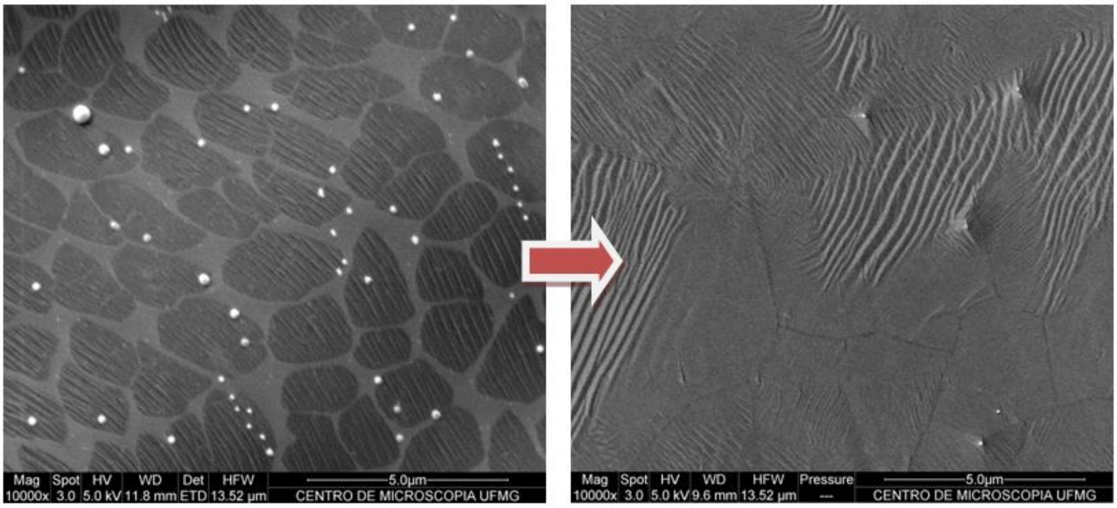

Figure 3-4 – Formation of a continuous graphene film by coalescence of monocrystalline domains of graphene.

3.2 Optical Microscopy Characterizations

Optical microscopy was employed to characterize the as-grown graphene immediately after the CVD growth. The major advantage of this technique is the possibility to access critical features of the grown graphene, such as grain size and morphology, in a fraction of the time usually demanded by other imaging methods (e.g. scanning electron microscopy).

The selective oxidizing of the underlying copper through thermal annealing in air enable the acquisition of high quality optical images of graphene grain boundaries as well as separated domains directly on the metal substrate, without the necessity to transfer the grown graphene to a Si/SiO$_2$ substrate. The reason for that is the increase of the interference color contrast between Cu and Cu oxide produced by the oxidation of the Cu regions uncovered with graphene (Figure 3-4).

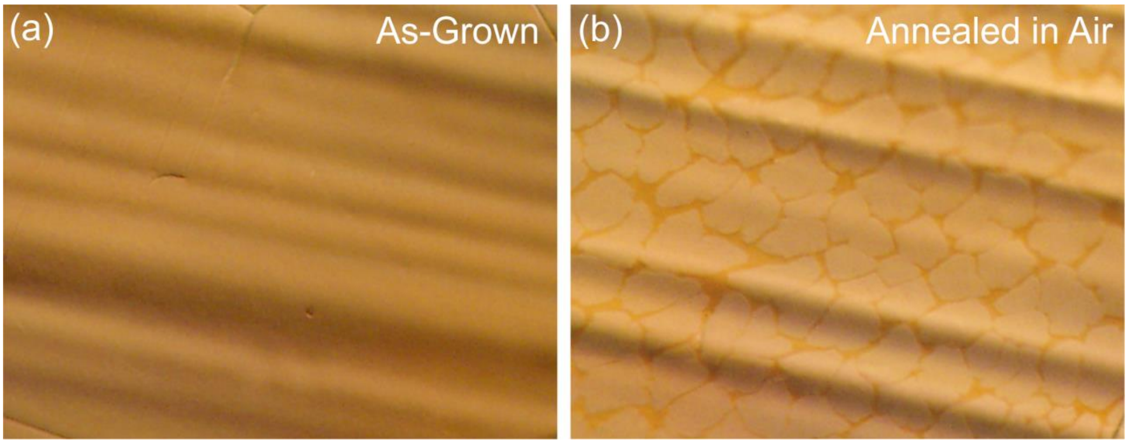

Figure 3-5 – Optical Image of graphene on Cu: (a) As-grown; (b) thermally oxidized in air after the growth.

The thermal oxidation of the graphene/copper samples were carried out in air on a hot plate at 200º C for 2 min. As the oxidation also damages graphene, only a portion of the sample was submitted to this process. The sample was cut into two pieces and one was held in reserve for other characterizations (i.e. Raman and SEM characterizations).

3.3 Raman Spectroscopy of Graphene

In Raman spectroscopy, the interaction between laser photons with molecular vibrations, phonons and/or other low frequency excitations of a target material causes a shift in the frequency of the scattered radiation (Figure 3-6). When the frequency of the inelastically scattered photon is lower than the frequency of the incident photon, the vibrational state of the target material is more energetic than its initial state, and the total energy of the system is conserved. This process is known as Stokes shift. Conversely, the anti-Stokes shift occurs when the frequency of the inelastically scattered photon is shifted to a higher value compared to the frequency of the incident photon, and the final vibrational state of the material is less energetic than its initial state. In both cases, inelastic scattering occurs because energy and momentum are transferred between the photons and the target material during the interaction [76].

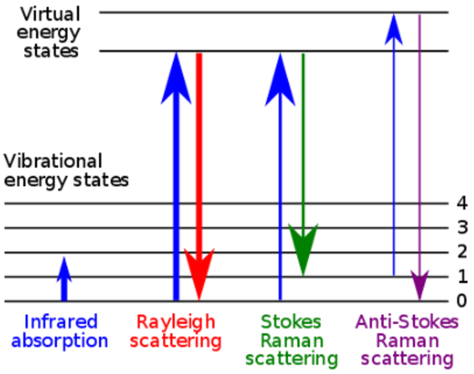

Figure 3-6 - Energy-level diagram showing the states involved in Raman signal.

The Raman spectrum of graphene is often used to identify modifications introduced during its preparation and processing, such as structural damage and chemical modifications. A great deal of detail on the graphene fine structure can also be extracted from the Raman data since the nature of Raman scattering on phonons is essentially determined by the behavior of the electrons in graphene (*i.e.*, how they move, interfere, scatter). Therefore, any variation of the electronic properties due defects, doping and strain should be expected to affects the Raman peaks positions, widths and intensities, allowing one to probe electrons by monitoring phonons [77].

The phonon dispersion of graphene can be calculated using a simple harmonic oscillator model taking into account the constraints imposed by the symmetry of the honeycomb lattice [78]. The phonon dispersion curves for the high symmetry points comprise three acoustic (A) and three optical (O) branches as depicted in Figure 3-7.

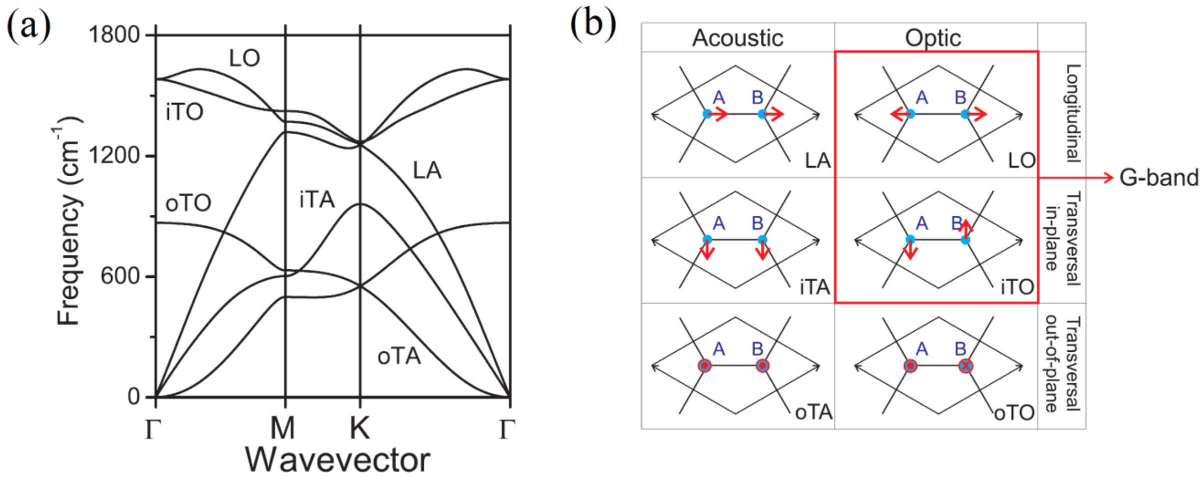

Figure 3-7 – (a) Phonon dispersion of monolayer graphene in the high symmetric directions calculated using the tight-biding method [79]. (b) Vibrations of the two atoms of the unit cell of monolayer graphene that correspond to the six phonon branches at the Γ point. Reproduced from [78].

At the ***Γ*** point, the iTO and LO modes are double degenerated and correspond to the vibrations of the sub-lattice A against the sub-lattice B as shown Figure 3-7 (b). These phonon modes belong to the two-dimensional representation E_{2g}, which is Raman active. The E_{2g} phonon mode gives rise to the so-called G band, which is seen as one peak in the Raman spectrum at around 1582 cm^{-1}.

The G band is a first order resonant Raman process, which occurs when a photon is absorbed by graphene, exciting an electron from the valence to the conduction band. This electron is then scattered by an E_{2g} phonon, emitting a photon after its recombination with a hole, as illustrated in Figure 3-8 (a). One common application for the G-band is in the determination of the strain and the doping level of graphene. It was observed that the G peak shifts to lower or higher energies values depending on the type and amount of doping (n or p) and/or strain (tensile or compressive) induced on the graphene sheet [80, 81].

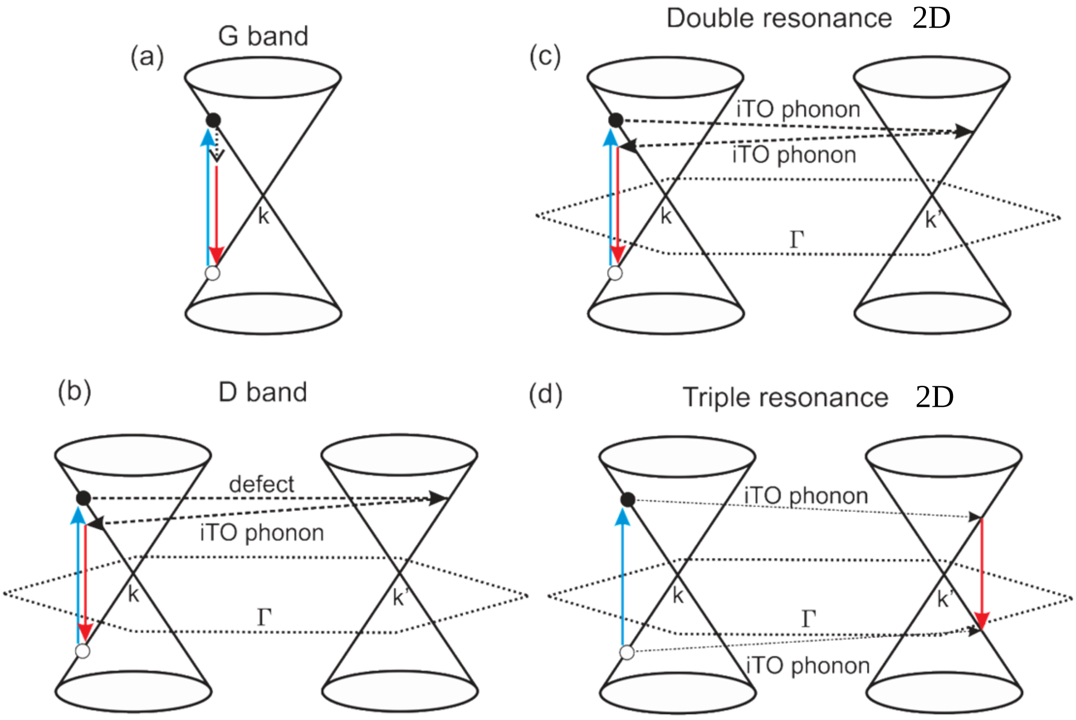

Figure 3-8 - (a) First-order Raman process which gives rise to the G band; (b) two-phonon second-order Raman spectral processes giving rise to the 2D band; (c) One-phonon second-order Raman process giving rise to the D band; (d) Schematic view of a possible triple resonance giving rise to the 2D Raman band in graphene. Adapted from [77].

The two other important bands in the Raman spectra of graphene are the D-band at ~ 1350 cm^{-1} and the 2D-band (or G'-band) at ~2685 cm^{-1}. [77, 76] The D-band is designated as the disorder band or the defect band and its intensity is proportional to the level of defects in the sample. It refers to the ring breathing mode of sp^2 carbon rings, which is active when the ring is adjacent to a graphene edge or a defect. The second order of the D-band, the 2D-band, do not represent defects and always displays a strong signal in the Raman spectra even when the D-band signal is negligible. The width of the 2D-band can provide information about the graphene layer thickness.

Both D and 2D bands exhibit a dispersive behavior, *i.e.* the position and the shape of these bands may vary significantly with different excitation laser frequencies. The origin of this behavior is related to a double resonance Raman process wherein the interaction between a photon and an electron near the K point induces the transition of the latter from the valence to the conduction band. Then, this electron is scattered by a phonon or a defect to a point belonging to the cone around the K' point, from where it is scattered back to the cone centered at K by another phonon. The subsequent recombination of this electron with a hole yields a photon emission. In the case of the D band, the scattering mechanism previously described outcomes from one elastic scattering event triggered by a crystal defect and one inelastic scattering event caused by the emission or absorption of an iTO phonon (Figure 3-8b). In the case of the 2D - band, both processes are inelastic scattering events involving two iTO phonons (Figure 3-8c). This double resonance mechanism is called an inter-valley process because it connects points in circles around inequivalent K and K' points in the first Brillouin zone.

The 2D band may also emerge as result of the scattering of holes in a process known as triple resonance Raman scattering [4,5]. In this process, the graphene system absorbs an incident photon and give rise an electron-hole pair around K point. Then, the electron is scattered by a phonon to a point belonging to the K' cone, similarly to what occur in the double-resonance model. However, in the triple resonance scattering a hole is also scattered by a phonon from the valence band around K to the valence band centered at K', in an intervalley process (Figure 3-8d). Next, the electron and the hole recombine, emitting a photon in the process [76, 77]. The triple-resonance condition is used to explain the higher intensity of the 2D-band compared to the G-band in the monolayer graphene.

The quality of as-grown CVD graphene can be evaluated by analyzing the peak intensity ratio of the 2D and G bands. In fact, a large value for the ratio I_{2D}/I_G as well as the lack of a D band can be often interpreted as signature of high quality defect free graphene. Moreover, the spectra exhibit a sharp symmetric 2D-band in the case of single layer graphene.

3.4 Electron Backscatter Diffraction

3.4.1 Fundamentals of Electron Backscatter Diffraction

Electron backscatter diffraction (EBSD) is a powerful method for quantitative microstructural information about the crystallographic nature of metals, minerals, semiconductors, and ceramics. The analysis of the EBSD patterns can provide key information about the crystallographic orientation, texture and phase identity of a particular material in a non-destructive way and with minimum specimen preparation.

The discovery of the fundamental diffraction on which the EBSD is based can be traced back to 1928 [82] but just posterior advances made in the hardware and software used to capture electron backscatter patterns on an automatic basis allowed EBSD to become practical. Today, EBSD is a common analytical tool based on an accessory system that can be equipped on most scanning electron microscopes (SEM), as illustrated in Figure 3-9.

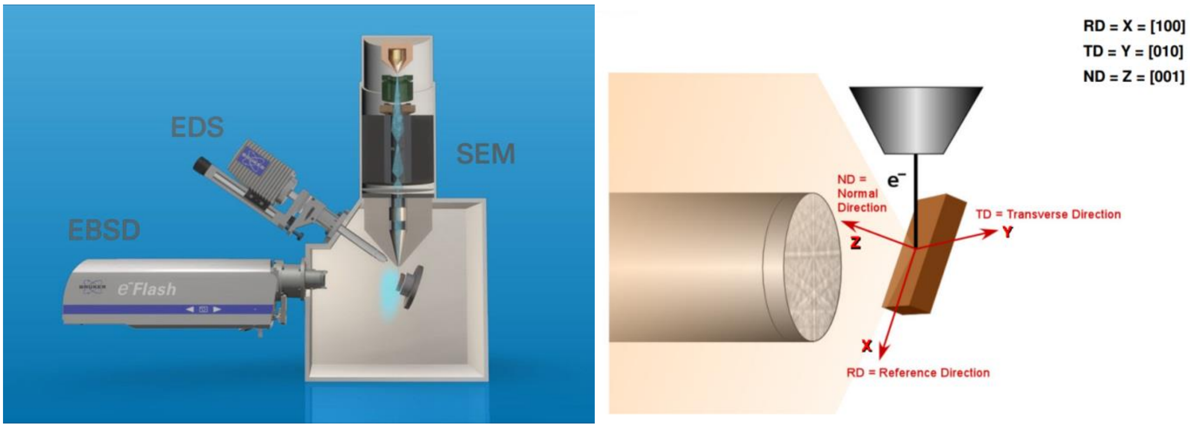

Figure 3-9 – Basic EBSD setup

In a typical EBSD measurement, a flat, highly polished specimen is positioned at the SEM sample stage, which is used to tilt the plane of the sample to a shallow angle, typically 20° respectively to the incident beam. The primary beam interacts with the crystal lattice producing low energy loss backscattered electrons that are channeled and subject to different paths, leading to constructive and destructive interference [82]. The set of directions that backscattered electrons can take satisfying Bragg condition is the surface of a cone at each side of the lattice plane [83] as illustrated in Figure 3-10. These cones are called Kossel-cones and due to its flatness, their area of interaction with the detector screen appears as bands, known as Kikuchi bands.

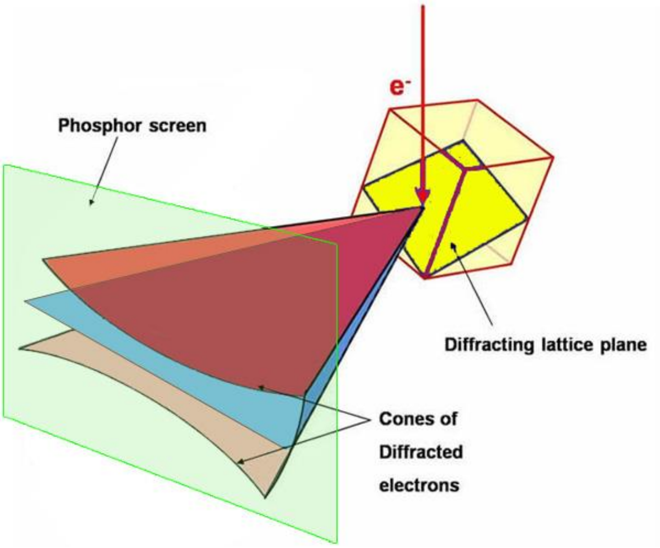

Figure 3-10 – (a) Bragg -reflection of electrons from a local electron source Q at the (010) and (021) lattice planes leading to a signal on the detector screen; (b) Position of the Kossel cones of a lattice plane in respect to the detector. Adapted from refs [83] [84].

The process which determines the actual indexing of the Kikuchi bands involves comparing the information derived from the pattern obtained experimentally with the theoretical values for reflectors in known phase reference tables. In general, specialized computer software analyzes the EBSD pattern by detecting a number of Kikuchi bands using an optimized Hough transform. Basically, the *Hough transform* converts the Kikuchi bands (Figure 3-11 (a)) to points in Hough space (Figure 3-11 (b)), which are easier to be localized and identified by an image processing software [84]. The software determines all possible orientations with each phase and reports the best fit, with the deviation from the reference data (Figure 3-11 (c)). Each Kikuchi band is then indexed by the Miller indices of the diffracting crystal plane which formed it (Figure 3-11 (d-e)). With a *priori* information about the candidate material under the beam, EBSD can be used to provide a complete crystal orientation map of a polycrystalline sample as depicted in Figure 3-12.

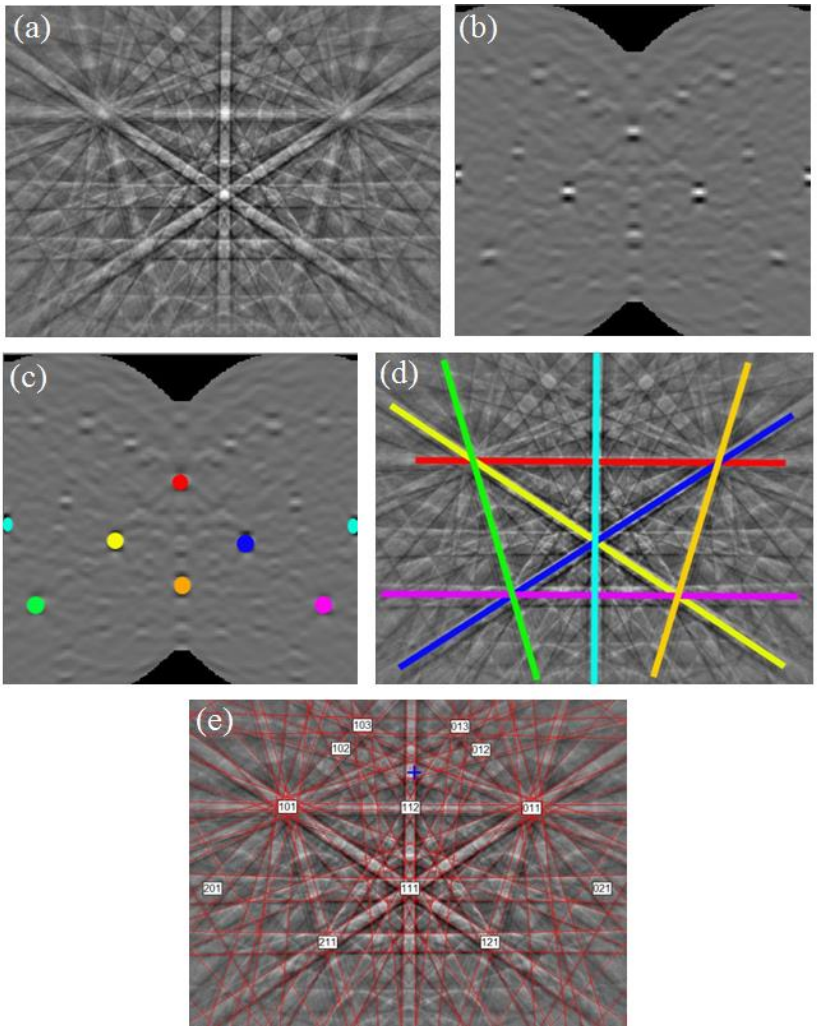

Figure 3-11 - Sequential steps of EBSD processing. (a) Kikuchi bands of the diffraction pattern collected from silicon; (b) Hough transform of the Kikuchi bands obtained in (a); (c) Identification and fitting of the points obtained in (b) by comparing it with the values known from reference tables. (d) Inverse Hough transform of the peaks found in (c). (e) Original diffraction pattern indexed by the Miller indices. Reproduced from Ref. [84].

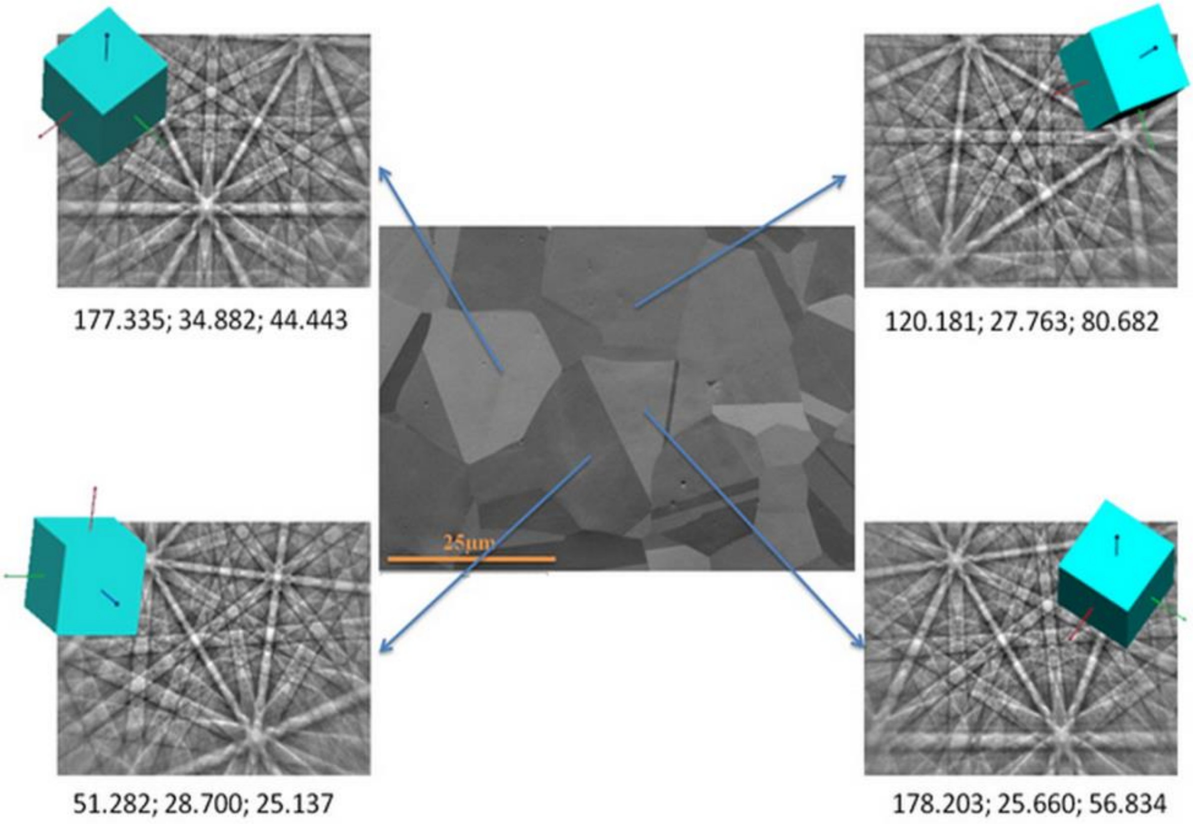

Figure 3-12 – Grain orientation map of a polycrystalline sample obtained via EBSD. Reproduced from [84].

The spatial resolution of the EBSD map is determined by the SEM electron optics as in conventional backscattered electron imaging. The EBSD detector generally consists of a CCD chip illuminated by a phosphor screen that intersects the spherical diffraction pattern. The phosphor converts the diffracted electrons into light suitable for the CCD camera to record. The accelerating voltage of the incident beam range from 10–30 kV, and the currents, 1–50 nA. Modern EBSD equipment allows the automatic acquisition, analyzing and storage of diffraction patterns.

3.4.2 EBSD Data – Inverse Figure Pole

The stereographic projection allows one to represent 3D directions in two dimensions. That is, a point P on the surface of a sphere can be represented by its projection at the equatorial plane of the sphere as depicted in Figure 3-13 (a-b). If a sample with a cubic unit cell were placed at the center of the projection sphere with its principal axes aligned with the axes of the sphere, then the crystal directions and plane normals can be projected onto the equatorial plane as displayed in Figure 3-13 (c-d).

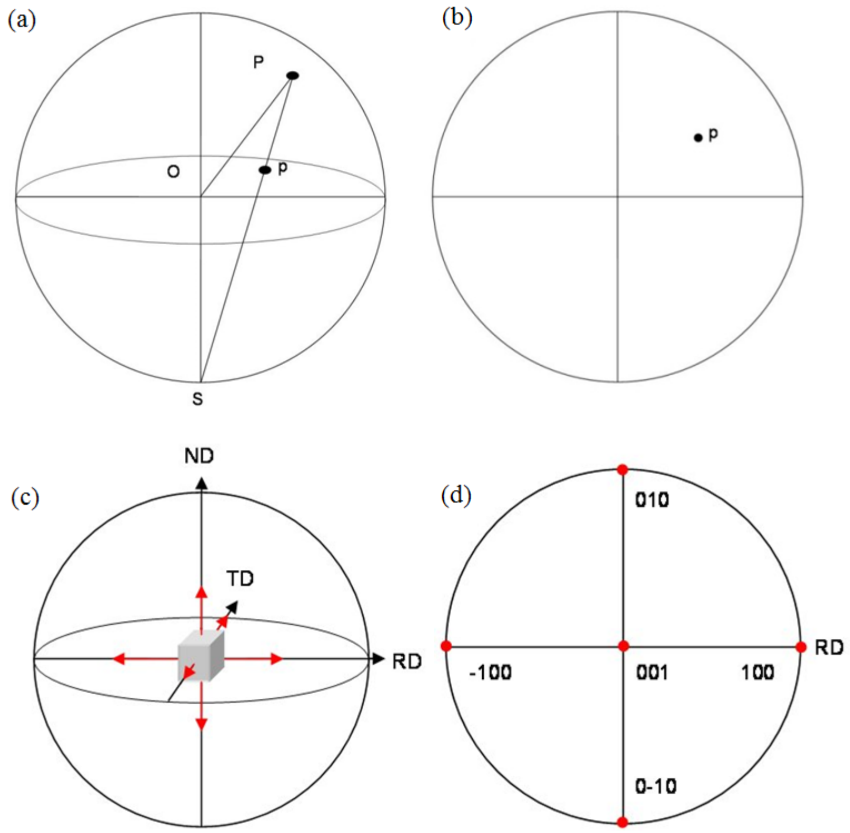

Figure 3-13 -(a) Projection of a point P on the surface of a sphere onto the equatorial plane at p; (b) The stereographic projection of the point P; (c) A cubic unit cell placed at the center of the projection sphere with its six {001} plane normals (poles) highlighted; (d) A stereographic projection of the directions shown in (c). Reproduced from [84].

As can be seen in the Figure 3-13 (c-d), the stereographic projection generates a set of equivalent points corresponding to the symmetrical directions of a particular crystal. However, to describe a *family* of equivalent crystallographic directions, the “unit triangle” shown in Figure 3-14 is more appropriate [84]. This triangle corresponds to the inverse pole figure (IPF) of a cubic crystal and is defined in such way that any of the crystallographically symmetrical equivalent directions assigned to a particular sample appears only once. In general, the IPF of given crystal is determined by the stereographic projection of the point group of the corresponding crystal Laue class.

Inverse pole figure orientation component uses a basic RGB coloring scheme. In cubic phases, full red, green, and blue are assigned to grains whose surface-normal direction are

<100>, <110> or <111>, respectively. Intermediate orientations are colored by an RGB mixture of the primary components [82], as seen in Figure 3-14.

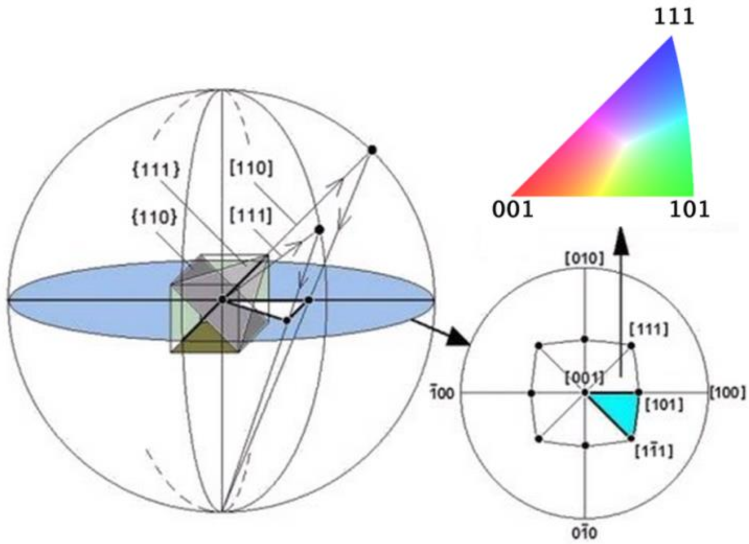

Figure 3-14 – Construction of the inverse pole figure. Only one stereographic triangle is required to describe a family of equivalent crystallographic directions because all triangles in the stereographic projection are symmetrically equivalent. Adapted from [84].

3.5 Transferring Graphene

For various applications, graphene grown by chemical vapor deposition must be transferred from the metal catalyst to a different substrate. This is a critical step in graphene production as the single atom layer is quite fragile and can suffer significant mechanical damage during the process. In the next sections we will discuss the two most successful methods utilized in this work to transfer the graphene grown on the Cu foil to silicon dioxide/silicon (SiO_2/Si) substrates.

3.5.1 Cu dissolution transfer method

The most common method used to move graphene from a metal onto another substrate involves a sacrificial polymer layer [10, 85]. The general idea of this method is to attach a polymer (poly-methyl –methacrylate, or PMMA for shorter) to the graphene side and then dissolving the metal on the opposing side in an etchant bath. The resultant polymer/graphene complex is then placed upon the target substrate, and the sacrificial polymer layer is removed by a solvent (Figure 3-15). This procedure takes several steps as we will describe next.

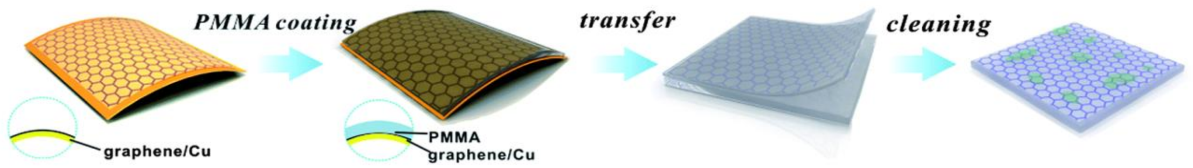

Figure 3-15 – Schematic illustration of graphene transfer from Cu foil to an arbitrary substrate. Reproduced from

The deposition of the polymer onto graphene is carried out *via* spincoating. In this process, liquid PMMA (950-C2) is laid onto graphene, and then spun at high speeds (~2500 RPM) for 60 seconds. The sample (Metal/Graphene/PMMA) is then cured on a hotplate at 160º C for 5 min, resulting in a smooth uniform layer of PMMA firmly attached to the graphene, and having a thickness no greater than 300 nm. This layer safeguard graphene during the oxygen plasma etching which is employed to remove the graphene grown on the opposite side of the substrate, the one not covered by PMMA. Moreover, it also protects graphene from cracks and tears due to physical disturbances.

Next, the metal is dissolved in an etchant bath of 0.1 M of ammonium *persulfate,* $(NH_2)_4S_2O_8$, for 24h. After the dissolution of the metal, all traces of any etchant used must be washed off in multiple baths of deionized water. This is done by moving the floating layer of PMMA-graphene from on bath to another through a “fishing out” procedure, wherein a piece of Si/SiO_2 is used as transfer base. One should be very careful during this stage, as the graphene layer is exposed on the polymer. The PMMA-graphene layer is then fished out one last time by the desired substrate and left to dry. We note that heating the substrate with the PMMA-graphene stack on top allowed the PMMA to become malleable, thereby relaxing on the substrate surface and enhancing the graphene contact with the substrate.

The polymer is removed letting the sample sit in acetone overnight, and then rinsing it with isopropyl alcohol (IPA) and blown it dry with nitrogen.

3.5.2 Electrolysis induced H_2 bubbling transfer method

In this method, graphene can be readily detached from the metal catalyst by H_2 bubbling resulting from H_2O electrolysis [85]. It is much faster than the dissolution transfer method since the electrolysis takes just few minutes to separate graphene from copper. In addition, this technic does not require many washing stages compared with the transfer route that use etchant solution.

Spin coated PMMA is also used as the supporting polymer thin film in this transfer process. Similarly, the graphene on the bottom face of the foil is dry etched by O_2 plasma as described in previous section. The PMMA/graphene/Cu-bundle is then used as the cathode of an electrolytic cell with 0.25M NaOH aqueous solution electrolyte. For the anode, a platinum electrode is used (Figure 3-16). To start the process, the current is ramped to ~1A and maintained at that level until the graphene is completely separated from the Cu foil by the H_2 bubbling. The typical time required for separation is 1-5 min. Once detached from the metal, the PMMA/graphene-bundle is picked up and rinsed in deionized water bath. Next, it is placed on the target substrate and left at room temperature until it gets dry. The removal of the PMMA layer is done in the same manner described in the previous section.

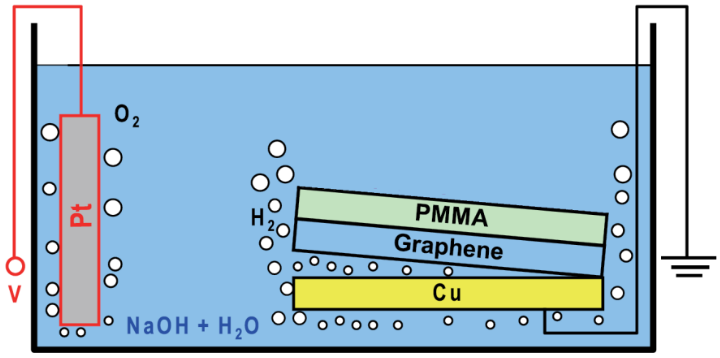

Figure 3-16 - H_2 bubbling separation of the frame/PMMA/graphene from the Cu foil induced by H_2O electrolysis. Adapted from [85].

3.6 Electrical Characterizations

3.6.1 Graphene Field Effect Transistor (G-FET)

The ability to modify the electronic properties of a material by applying an externally voltage is the core of modern electronics. It allows one to vary the carrier concentration in a semiconductor device and, as a result, change the electric current passing through it. Therefore, it is not surprise that the outstanding carrier mobilities found in graphene field effect transistors (GFETs) has propelled an extensive amount of research in graphene based device. The most often studied GFET is the back-gated configuration shown in Figure 3-17, wherein graphene is contacted to form source and drain electrodes and the silicon and silicon dioxide of SiO_2/Si substrate serve as back gate electrode and dielectric, respectively. [86]

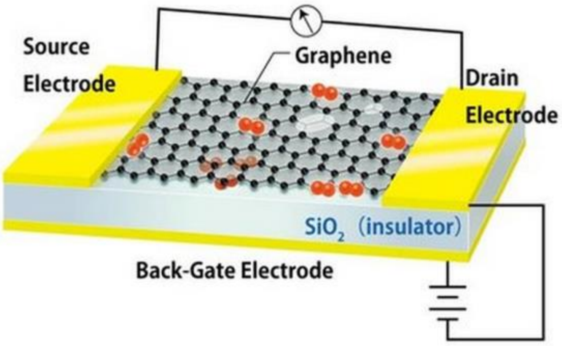

Figure 3-17 – Graphene based back-gated field effect transistor [87].

The peculiar shape of graphene π-band around the points K and K', referred as "Dirac cones", accounts for grafene's intrinsic electrical transport characteristics. As previously discussed (section 2.1.2), the energy has a linear dispersion behavior in this region [26]:

$$\epsilon(k) = \pm\hbar\nu_F|k| \qquad \text{eq. 3-1}$$

where ν_F is the Fermi velocity ($\approx 10^6$ m/s). The Fermi wavevector for all 2D systems is given by filling up the non-interacting momentum eigenstates up to q = k_F,

$$n = g_s g_v \int_0^{K_F} \frac{dq}{(2\pi)^2} dk = \frac{{k_F}^2}{\pi} \quad \rightarrow \quad k_F = \sqrt{n\pi} \qquad \text{eq. 3-2}$$

where n is the density of charge carriers per unit area [88], and g_s and g_v (both equal 2) are the degeneracies of spin and valley, respectively. Substituting eq. 3-2 in eq. 2-11, one obtains:

$$\epsilon(k_F) = \hbar\nu_F k_F = \hbar\nu_F\sqrt{n\pi} \qquad \text{eq. 3-3}$$

As a result, the Fermi level energy of graphene can be tuned near the Dirac point through selective control of the carrier concentration, n, which can be modulated by biasing the gate terminal. The amount of charge injected by the application of the electric field can be easily calculated since the system behave like a parallel-plate capacitor,

$$q = ne = cV_G \qquad \text{eq. 3-4}$$

where q is the total charge injected into the material per unit area, V_G is the applied voltage at the gate, and c is the capacitance per unit area, given by $c = \varepsilon_0\varepsilon_{ox}/d$, where ε_0 is the electric permittivity of vacuum, ε_{ox} is relative permittivity of SiO_2 and d is the width of the SiO_2 layer, namely the distance between Si and graphene. By rearranging equation eq. 3-4, one can write:

$$n = \frac{c}{e}(V_G - V_{CNP}) \qquad \text{eq. 3-5}$$

where V_{CNP} is the voltage at the charge-neutrality point, for which the source-drain conductance is minimal. For undoped graphene, $V_{CNP} = 0$. However, at ambient conditions, the samples are often found to be p-type doped materials due to unintentional doping caused either by the condensation of water vapor, present in air, onto graphene surface, as well as by residues of the PMMA used during the graphene transfer and photolithography. In this circumstances, $V_{CNP} > 0$, and the energy of the last occupied state in function of the gate voltage assume the form:

$$\epsilon(k_F) = \hbar \nu_F \sqrt{\frac{c}{e}\pi(V_G - V_{CNP})} \qquad \text{eq. 3-6}$$

To describe the behavior of the source-drain conductivity with the gate voltage, one may invoke the semi-classical conductivity equation, $\sigma = en\mu$, wherein μ is the carrier mobility, given by $\mu = e\langle\tau\rangle/m^*$. The effective mass can be written as $m^* = (2\epsilon_F/{\nu_F}^2)$, [88] which leads to:

$$\sigma = e^2 \frac{\epsilon_F}{\pi\hbar^2}\langle\tau\rangle \; = \; \frac{e^2 \nu_F}{\pi\hbar}\left(\sqrt{\frac{c}{\pi e}(V_G - V_{CNP})}\right)\langle\tau\rangle \qquad \text{eq. 3-7}$$

where $\langle\tau\rangle$ is the relaxation time, and depends on the type and rate of scattering processes which mobile charge carriers are subjected. Moreover, graphene FETs have an ambipolar conduction behavior, *i.e.* either electrons as well as holes can dictate graphene electrical conduction comportment depending on the chemical potential (Fermi level) of the system, which in turn, can be modulated by an external voltage applied at the back-gate. In fact, by applying a negative bias on the Si gate, electrons are removed from graphene, shifting the Fermi level to below the Dirac point. As result, the electrical transport at this half-filled band configuration occurs mainly due to the positive carriers, *i.e.* holes. On the other hand, the application of positive bias at the back-gate produces an increase of the number of electrons embedded in graphene, shifting the Fermi level to above the Dirac point. Again, a half-filled band configuration is established, but at this time, the electrons are the major charge carriers. Figure 3-18 illustrates the behavior of the intrinsic resistivity and conductivity of undoped graphene as a function of applied gate voltage. For V_G = 0V, the Fermi level lies exactly between the conduction and valence bands. The occurrence of a minimum non-zero value of conductivity at this point reflects the inexistence of a band gap in graphene band-structure. Indeed, the graphene FET channel has a low resistance modulation ratio ρ_{on}/ρ_{off} ~6. This ratio, often referred as current ratio I_{on}/I_{off}, does not exceed 10 at room temperature, and for this reason, the use of graphene for logic devices, where the minimum required I_{on}/I_{off} exceeds 10^3, is unfavorable. Nevertheless, graphene was found to be attractive for high-frequency electronics, where transistor current gain is more important than I_{on}/I_{off} [86].

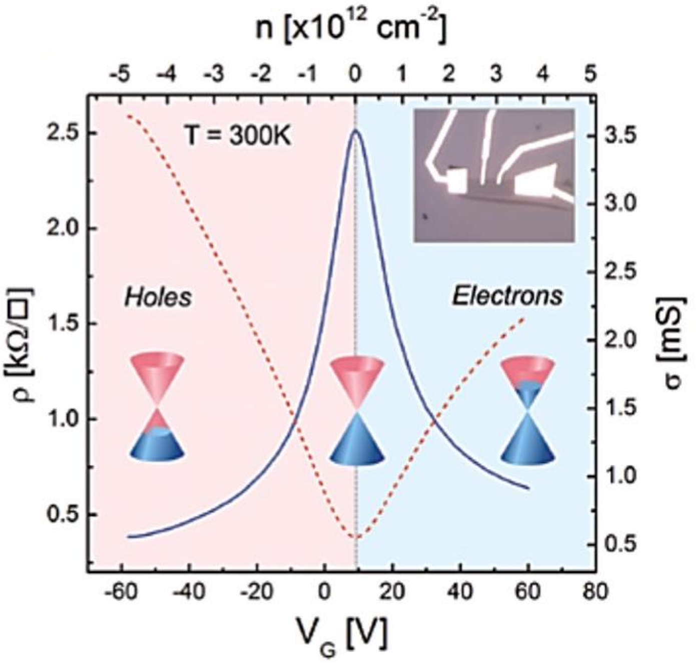

Figure 3-18 - typical transfer curve for a single-layer graphene transistor: channel resistivity (blue line) and channel conductivity (red dashed line) vs. gate voltage. Adapted from [89].

It turns out that disturbances in graphene electronic structure produced by its interaction with the underneath substrate or by the presence of defects and adsorbed impurities may produce significant decrease of GFET conductivity. In particular, the field effect mobility of the charge carriers, μ, degrades significantly due to extrinsic scattering mechanisms [90, 91, 92], which contribute to the reduction of the mean free path and the relaxation time. Hence, the measurement of μ is often used to evaluate the quality of the synthesized graphene. The carrier mobility can be obtained from:

$$\mu = \frac{1}{e}\left(\frac{d\sigma}{dn}\right) = \frac{1}{c}\left(\frac{d\sigma}{dV_g}\right) \qquad \text{eq. 3-8}$$

where the derivative term can be estimated from the linear region of the curve $\sigma \times V_g$ (Figure 3-18). However, is more common to use the curve of transconductance (I_{SD} x V_G) to obtain the electron mobility. In this case, equation eq. 3-8 can be rewritten as:

$$\mu = \frac{L}{cWV_{SD}}\left(\frac{dI_{SD}}{dV_g}\right) \qquad \text{eq. 3-9}$$

where W is the width and L is the length of graphene channel and I_{SD} and V_{SD} are the current and voltage between source and drain, respectively.

3.6.2 Device Fabrication

Graphene device fabrication begins with the spin coating of thin layer of the photo-sensitive resistor over the surface of the graphene film which was previously transferred to the Si/SiO$_2$ substrate. In this process, liquid positive photoresist S1805 is laid onto the sample and then it is spun at high speeds (~1000 RPM), thereby spreading the coating material uniformly over the surface. The polymer is then cured on a hot plate at 100 ° C for 1 min.

Next, a pattern previously created in a CAD program is written direct on the photoresist by a laser writer machine (Microtech LW405) which uses a laser of 405 nm to scan the sample along the xy-axis. This process transfer the desired pattern to the photoresist in the same way an inkjet printer transfer a pattern to a sheet of paper. The sample is then immersed in a developer solution (MF321) that removes the exposed photoresist, revealing the graphene layer upon which metal will be evaporated in the following step. The deposition of 5 nm of Cr prior the deposition of 50 nm of Au is necessary in order to improve the adhesion of the electrical contacts with the substrate.

The remaining photoresist is removed in a bath with acetone, in a process known as lift-off [93] which leaves only the contacts of Cr/Au. A new layer of photoresist in then deposited onto the sample and optical lithography is used to pattern the graphene film. Once again, the exposed photoresist is removed, but this time it reveals the graphene region which will be etched by a RIE plasma of Ar/O$_2$. This plasma removes the exposed graphene but leaves intact the material protected underneath the resist layer. The process ends with a final lift-off step. The entire procedure is schematized in Figure 3-19.

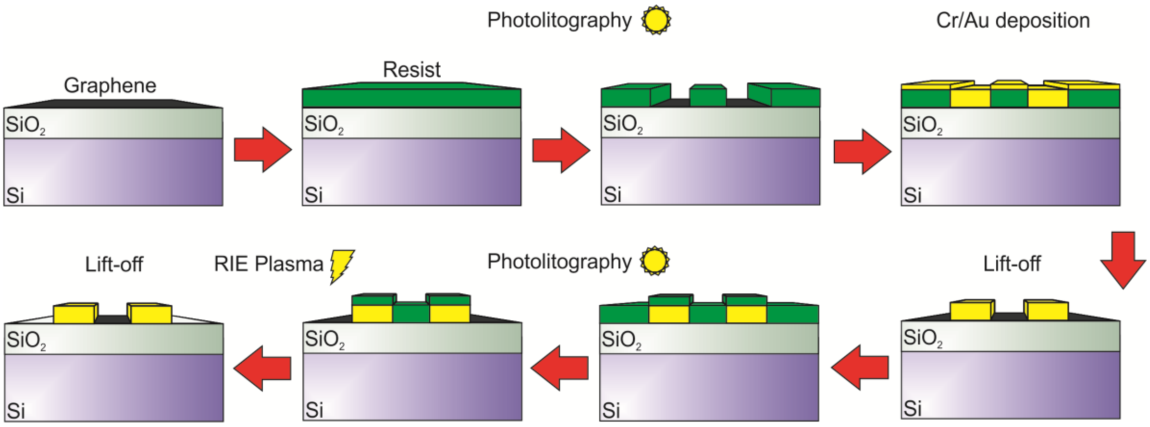

Figure 3-19 – Sequential steps of G-FET production.

4 Results and Discussion

4.1 Cu-Catalyzed Methane-Based graphene CVD

The synthesis of graphene was initially performed following the near standard conventional procedure reported in the literature [72], which is described next.

Commercially available 25 μm thick copper foils were placed on the graphite-heater mounted inside the homebuilt stainless steel chamber as described in section 3.1. The chamber was pumped to below 10^{-6} Torr in order to remove as much air as possible. The copper foils were then annealed at 900 °C for 30 min in a hydrogen environment in order to remove the oxide layer from the copper surface. This thermal treatment also served to increase the grain size of the copper and to remove any structural defects of the surface, which could compromise the quality of the resulting graphene film [94]. Methane was supplied as carbon precursor at a rate of 1 sccm diluted in 10 sccm of hydrogen for 20 s to 30 min in order to grow graphene. The total pressure in the reactor was on the order of 10^{-3} Torr and the temperature was in the 850-950 °C range. After the growth, the samples were cooled down to room temperature in vacuum.

4.1.1 The Temperature Dependence of Graphene Films

The influence of the growth temperature on the quality of the resulting graphene was investigated by comparing several individual samples that were grown at different temperatures in the interval of 870 °C to 910 °C. For a better understanding of its effect over the size of graphene grains, we used a short growth time to avoid full graphene coverage as depicted in Figure 4-1.

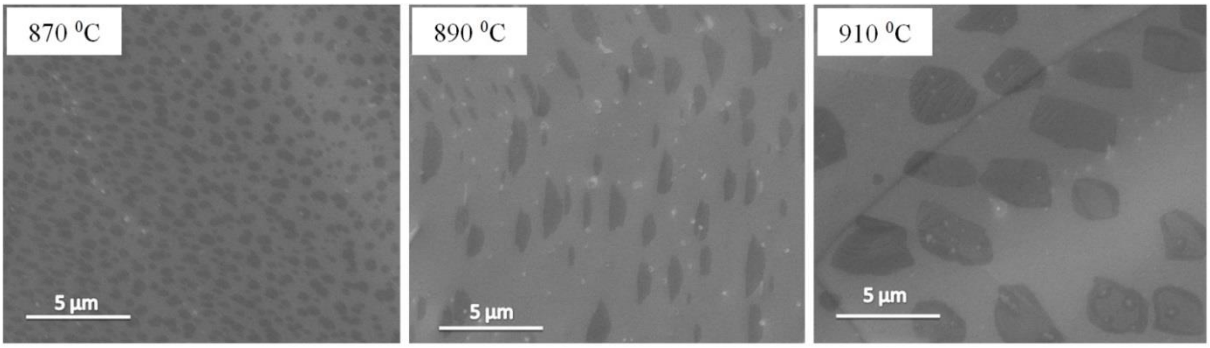

Figure 4-1 - SEM images of graphene domains grown at different temperatures.

For longer growth times, the graphene fully covers the copper foil. The resultant film is an intricate patchwork of grains connected by tilt boundaries, which size and density strongly depends on the growth temperature. By comparing the Raman spectra (Figure 4-2) of graphene films grown at the same temperatures of the samples showed in Figure 4-1, it is clear that there is more defect formation at lower temperatures and that the quality is significantly better for higher growth temperatures. The D/G ratio follows a clear trend, decreasing as the temperature increases, whereas the 2D/G ratio shows the opposite trend, increasing with the temperature.

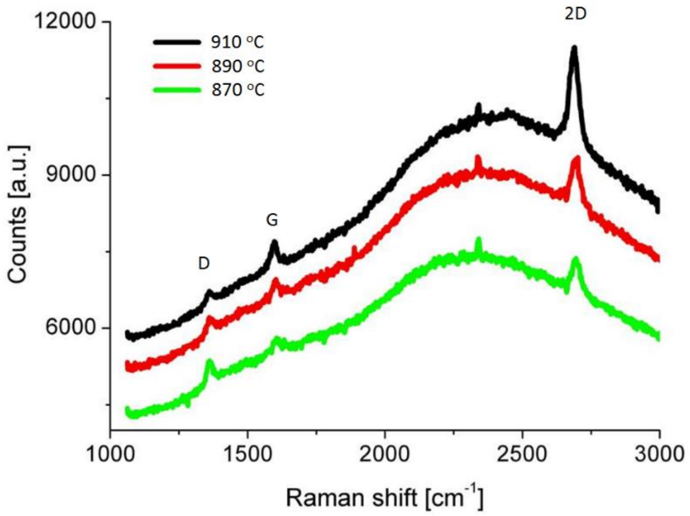

Figure 4-2 - Raman spectra of graphene films grown at different temperatures. The photoluminescence of the copper substrate produces a strong background in the Raman spectra.

The full width at half maximum (FWHM) of the 2D peak is also large (~40 cm^{-1}) in the samples grown in lower temperatures, which could be due to the existence of more layers of graphene than a single monolayer [95]. It can also be due to several small grains of monolayered graphene being probed at the same time. The 2D peak is then broad due to integration over different graphene grains, which each contribute a single sharp Lorentzian peak in the spectrum. This results in a Gaussian distribution of Lorentzians, which can be fitted with a Voigt function, as seem in Figure 4-3.

Based on these results, we can understand the growth process as follows. At low temperatures, carbon species quickly nucleate new domains rather than move on the copper surface and enlarge existing domains. That is, the surface mobility of the carbon precursor on the copper surface is low at low temperatures. At high temperatures, on the other hand, the carbon species moves longer distances on the copper surface and expands an existing graphene grain instead of creating a new one. The desorption of carbon species may play an important role in this process. Although it can be negligible at low temperatures (T< 850 °C), desorption may become important at high temperatures, resulting in desorption-limited growth. [96, 37] Namely, the increased rate of re-evaporation of active carbon species at high temperatures (which may also be related to the substrate sublimation) causes that fewer nucleation sites are formed, leading to larger graphene monocrystalline domains, which are crucial to minimize the amount of defects in the resulting film.

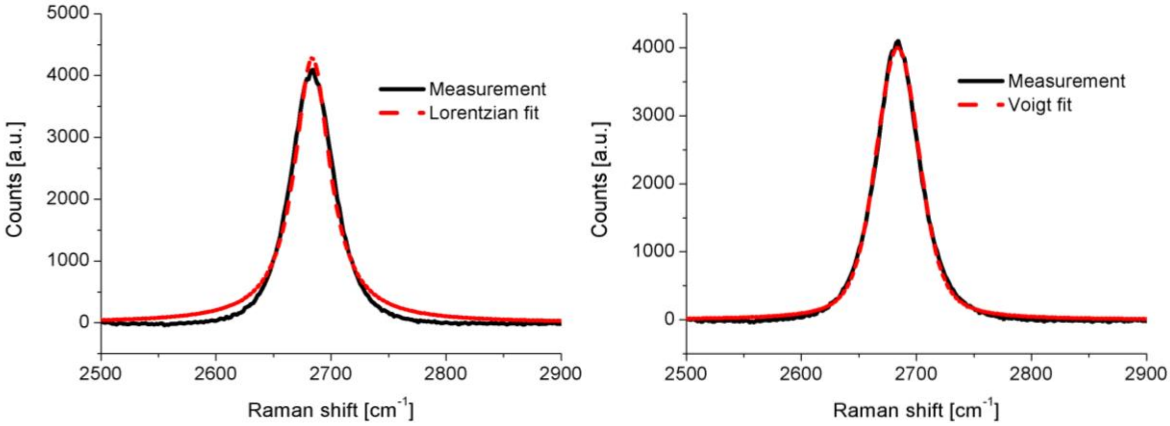

Figure 4-3 - Comparison of bad Lorentzian fit and good Voigt fit of the same spectrum.

It is worth to mention that the increase of the rate of desorption of carbon species may be related to the increase of copper sublimation at higher temperatures. In fact, we present in section 4.2.2 strong evidence that copper sublimation and self-diffusion severe impacts graphene growth under low background pressure.

4.1.2 Film Strain

It has been shown that an enclosure of copper foil can be an interesting way to grow graphene. This configuration limits the concentration of the carbon feedstock on the inside of the enclosure (also called envelope), leading to the growth of large graphene grains [97]. Similarly, the carbon concentration can be limited on the bottom side of a flat copper foil which lies over a plane surface. Since the copper foil can never be completely flat on a microscopically scale, there will always be different channels for the carbon precursor to reach the surface, which allow graphene growth on the bottom side of the Cu foil. This creates a gradient where more of the carbon precursor reaches the edges of the sample whereas less carbon can react with the central parts. This novel substrate/catalyst architecture provides means of studying the coalescence of graphene domains during the film formation. As can be seen in Figure 4-4 (b), the gradient in carbon concentration yields a transition from fully covered graphene to individual graphene domains.

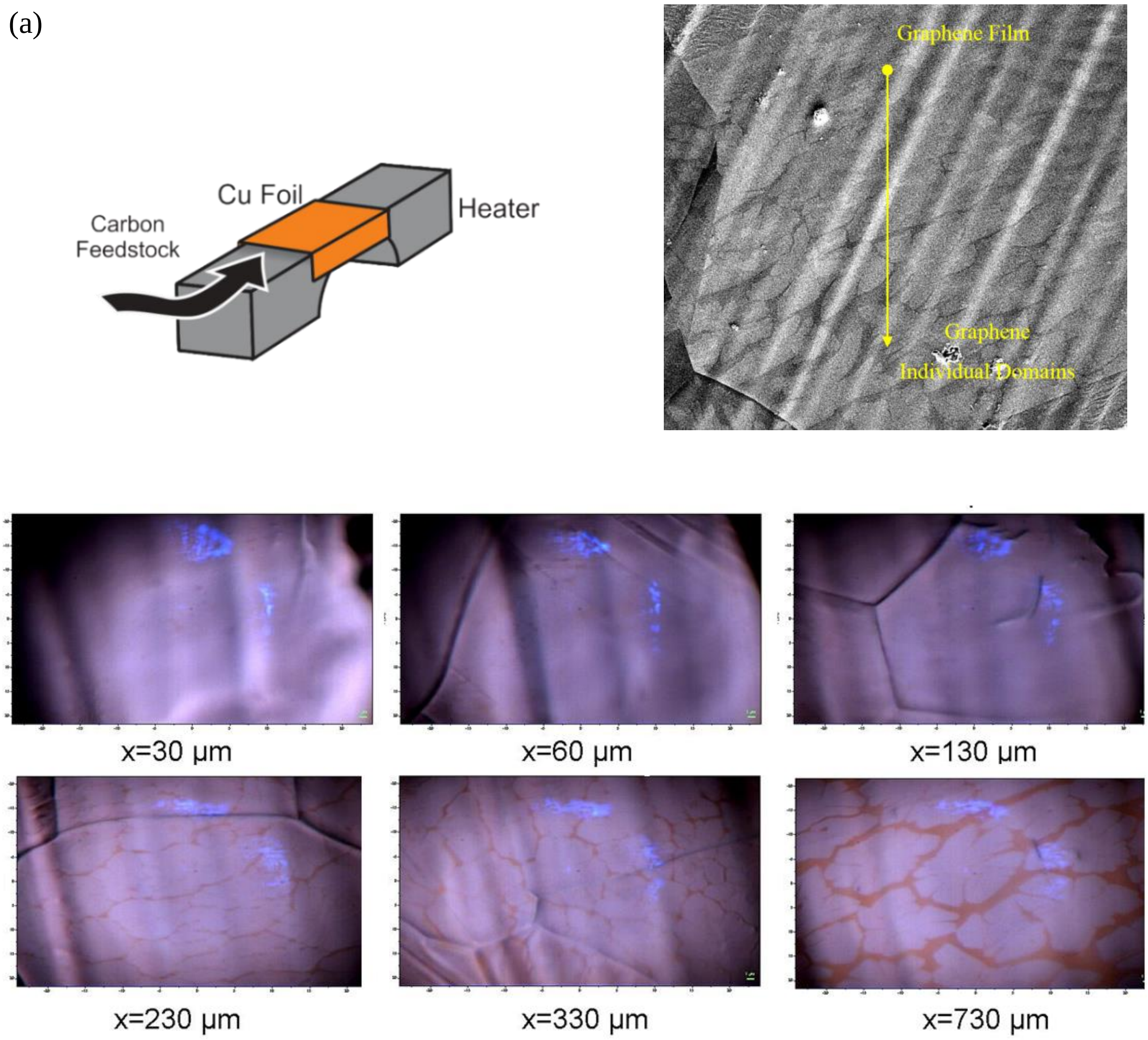

Figure 4-4 – (a) Sketch of the Cu substrate positioned over the graphite heater and typical SEM image of the backside of the substrate after the growth. (b) Optical images of the graphene grown along the backside of the copper foil. Graphene fully covers the copper at the edge of the sample (x=30 μm), whereas individual grains covers the middle of the foil (x=730 μm), where less carbon had access.

Raman spectroscopy was used to investigate the synthesized graphene. The Raman spectra were measured along a straight line crossing the sample, as depicted in Figure 4-4 (a). The position of the G peak shifts as the laser scans the sample from its edge to its center (Figure 4-5). The maximal shift occurs at the regions where individual grains are grown. The 2D peak shifts in a similar manner, but with higher magnitude, as seen Figure 4-6. For clarity, we subtracted the background due to Cu photoluminescence from the Raman spectra showed in Figure 4-5 and Figure 4-6.

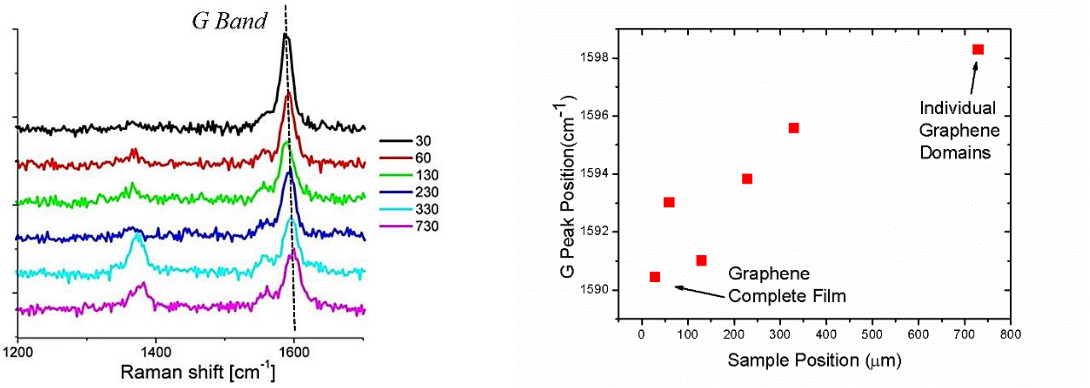

Figure 4-5 - Raman spectra in the D-G region taken at the same locations as the images shown in Figure 4-4. The G peak blue shifts about 10 cm^{-1} from the edge of the sample to middle where the individual grains can be seen on copper substrate. The sample position axis represent how far away from one of the edges the spectra was acquired. A D peak can be seen to appear in the region where the individual grains are grown. This is consequence of more graphene edges being probed.

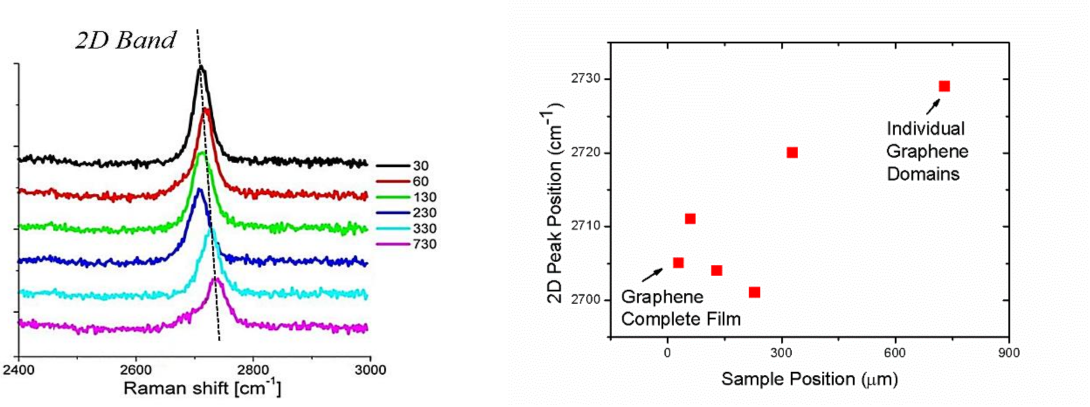

Figure 4-6 - Raman spectra in the 2D region taken at the same locations as the images shown in Figure 4-4 The 2D peak blue shifts about 30 cm^{-1} from the edge of the sample to the middle, where the individual grains can be seen on copper substrate.

According to references [80, 81], the G and 2D peaks shift due to strain and/or doping. In our case, we verified using scanning tunnelling spectroscopy (STS) that the doping level of the as-grown graphene is negligible. Therefore, the observed shifts of the G and 2D peaks of 9 cm^{-1} (Figure 4-5) and 28 cm^{-1} (Figure 4-5), respectively, indicate that our sample is strained rather than doped. This conclusion is corroborated by references [80, 81], which reported that the 2D peak is less affected by doping and more affected by changes in strain than the G peak.

Compressive biaxial strain usually leads to a phonon hardening (blue shift) for graphene, while tension leads to phonon softening (red shift). [98]. We verified a maximal blue-shift at the regions where individual graphene domains grew, thereby indicating that individual domains are more strained (compressive) than the fully covered graphene. We estimate the average strain induced on graphene from the Raman features using the mode Grüneisen parameter $\gamma = \Delta\omega/2\varepsilon\omega_0$, where ω_0 is the Raman mode frequency and $\Delta\omega$ is the shift in the mode frequency induced by biaxial strain ε. Using the Grüneisen parameters of γ_G = 1.8 [99] and adopting the peak positions of the G band as ${\omega_0}^G = 1584\ \mathrm{cm}^{-1}$ in the absence of strain, we found that individual graphene domains are under compressive strain of 0.3% whereas complete graphene films are 0.1% strained as depicted in Figure 4-7. These values are close to those presented in reference [99] where the authors predict frequency shifts in the range of 0-11.4 cm^{-1} for the G mode and 0-27.9 cm^{-1} for the 2D mode in the strain range of 0-0.4%

The origin of observed strain may lie in the graphene growth process itself. In fact, in section 4.2.2 we show that copper undergo substantial sublimation during the growth, which change the morphology of the substrate surface, leading to copper step retraction and copper faceting. This phenomenon often creates a rough surface underneath graphene, which may produce an appreciable strain over the graphene overlayer. Moreover, as graphene growth process occurs at high temperatures and ends with the graphene/metal system being cooled down to room temperature, it is plausible to expect that strain is also generated due the competition between copper contraction and graphene expansion that occurs during the cooling stage. This is consequence of the difference between the coefficients of thermal expansion for graphene (-6×10^{-6}/K) and copper (24×10^{-6}/K) [72].

The remaining question is, why graphene domains are more strained then complete films? To shed light on this issue, one must first consider the relation between graphene and the underneath substrate. In general, the graphene-metal interaction with the majority of transition metals is assumed to be small, approximately 100 meV per atom [100]. However, experimental findings support that the interaction between carbon and metal atoms at the graphene edges is much more strong, such that small graphene island tend to be dome shaped [101]. Therefore, the strong carbon-metal bonds at the graphene edge may play a key role in the induction of strain on the deposited graphene.

One simple interpretation for the fact that complete graphene film is less strained than individual graphene domains is that the coalescence of the individual domains, which lead to film formation, decouples the graphene edges from the substrate, enabling the film relax (at least partially). Individual graphene grains, on the other hand, have its edges more tightly bound to the substrate and, thus, are unable to expand in order to relax.

Currently, we are working to better understand these findings, and preparing a manuscript for publication.

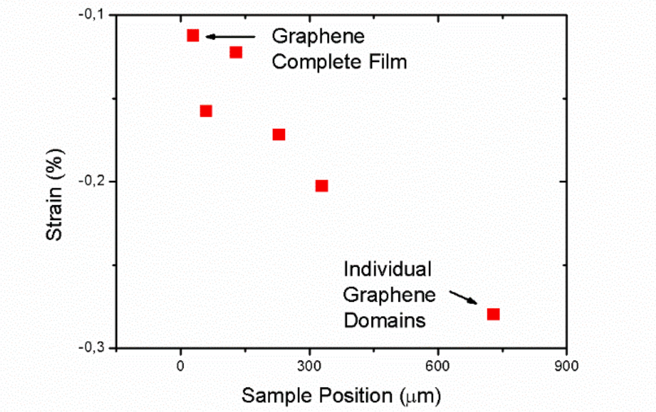

Figure 4-7 - Strain evolution over the sample shown in Figure 4-4.

4.1.3 Film Electrical Proprieties

In order to further characterize our grown material for future applications, we transfer it from the metal catalyst substrate to SiO_2/Si. The H_2 bubbling technique described in section 3.5.2 provides a shorter route to transfer graphene from the catalyst surface to the desired substrate than the substrate dissolution transfer procedure (section 3.5.1); however, we found that the later method produces fewer cracks and tears on the transferred graphene films. Optical microscopy and Raman spectroscopy characterizations suggest that the quality of monolayer graphene transferred by both methods is very good although some degree of p-doping was verified due the presence of residual PMMA resultant of the transfer process (this is evidenced by a shift on the G and 2D bands of Raman spectra). In Figure 4-8, it is shown optical images of a graphene film and individual graphene domains transferred to SiO_2/Si.

To investigate the electrical properties of the synthesized graphene, we fabricated the back-gated GFET shown in Figure 4-9 from the graphene monolayer film presented in Figure 4-8 (a).

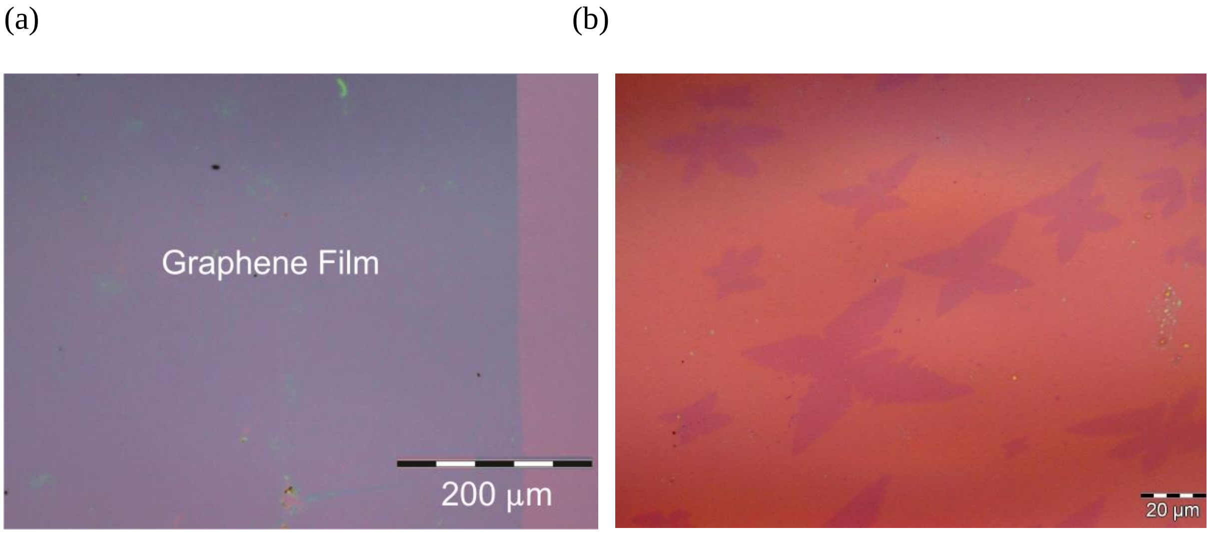

Figure 4-8 – (a) Graphene film and (b) graphene monocrystalline domains transferred to SiO_2/Si. The achievement of large graphene single domains as showed in (b) is discussed in details in section 4.2.

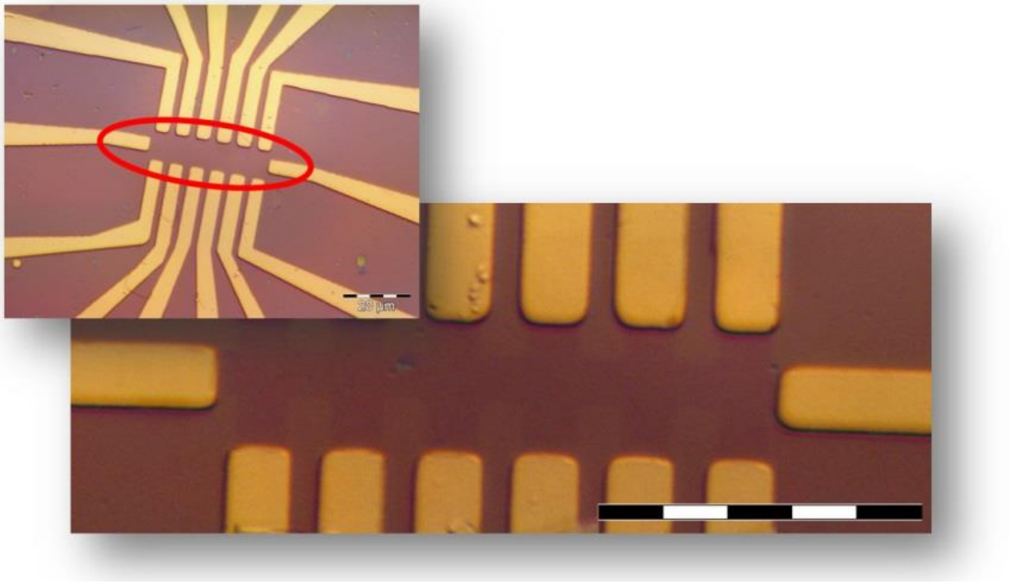

Figure 4-9 – Back-gated graphene field effect transistor (GFET). See section 3.6.2. for further details.

We utilized the circuit illustrated in Figure 4-10 to obtain the transconductance curve of the fabricated device. The current between the source and drain terminals is measured by a lock-in connected to a computer running a LabView application. This computer also control voltage difference applied between graphene and the p-doped Si substrate. This circuit is protected by a high resistance resistor with is placed in series with the substrate to prevent that over-currents originated by the dielectric rupture of the 300 nm silicon oxide damage the system.

The transconductance curve of the device shown in Figure 4-9 is presented in Figure 4-11.

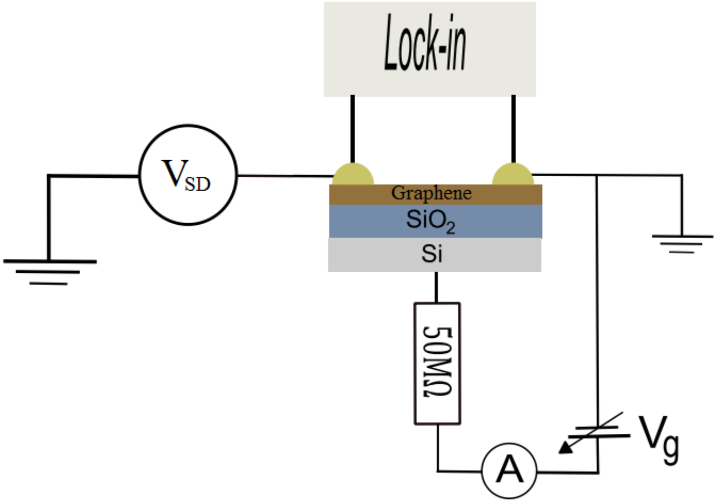

Figure 4-10 – Experimental setup for electrical measurements

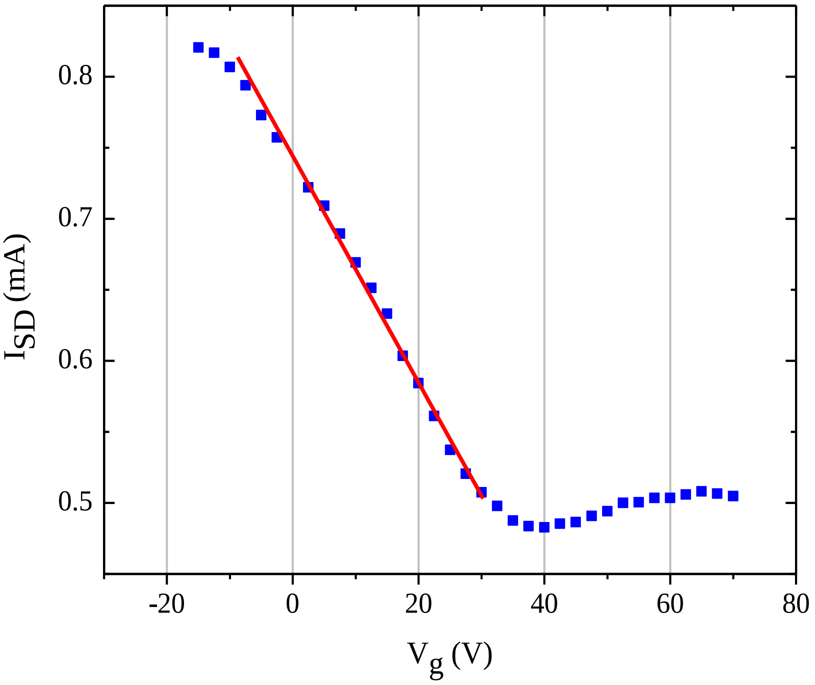

Figure 4-11 - Transconductance curve of the device shown in Figure 4-9.

The device shows typical characteristics of p-type doping, with the Dirac point located at positive gate voltage of about +40 V. It also displays electron-hole asymmetry, with suppression of the electron conduction branch. The p-type doping is attributed to residual PMMA from the transfer and photolithographic processes. The electron-hole asymmetry is likely originated from imbalanced carrier injection caused by “misalignment” between the contact electrode work function and channel neutrality point [102]. The hole transport branch switch from saturation at -20 V to current minimum at the Dirac Point (+40 V). The carrier mobility was estimated to be 1300 $cm^2/V \cdot s$ for holes at ambient conditions. Although this is not an extraordinary value, it is not bad since we still have much room to improve it. In fact, we found that adopting a PMMA solution with lower concentration gave fewer residues after exposure to acetone. It has yet to be verified how this improvement affect the graphene doping level and the charge carrier mobility. Besides, techniques such as the current annealing, wherein a current conducted through the graphene film was reported to remove contamination on the graphene surface by Joule heating [103], can also be employed.

4.2 Graphene Growth at Very Low Pressure

4.2.1 The Liquid Precursor

During a typical CVD process, the vacuum chamber must be clean in order to quickly reach the base pressure when pumped down. We noted, however, that over the long term the time necessary by the system to reach the desired pressure had increased. Moreover, we verified that graphene was growing even without the introduction of methane to the reactor. These observations impelled us to search for contaminates which could be acting as carbon sources during the growth. Typical contaminants of high vacuum systems include oil and grease on screws and seals, as well as condensed vapors adsorbed on the walls of the reactor. Therefore, we perform a meticulous cleaning procedure to ensure that the vacuum components were clean and grease-free. We found, however, that the contamination was eliminated only when the rotary vacuum pump (see section 3.1) was replaced by an oil-free diaphragm vacuum pump. This result (and other additional tests) led us to conclude that the source of contamination was the back streaming of oil vapors at the inlet of the rotary pump.

A remarkable aspect of this oil vapor back streaming (10^{-6} to 10^{-5} Torr) is that it could be used to grow large graphene single crystals, as depicted in Figure 4-12. In fact, using methane we were not able to achieve such large domains since the increase of growth temperature often demanded the increase of methane concentration, which generally led to the increase of nucleation density and the decrease of domains size. In contrast, the “oil vapor precursor” enabled the growth of low density of graphene domains at temperatures above 920ºC, up to temperatures close to the copper melting point (~980 ºC at 10^{-6} Torr).

This precursor is a vapor of a paraffinic oil, a petroleum derivative composed of a mixture of alkanes with the molecular formula C_nH2_{n+2} in the C_{20} to C_{50} range. The major benefit of the employment of high molecular weight liquid precursor compared to the widely used low molecular weight gaseous sources, such as methane and ethylene, is the possibility to synthesize graphene at lower temperatures and low precursor concentrations. This fact can be explained in terms of the competition between desorption and dehydrogenation processes, as discussed in section 2.3.2. In simple terms, larger molecules are more efficient to produce carbon active species because they have high desorption barriers that inhibit their easy desorption during the consecutive dehydrogenation steps. The same do not occur with small molecules such methane and ethylene which have a small desorption barrier compared to their dehydrogenation barrier. In this latter case, the growth only proceeds at much higher supersaturation, i.e. at much larger partial pressures.

Based on this serendipitous finding, we decided to further investigate the growth using this liquid precursor. Hence, graphene was grown exposing the surface of 25 μm-thick copper foils to a low pressure (10^{-5} Torr) of paraffinic oil vapor. No hydrogen or other gaseous species were employed during growth and it was found that no pretreatment of the substrate was required before the synthesis; even the usual thermal annealing was dispensed. This latter observation is justified by a recent study [104] that claims that copper with an oxidized surface act as a self-cleaning substrate for graphene growth. According to this work, the thermally decomposition of copper oxide releases oxygen, which reacts with the carbon residues on the copper surface and forms volatile compounds. The desorption of such compounds (e.g. carbon monoxide and carbon dioxide) leave a clean copper surface free of carbon.

The quality of the obtained graphene domains was very high as indicated by the Raman spectra shown in in Figure 4-12. As long as the laser spot is entirely focused inside the grain, without probing its edges, the D peak is significantly smaller than the G band. It can be comparable to the noise level, which indicates that few defects are present [77]. The 2D peak is up to 4 times more intense than the G band and with a FWHM down to ~28 cm^{-1}, further confirming the good quality of monolayer graphene.

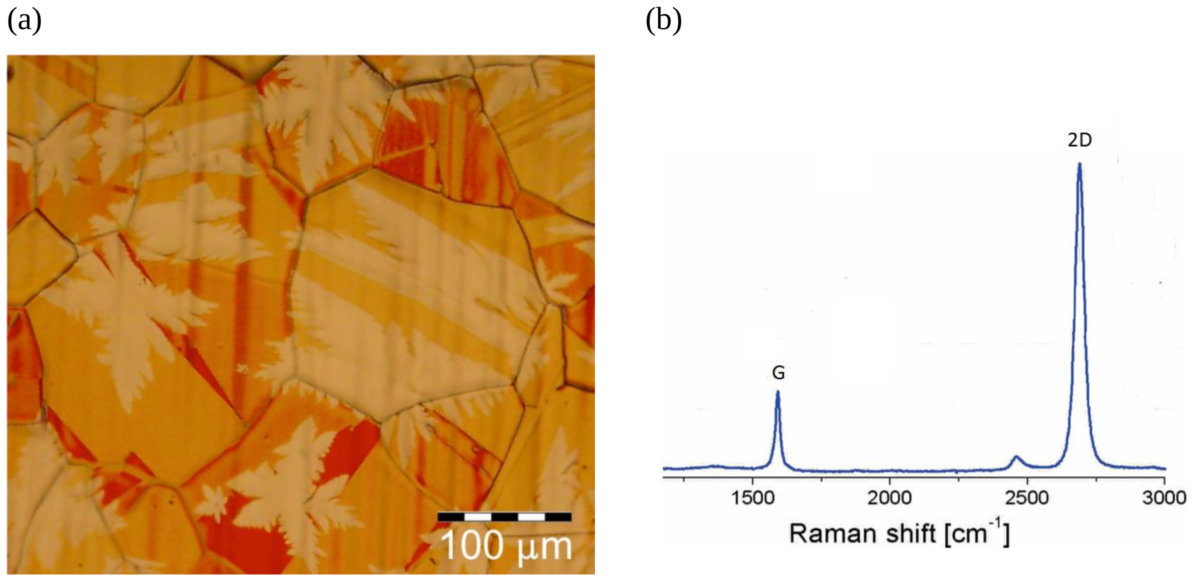

Figure 4-12- (a) Optical image of large graphene domains grown at low pressure and high temperature (960 ºC) using paraffinic oil; (b) Raman Spectra of a single graphene domain. For clarity, the strong background due to Cu photoluminescence was subtracted from the Raman spectra

We also observed that graphene domains having different shapes were grown on the many different grains that compose a Cu foil. Such trend is more evident at higher temperatures, close to the copper melting point (~ 980 ºC at 10^{-6} Torr). This evident relationship between the observed graphene morphologies and the underneath Cu grain is discussed in more details in the next section.

4.2.2 The impact of substrate surface self-diffusion in domain shape

This section is mostly based on the work published in ref. [105]. Here, we focus on the characterization of isolated graphene domains grown at different temperatures, obtained prior to the coalescence of a complete monolayer. We found that graphene domains often exhibit different morphologies at different Cu grains when grew at high temperatures. To determine the crystal structure of our underlying Cu foil substrates, we perform electron-backscatter diffraction (EBSD) measurements. These measurements give us crystallographic orientation in the x, y, and z directions, but here we will only consider the z plane of the copper surface. Figure 4-13 shows a typical orientation map of the different grains that compose a Cu foil. The EBSD map of this foil shows a crystallographically diverse Cu surface, composed of Cu(111), Cu(113), Cu(013), Cu(012), Cu(101), and Cu(001) facets.

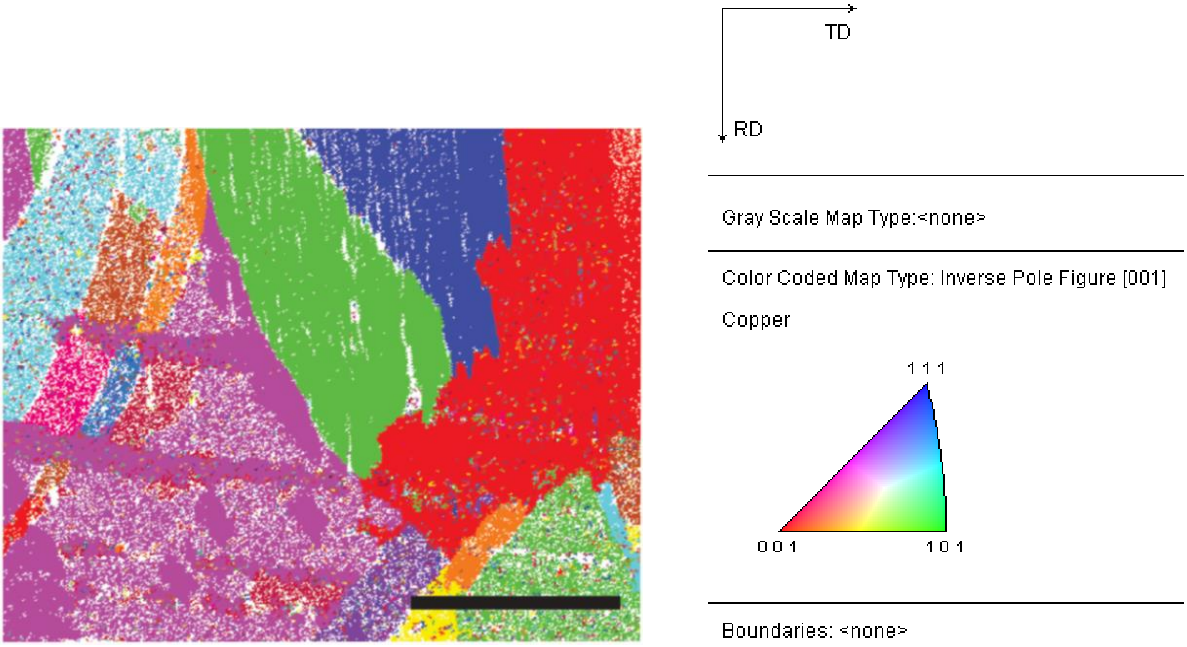

Figure 4-13 – EBSD map of a typical Cu foil used during graphene growth.

One can correlate the EBSD map with scanning electron microscope (SEM) imaging to assess graphene coverage visually. In this way, we verified that aligned six-folded graphene domains can be grown over the Cu(113) face as depicted in Figure 4-14.

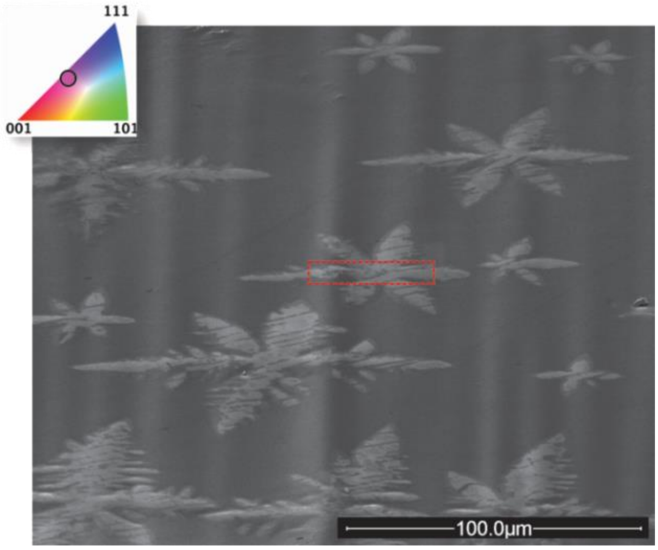

Figure 4-14 - SEM image and the corresponding EBSD data (inset) of graphene grown over as-receveid Cu foil on Cu(113) surface at 960 °C.

Graphene domains grown on polycrystalline Cu at 960 °C exhibit multi-branched dendritic edges as depicted in Figure 4-15. EBSD analysis revealed that four-lobed domains, having square and rectangle symmetries, are associated to Cu (001) and (101) surfaces, respectively; whereas six-lobed, star-shaped, domains are found on (111). The average domain growth rate (R), calculated based on analysis of optical images and deposition time, was very high, ~ 2-3 μm^2/s. Growth was faster, R= 3 μm^2/s, on atomically flat Cu surfaces [(001) and (111)] than on the stepped (101) surface, R= 2 μm^2/s (Figure 4-16.a). These results are in contrast to those reported in reference [106] where growth on Cu(111) was found to be faster than on Cu(001) but slower than growth on (101) and on high index surfaces. The referred results, however, were obtained from APCVD processes which generally display trends completely different from LPCVD processes. Relying only on our own results from LPCVD, we attributed the slower graphene growth rate on Cu (101) to the presence of monoatomic steps which can effectively increase the diffusion barrier felt by the diffusive adspecies in certain directions. [107].

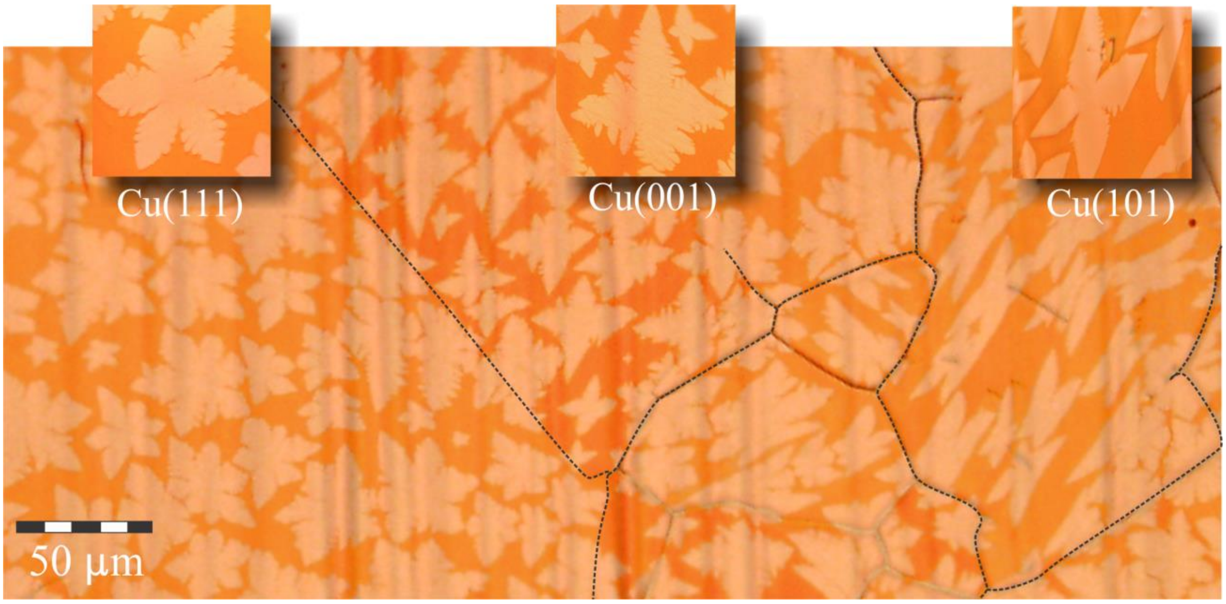

Figure 4-15 – (a) Optical images of graphene domains grown on as-received Cu foil. The growth temperature was 950 ºC and the precursor partial pressure 5 x 10^{-6} Torr.

Micro-Raman spectra of as-grown domains acquired at different Cu crystallographic surfaces shown similar characteristics: large 2D to G-peak intensity ratio of $I_{2D}/I_G \approx 3$ and a 2D peak width (FWHM) of 32 cm^{-1} (Figure 4-16.b). In addition, no significant shifts of the G and 2D bands were verified between the spectra of domains grown on different Cu faces, thereby indicating a weak coupling between graphene and Cu.

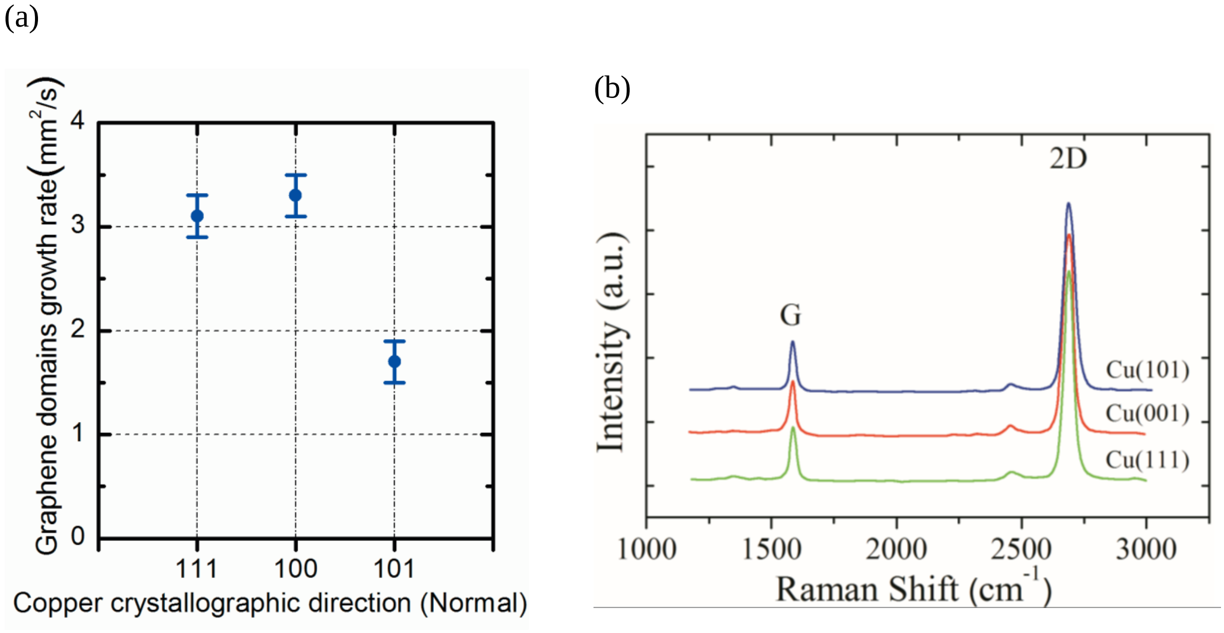

Figure 4-16 - (a) Average growth rates of graphene domains shown in Figure 4-15; (b) Raman spectra of graphene domains grown in different Cu faces. The fluorescence background signal due the Cu substrate was removed from the total spectra.

As can be seen in Figure 4-17, while the (111) and (001) facets of fcc Cu have a flat hexagonal and cubic atomic arrangement, with each atom having six and four in-plane nearest neighbours, respectively, the fcc (113) surfaces consist of parallel close-packed atom rows with a dilated hexagonal arrangement of the top most atoms. This structure is very similar to the (101) faces, however, in the case of the (113) surfaces, each second row is shifted along the close-packed direction by half an atomic diameter. As a consequence, the (113) surfaces contain both (111) and (001) microfacets, whereas (101) surfaces only comprise (111) microfacets. [108] These fundamental geometric differences are expected to have distinct surface energy potentials, which should affect the diffusion of any migrating adspecies.

We further observed that in the beginning of the growth, graphene islands have symmetrical circular shapes, which are independent of the orientation of the underneath copper substrate (Figure 4-18). As the island diameter increase, morphological instabilities develop and lobes start to propagate increasing the island perimeter-to-area ratio very rapidly.

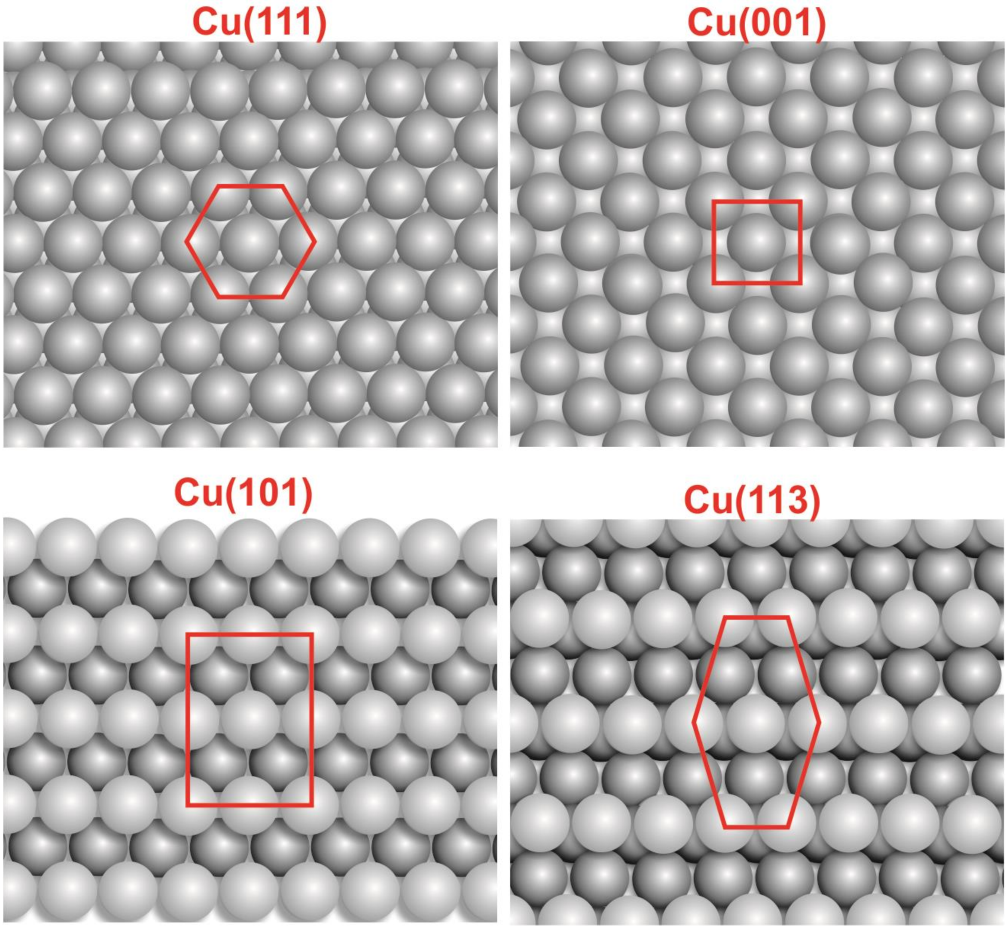

Figure 4-17 – Cu crystallographic surfaces

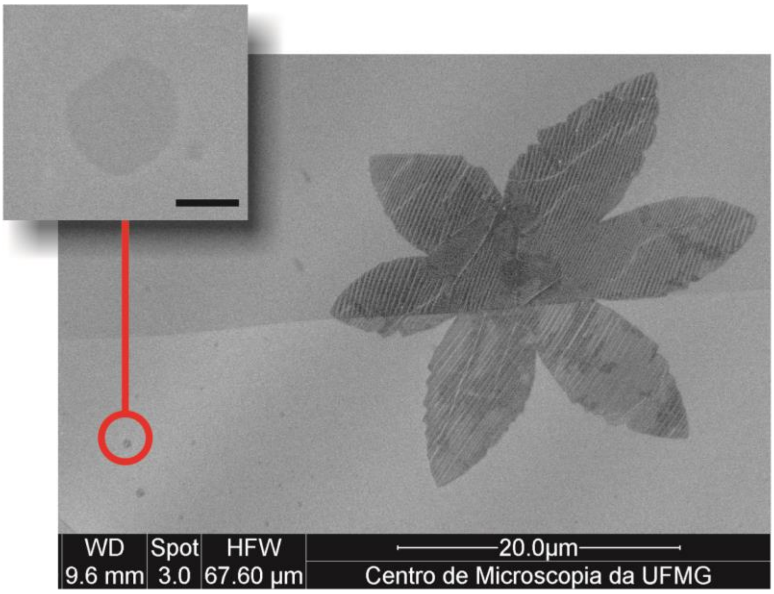

Figure 4-18 - SEM image of graphene domains at different stages (T = 950 ºC). Due to large deviations in nucleation time, various phases of growth can be observed in the same sample. The scale bar in the inset is 200 nm.

Graphene morphology is also strongly affected by deposition temperature, as shown in Figure 4-19. For T<900 ºC, round graphene domains grew uniformly across all grains of the polycrystalline substrate. As T increases, the island perimeter-to-area ratio also increases by the formation of dendrites which are oriented with respect to the Cu crystallographic directions. This effect is seen first on the stepped (101) and (113) faces for T~900 ºC, and then on (111) and (001) faces at T>920 ºC. In addition, we verified the formation of Cu hillocks underneath the graphene domains grown at higher T, indicating that a substantial amount of mass transport in the copper surface occurs during growth (Figure 4-20).

These results indicate that both temperature and substrate crystallography are important in order to control the graphene domain pattern during LPCVD. Similarly, the shape and size of the growing islands in kinetically controlled epitaxial growth of metals on metal surfaces are also dependent on the same parameters (temperature and symmetry) [109]. According to standard "atomistic" theory, growth is result of the competition between the different movements that adatoms can make along the surface, such as diffusion on surface terraces, over steps, along edges and across corners and kinks. Hence, one is tempted to apply established principles of epitaxial growth to explain graphene CVD on Cu [109, 110, 111]. Nonetheless, there are key incompatibilities between the existing models of epitaxial growth and graphene CVD on copper. First, in metal epitaxy, the growth mode is often determined by kinetic constraints wherein the growing aggregates can be shaped by selective activation/freezing of certain diffusion processes, depending on the temperature. The growth temperature, however, is usually much lower than the melting point (T_m) of either the substrate or the deposited material. This contrasts with our findings which show that the correlation between shape of graphene domains and the symmetry of the substrate becomes evident just at temperatures very close to the Cu melting point. Another sign of the complexity of the graphene growth compared to the typical epitaxy is the weakly interaction between graphene and most transitions metals. In the standard model of epitaxy, it is assumed that the adatoms and edge atoms are considerably more weakly bound than bulk atoms. Carbon adatoms and graphene edge atoms, on the other hand, often have carbon-metal bonds that are comparable in strength to the carbon-carbon bonds within graphene [112]. Therefore, carbon adatoms must break all their bonds with the substrate atoms in order to become part of the growing graphene crystal. Since, adatom-metal bonds are estimated to be very strong, up to 7-eV, [69],the barrier for attachment should be expected to be very large. This situation has no analogue in the standard epitaxial picture where an adatom only experiences a small energy barrier to attach to the edge of a growing island.

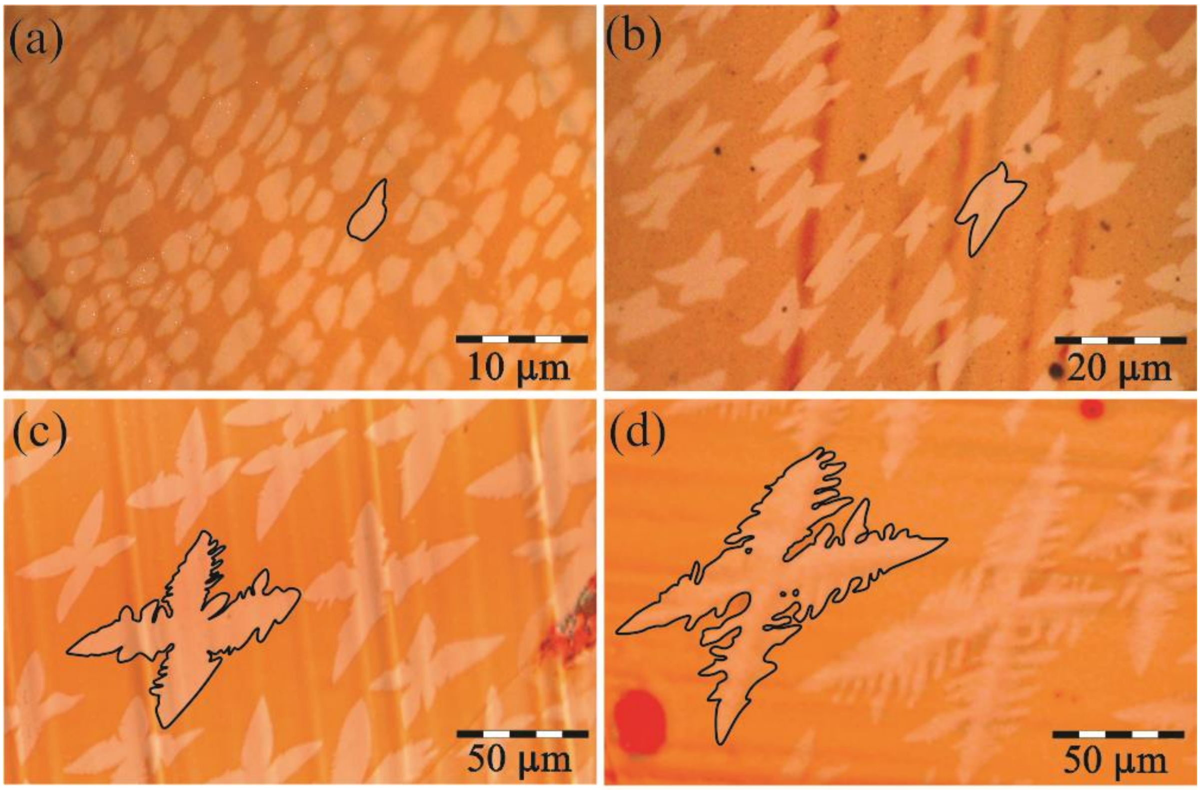

Figure 4-19 - Temperature dependence of graphene shape on Cu(101). The growth temperatures were (a) 920 ºC, (b) 940 ºC, (c) 960 ºC, and (d) 980 ºC.

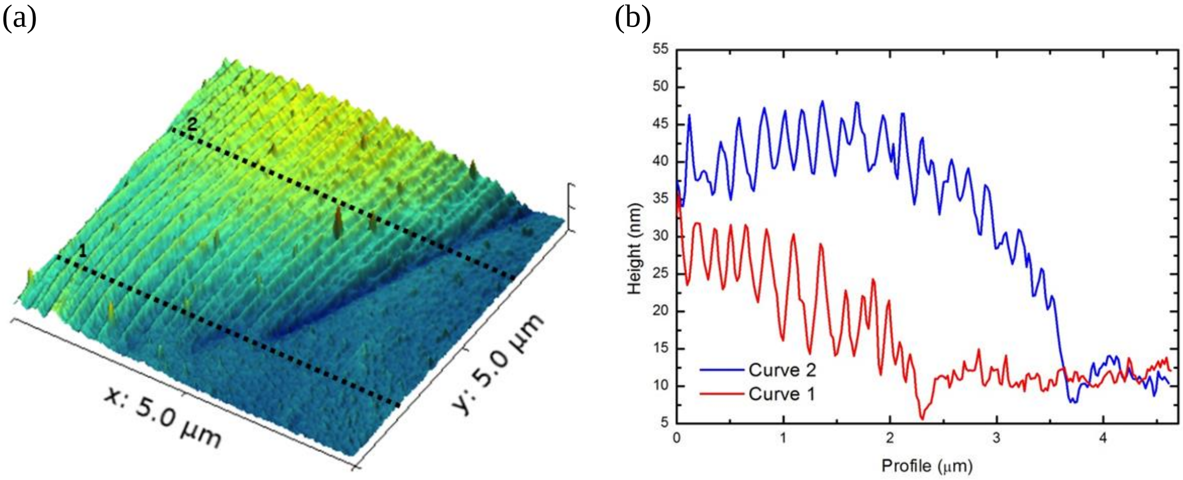

Figure 4-20 – (a) Formation of Cu hillocks at 980º C. (b) Topologic profile of the exposed Cu surface after graphene growth.

One way to assess graphene growth mechanisms is to investigate the T dependence of key growth characteristics, such as nucleation density (n_d). [37] Figure 4-21 depicts the T dependence of graphene n_d wherein two slopes can be identified, associated with different activation energies (E_{act}). For T > 960ºC (E_{act} = 9 eV), graphene domains exhibit multi-branched dendritic edges aligned according to the principal Cu crystallographic directions, as previously stated (Figure 4-19{c,d}). In this case, n_d can be very low (n_d~10^{-3} µm^{-2} for T = 980 ºC), which means that large graphene domains, having diameter up to 150 µm, could be obtained if the growth had proceeded. At lower temperatures (T < 960º C), on the other hand, the activation energy is lower (E_{act} ~ 6 eV), graphene domains are smaller and display smoother branch edges with some relative misalignment among them (Figure 4-19{a,b}).

In the framework of the existing nucleation models [113], the apparent nucleation activation energy is related to: (a) the energy barrier of attachment for the capture of a monomer by supercritical nucleus, E_{att}; (b) the activation energy of surface diffusion of a monomer, E_d; (c) the activation energy for dissociative adsorption of gas phase molecules on the substrate, E_{ad}; and to (d) the desorption energy of a carbon monomer on the substrate surface, E_{des}. For the sake of comparison, the experimentally measured activation energy of graphene nucleation reported in literature is in the interval of 3-4 eV at temperatures above $900℃$ [37, 114]. This discrepancy between our results and those from literature is not surprising since our growth was performed with a different carbon precursor, on a Cu foil which was not subject to thermal annealing, and under a total pressure almost 3 orders of magnitude smaller than the values of standard LPCVD graphene. It is more worthwhile to compare ours results with the temperature dependence of copper surface self-diffusion previously reported and compiled in ref. [115] and summarized in Figure 4-21(b). Gjostein and Bonzel [116] determined the self-diffusion coefficient in Cu (101) surfaces in a wide temperature range. For the temperature interval of $500 < T < 960℃$, they obtained an activation energy of 0.8 eV, whereas for higher temperatures (to the melting point), a significantly larger value, 2.7 eV, was obtained. Similar results were observed in other studies, suggesting that an additional mechanism appears to contribute significantly to Cu surface diffusion for $T > 960℃$. In fact, the same trend was reported for wide variety of metals by in numerous studies of mass-transfer diffusivity, compiled five decades ago [116, 117, 118, 119, 120, 121]. These studies show that the ratio between activation energies in high and low temperature regions is between 2 and 3, and that correspondingly the pre-exponential factor *D*, varies over about five orders of magnitudes.

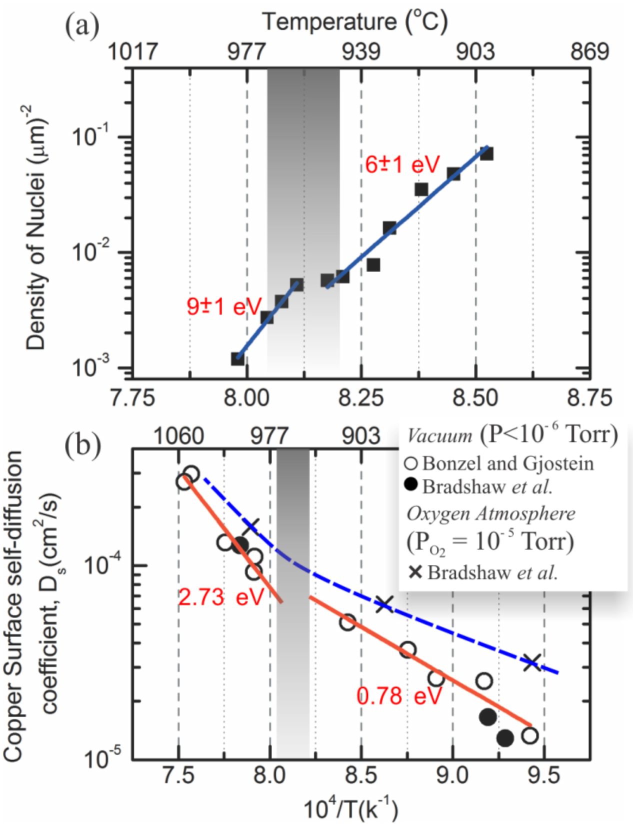

Figure 4-21 - Arrhenius plot of the temperature dependence of (a) density of graphene nuclei measured at the (101) Cu Surface, (b) temperature dependence of surface self-diffusion on Cu (101) surface. Reprinted from J. Phys. and Chem. Ref. Data 2, 643-655 (1973).

The change in the E_{act} of copper surface self-diffusion is not completely understood, and different interpretations have been put forth [122, 123]. However, a reasonable explanation for the peculiar bending of the Arrhenius plot shown in Figure 4-21(b) is related to a change from a regime where the key energy barrier to surface diffusion is the enthalpy of formation of adatoms from kinks sites in surface steps (lower T) to a regime wherein the release of an adatom directly from a flat surface becomes significant (higher T). [124] As more bonds have to be break to form an adatom from a flat surface than from a kink site, the energy barrier of adatom formation increases accordingly. Simulation of Cu (l01) using effective medium theory has demonstrated a substantial adatom formation above 0.7 T_{melt} [125]. This kind of adatom generation will be fundamental for the growth model proposed next (Figure 4-24). A remarkable similarity is observed when the two Arrhenius plots of Figure 4-21 are compared. The change in E_{act} of copper surface self-diffusion occurs at the same T (960 ºC) as the observed transition for graphene n_d. Moreover, the differences between the E_{act} values for high and low T ranges are also fairly close (3 eV for graphene n_d, and 2 eV for Cu diffusion). Besides, these values are comparable to the measured heat of sublimation (3.5 eV), and to the calculated binding energy of copper (2.3-3.5 eV). [126] In summary, at higher T (> 960 ºC), Cu surface atoms tend to become loosely-bound and more prone to diffuse and sublimate. Therefore, it is reasonable to assume that intense rearrangement of Cu adatoms in the substrate surface should play a crucial role in graphene nucleation and growth. This role is reflected in the parallels observed in the Arrhenius plots of Figure 4-21, however a complete analytical description of all temperature dependent mechanisms (and all associated energies) involved in this complex growth process is beyond the scope of this work.

Interestingly, previous measurements of Cu self-diffusion have also revealed that it strongly depends on the atmosphere in which it takes place (Figure 4-22), being larger in vacuum than in reducing atmospheres that are typical in graphene APCVD. [115, 121] Therefore, the hypothesis that Cu diffusion impacts graphene growth might also explain the differences observed between low and atmospheric pressure processes. Moreover, as shown in Figure 4-21 (b), the presence of O_2 also enhances Cu surface diffusion. Thus enhancement of Cu diffusion can also be invoked to explain (at least partially) recent results of Yufeng Hao *et al.*, [127] who found that oxygen accelerates graphene domain growth and shifts the growth kinetics from edge-attachment-limited to diffusion-limited (Figure 4-23).

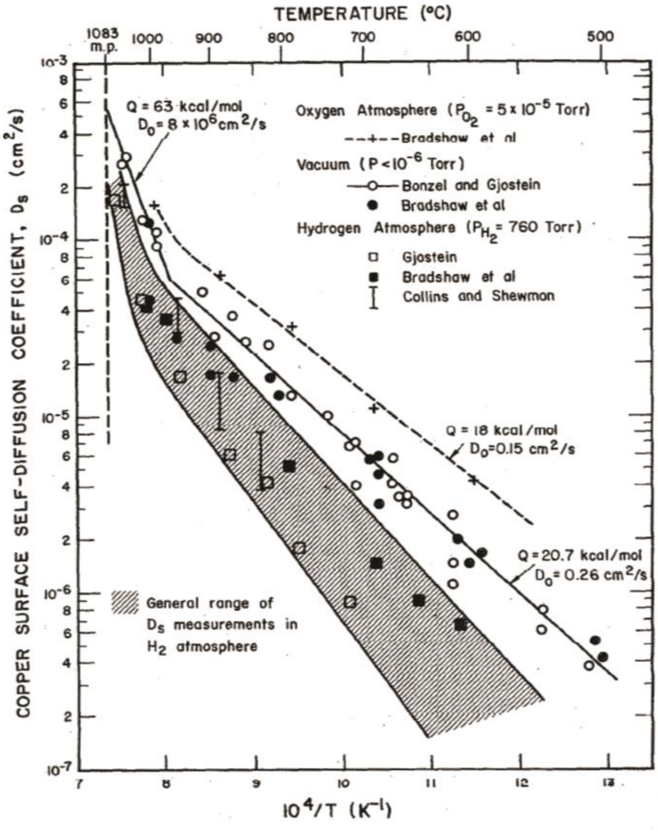

Figure 4-22 – Surface diffusion of copper on copper. Reproduced from [115].

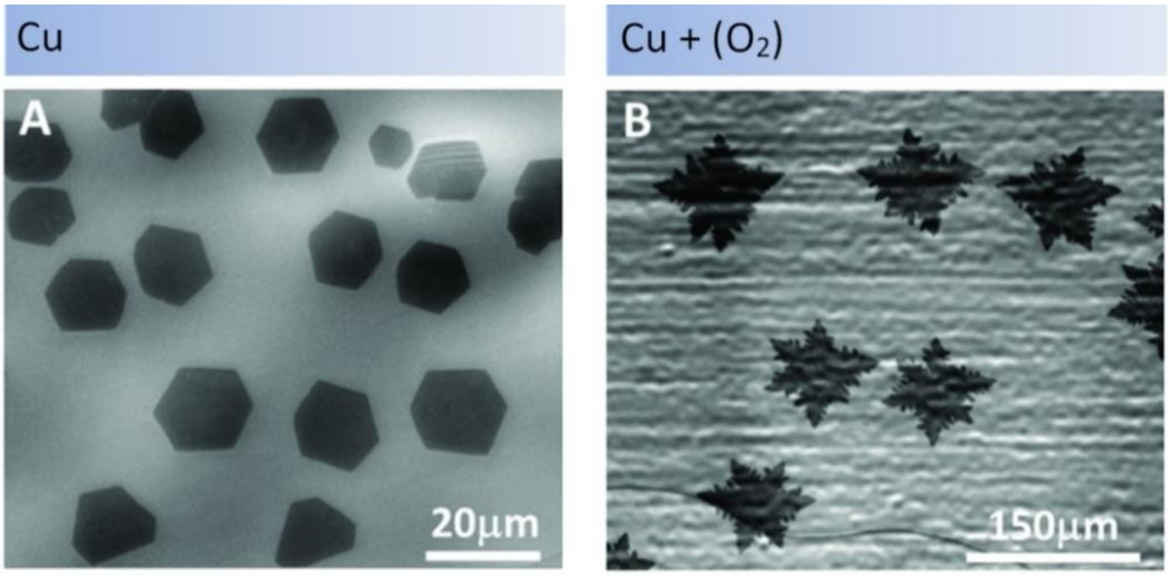

Figure 4-23 - The effect of oxygen on graphene growth kinetics. SEM images of graphene domains grown with and without the assistance of oxygen. Reproduced from [127].

High Cu sublimation and diffusion rates also explain the formation of Cu hillocks underneath the graphene domains at high T, by the mechanism known as step-bunching, which has been captured in a previous real time low energy electron microscopy study (Section 2.4.3.2). The movement of surface Cu atoms in non-flat surfaces occurs mainly via step flow induced by sublimation. When a step collides with a graphene island it slows down, and since additional steps are constantly arriving they accumulate underneath the island, forming a hillock.

We can now attempt to explain how graphene pattern formation occurs in low pressure, high temperature CVD processes, wherein Cu sublimation and diffusion are relevant. A schematic sketch containing the relevant steps is depicted in Figure 4-24. The nucleation stage has been described by H. Kim *et al* [37]; as growth begins, the concentration of carbon species on Cu surface quickly increases until a critical supersaturation is reached, after which stable nuclei are formed. At this point, the growth rate is high enough to produce isotropic round islands (Figure 4-18). However, as growth proceeds, the surrounding carbon adspecies are depleted and the growth front velocity decreases. As a consequence, sublimation induced Cu surface rearrangement becomes important. Cu atoms trapped in the region underneath graphene nuclei cannot diffuse out and sublimate, thus the surrounding substrate region is lowered leaving the graphene on the top of a relatively “elevated” Cu terrace (process 1 as indicated in Figure 4-24). This causes the increase of the barrier seems by carbon adspecies arriving at the graphene edges, reducing their attachment probability (process 2). In the meantime, since T is close to Cu T_m, a high fraction of Cu atoms from flat terraces have enough energy to detach and to diffuse as loosely-bound adatoms (process 3). When Cu adatoms reach the steps retained by the graphene domains, they are highly likely to be incorporated (process 4) due to the high T. In turn, the newly added Cu atoms act as pathways for incoming carbon adspecies, decreasing the energy barrier for carbon attachment; *i.e.*, only after the Cu terraces surrounding the graphene are extended, the diffusive carbon adspecies are able to attach to the graphene edges and contribute to growth (process 5).

The results discussed section 2.4.2 obtained from the growth of graphene on Ru (0001) can also be invoked to support our model. Gunther *et al.* verified from the analysis of in-situ STM images that at low T, graphene growth front is unconstrained by the atomic steps on the metal surface and it can eventually cover the entire surface. At lower pressures or higher T, however, graphene growth front no longer traverses the Ru atomic steps; instead, graphene can only continue to grow on the original Ru terrace level as a result of the terrace expansion. This latter mechanism is, according to our model, the main responsible for graphene pattern formation.

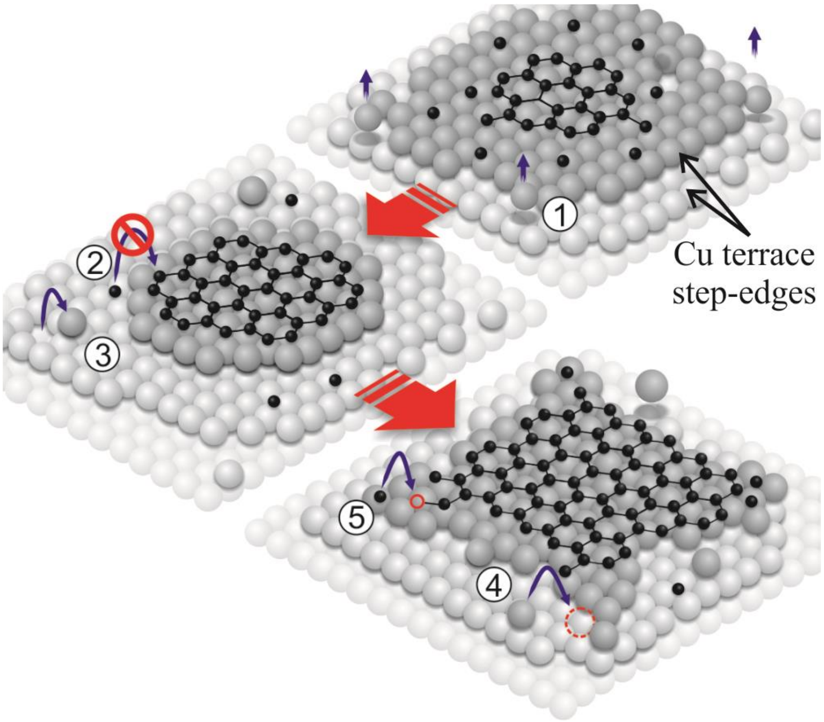

Figure 4-24 - Graphene pattern formation during LPCVD synthesis on Cu(001). Intense sublimation of Cu atoms at the surrounds of a growing island lowers the adjacent substrate region leaving graphene on the top of an "elevated" Cu terrace (process 1). This causes the increase of the barrier seems by carbon adspecies arriving at the domain edges, reducing their attachment probability (process 2). In the meantime, due to the high temperature, a high fraction of Cu atoms from flat terraces have enough energy to detach and to diffuse as loosely-bound adatoms (process 3). Diffusive Cu adatoms that impinge upon the steps retained by graphene domains can be incorporated extending the Cu terraces in accordance with the local Cu symmetry (process 4). The shape of the Cu terraces defines the most probable directions at which the incoming carbon adspecies can attach to the graphene edge (process 5).

An additional evidence to support our model is given in Figure 4-25 which presents an atomic force microscopy (AFM) image of graphene grown at 960 ºC on copper. The Cu steps are unambiguously covered by graphene, forming a plateau of ~25 nm height relative to the bare copper. Moreover, the regularly spaced wrinkles in graphene suggests that graphene on copper is not a real conformal coating with atomic accuracy, further proving the low affinity of carbon to copper. [24]

This model is able to explain the differences in shape for different growth temperatures observed in Figure 4-19. If T is low (and/or total pressure is high) than Cu sublimation and surface self-diffusion are relatively small and C adspecies kinetics dictates the growth, yielding domains with hexagonal or rounded shapes. On the other hand, if T is high (and/or total pressure is low) than sublimation and diffusion of Cu atoms occur at high rates, and graphene growth is determined by the shape evolution of the Cu terraces surrounding the graphene domains, which in turn is given by a balance between retraction (by sublimation) and expansion (by Cu diffusion from the terraces below).

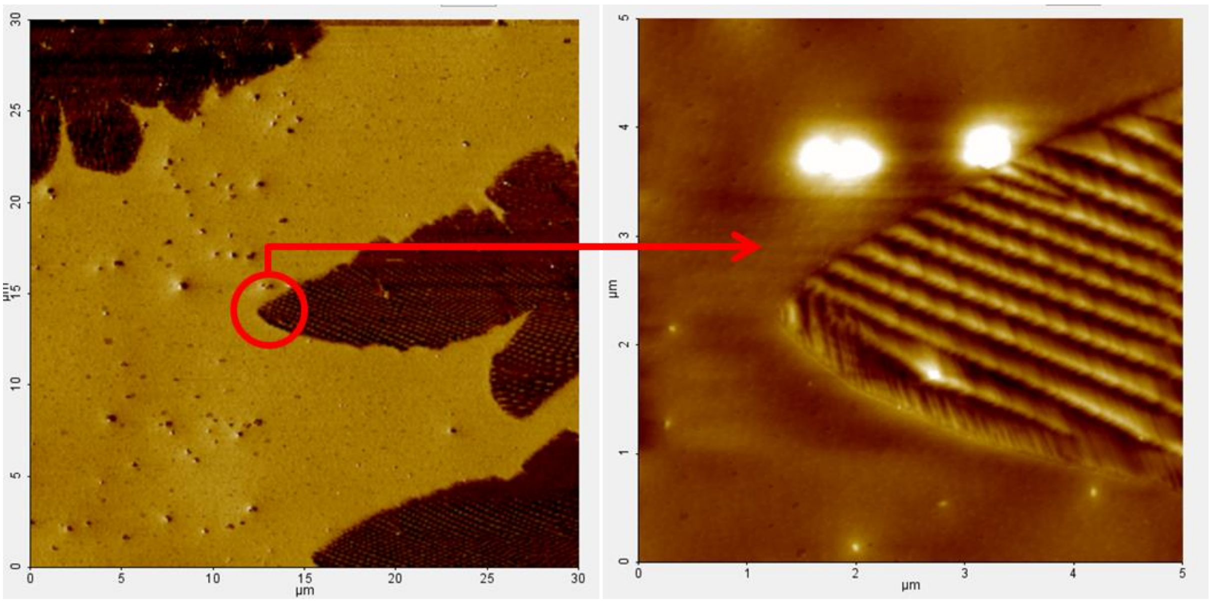

Figure 4-25 – AFM image of a graphene domain grown on Cu at 960 ºC and 5×10^{-6} Torr

In order to understand the process of expansion of the Cu terraces underneath graphene domains, we can resort to the theory of step motion in vicinal surfaces (section 2.2.2.2). The expansion occurs via step-edge attachment of Cu adatoms that diffuse along the immediately lower Cu terrace according to the stationary diffusion equation (eq. 2-18):

-

$$\frac{\partial c}{\partial t} = D_s \nabla^2 c + F - \frac{c}{\tau_s}$$

where D_s is the surface diffusion tensor, c is the concentration of mobile atoms adsorbed on the lower terrace, τ_s is the life time of an atom in a state of mobile adsorption (adatom) and F is a generation rate of adatoms. In the standard theory, F corresponds to the arrival rate. However, here F can be associated to the generation of adatoms directly from within the terrace (as described in the discussion of Figure 4-24).

Assuming that only Cu adatoms coming from the lower terrace contribute for the growth of the terrace retained by graphene, the diffusion mass flux arriving at the step is given by: [128]

$$D_s(\mathbf{n} \cdot \boldsymbol{\nabla} c) = K\left(c - c_{eq}{}^{*}\right) \qquad \text{eq. 4-1}$$

where n is the local step normal, $c_{eq}{}^{*}$ is the local equilibrium concentration which has a Arrhenius dependence with temperature. The kinetic coefficient, K, gives a measure of how ease adatoms coming from the lower terrace can stick to the growing edge, and it depends on the symmetry of the Cu face. As a result, terrace edges expand with an orientation-dependent velocity given by:

$$\mathrm{v}_n = \Omega\, K(\theta)\left[c - c_{eq}{}^{*}\right] \qquad \text{eq. 4-2}$$

where v_n is the flow velocity normal to the step, Ω is the area occupied by an Cu adatom, and K depends on θ, the local orientation of the step normal. (see Figure 4-26 for more details about the parameters given in the above eqs.)

This set of equations is very similar to those used by Meca *et al.* (section 2.2.2.2) to describe carbon adatom dynamics during graphene growth, which provided an excellent description of the effects of kinetic and diffusion anisotropy on the shape of graphene domains. However, here we are proposing that similar effects resulting from copper adatom dynamics are more important. According to our description, there are two causes for the observed variety of graphene domain morphology: the anisotropy in the diffusion of Cu adatoms (reflected in the tensor D_s), which depends on the Cu crystallographic orientation, and the anisotropy in the attachment probability of Cu adatoms at the terrace edges surrounding the graphene domain, which also follows the symmetry of the Cu surface.

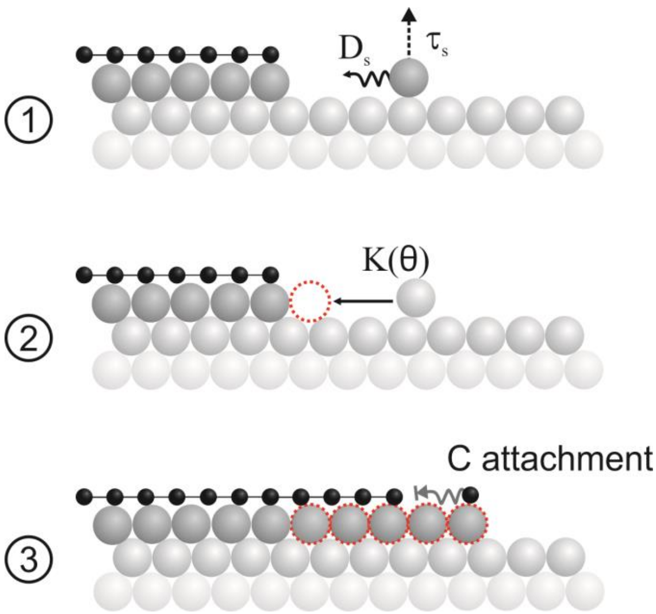

Figure 4-26 - Schematic view of the proposed growth model. D_s is the surface diffusion tensor, τ_s is the life time of an atom in a state of mobile adsorption, $\boldsymbol{K}$ is the kinectic coefficient which give a measure of how ease adatoms coming from the lower terrace can stick to the growing edge.

5 Conclusion

In this work we designed and built a cold-wall reactor to grown graphene by chemical vapor deposition under high vacuum conditions. We have found using standard graphene growth routine that the size of graphene single domains, and consequently the film quality, is strongly dependent on the growth temperature. The Raman spectra of graphene films grown at different temperatures indicated that high quality graphene with fewer defects form at higher growth temperatures. Moreover, we verified that during the coalescence of the graphene individual domains strain is induced over the film. A compressive strain of ~0.4 % is found for the fully covered graphene relative to the individual domains.

We also demonstrated the growth of large graphene single crystals (up to 300 µm) by exposing low purity copper foils to a vapor of a high molecular weight liquid carbon precursor. It was found that the conventional thermal pre-treatment of the substrate could be skipped without prejudice of the quality of the graphene to be grown. Actually, the quality of the resultant graphene was found to be very high, much better than the quality of our preceding growths preformed using the standard routine. In addition, we verified that graphene domains shapes were strongly dependent on the substrate crystallography and growth temperature. Based on these observations and on results reported by innumerous studies of mass-transfer diffusivity on metals, we proposed a mechanism to explain graphene formation at high temperatures and low pressures by considering the growth on a dynamic substrate surface. At temperatures near 1000º C and pressures of order 10^{-6} Torr, we do not expect to find an imaginary static surface wherein graphene can grow according to the standard picture of epitaxial growth. Instead we demonstrated a promising mechanism to engineering high quality monolayer films by controlling the dynamic of the substrate underneath. This approach should inspire one to look for an alternative route to grow graphene by using auxiliary gases which are capable of alter the substrate surface dynamics without change graphene elementary proprieties. Halogens, for example, are especially actives in promoting high Cu surface self-diffusion [129], and thus it remains to be seen how they affect graphene itself. These results were published in Applied Physics Letters, volume 105, issue 7, 073104 (2014).

Finally, we show two approaches to transfer the as-grown graphene to other substrates, and we measured the electrical proprieties of a graphene film transferred to Si/SiO_2. We expect to improve the quality of the transfer routine as well as the photolithographic process in order to begin the study of solar cells based on own graphene films.

6 Bibliography

1 K. S. Novoselov, A. K. Geim, S. V. Morozov, D. Jiang, Y. Zhang, S. V. Dubonos, I. V. Grigorieva, A. A. Firsov. Electric Field Effect in Atomically Thin Carbon Films. Science, 306 (2004), 666-669.

2 L. D. Landau. Zur Theorie der phasenumwandlungen II. Phys. Z. Sowjetunion, 11 (1937), 26-35.

3 R. E. Peierls, Quelques propriétés typiques des corps solides. Ann. I. H. Poincare, 5 (1935), 177-222.

4 K.I. Bolotina, K.J. Sikes, Z. Jiang, M. Klima, G. Fudenberg, J. Hone, P. Kim, H.L. Stormer. Ultrahigh electron mobility in suspended graphene. Solid State Communications, 146 (2008), 351–355.

5 C. Lee, X. Wei, J. W. Kysar, J. Hone. Measurement Of The Elastic Properties And Intrinsic Strength Of Monolayer Graphene. Science, 321 (2008), 385-388.

6 S. Ghosh, I. Calizo, D. Teweldebrhan, E. P. Pokatilov, D. L. Nika, A. A. Balandin, W. Bao, F. Miao and C. N. Lau. Extremely high thermal conductivity of graphene: Prospects for thermal management applications in nanoelectronic circuits. Appl. Phys. Lett., 92 (2008), 151911.

7 R. R. Nair, P. Blake, A. N. Grigorenko, K. S. Novoselov, T. J. Booth, T. Stauber, N. M. R. Peres, A. K. Geim. Fine Structure Constant Defines Visual Transparency of Graphene. Science, 320 (2008), 1308.

8 K. S. Novoselov, V. I. Fal′ko, L. Colombo, P. R. Gellert, M. G. Schwab & K. Kim. A Roadmap for Graphene. Nature, 490 (2012), 192–200.

9 X. Li, W. Cai, J. An, S. Kim, J. Nah, D. Yang, R. Piner, A. Velamakanni, I. Jung, E. Tutuc, et. al. Large-Area Synthesis Of High-Quality And Uniform Graphene Films On Copper Foils. Science, 324, 5932 (2009), 1312-4.

10 S. Bae; H. Kim, Y. Lee, X. Xu, J. Park, Y. Zheng, J. Balakrishnan, T. Lei, H. Kim, Y. Song et al. Roll-to-roll production of 30-in. graphene films for transparent electrodes. Nature Nanotech., 5 (2010), 574–578.

11 Dmitry A. Abanin and Leonid S. Levitov. Conformal Invariance And Shape-Dependent Conductance Of Graphene Samples. Phys. Rev. B, 78, 3 (2008), 035416.

12 Qingkai yu, L. Jauregui, Wei Wu, Robert Colby, Jifa Tian, Zhihua Su, Helin Cao, Zhihong Liu, Deepak Pandey, Dongguang Wei, Ting Fung Chung, Peng Peng, Nathan P. Guisinger, Eric A. Stach, Jiming Bao, Shin-Shem Pei & Yong P. Chen. Control and characterization of individual grains and grain boundaries in graphene grown by chemical vapour deposition. Nature Mater, 10 (2011), 443–449.

13 Z. Luo, S. Kim, N. Kawamoto, A. M. Rappe, A. Johnson. Growth mechanism of hexagonal-shape graphene flakes with zigzag edges. ACS Nano, 5, 11 (2011), 9154-60.

14 Yi Zhang, Luyao Zhang, Pyojae Kim, Mingyuan Ge, Zhen li, and Chongwu Zhou. Vapor trapping growth of single-crystalline graphene flowers: synthesis, morphology, and electronic properties. Nano Lett., 12, 6 (2012), 2810-6.

15 X. Li, C. Magnuson, A. Venugopal, J. An, J. Suk, B. Han, M. Borysiak, W. Cai, A. Velamakanni, Y. Zhu, L. Fu, E. Vogel, E. Voelkl, L. Colombo, R. Ruoff. Graphene films with large domain size by a two-step chemical vapor deposition process. Nano Lett., 10, 11 (2010), 4328-34.

16 Robert M. Jacobberger and Michael S. Arnold. Graphene Growth Dynamics on Epitaxial Copper Thin Films. Chem. Mater, 25, 6 (2013), 871–877.

17 Joshua d. Wood, Scott W. Schmucker, Austin S. Lyons, Eric Pop and Joseph W. Lyding. Effects of Polycrystalline Cu Substrate on Graphene Growth by Chemical Vapor Deposition. Nano Lett., 11, 11 (2011), 4547–4554.

18 Adrian T. Murdock, Antal Koos, Ben Britton, Lothar Houben, Tim Batten, Tong Zhang, Angus J. Wilkinson, Rafal E. Dunin-borkowski, Christina E. Lekka, and Nicole Grobert. Controlling the Orientation, Edge Geometry, and Thickness of Chemical Vapor Deposition Graphene. ACSNano, 7, 2 (2013), 1351–1359.

19 Hyeon-Jin Shin, Seon-Mi Yoon, Won Mook Choi, Seongjun Park, Dongwook Lee et al. Influence of Cu crystallographic orientation on electron transport in graphene. Appl. Phys. Lett., 102 (2013), 163102.

20 J. Wofford, S. Nie, K. Mccarty, N. Bartelt and O. Dubon. Graphene Islands on Cu Foils: The Interplay between Shape, Orientation, and Defects. Nano Lett, 10 (2010), 4890.

21 Lili Fan, Jie Zou, Zhen Li, Xiao Li, Kunlin Wang, Jinquan Wei, Minlin Zhong, Dehai Wu, Zhiping Xu, And Hongwei Zhu. Topology evolution of graphene in chemical vapor deposition, a combined theoretical/experimental approach toward shape control of graphene domains. Nanotechnology, 23 (2012), 115605.

22 Esteban Meca, John Lowengrub, Hokwon Kim, Cecilia Mattevi, and Vivek B. Shenoy. Epitaxial Graphene Growth and Shape Dynamics on Copper: Phase-Field Modeling and Experiments. Nano Lett., 13, 11 (2013), 5692–5697.

23 Antonio H. Castro Neto. Les Houches Notes on Graphene. arXiv:1004.3682 (2010).

24 U.O.Liverpool.[Online].Available:http://www.chemtube3d.com/orbitals ethene.htm

25 Jean-Noel Fuchs and Mark Oliver Goerbig. Introduction to the Physical Properties of Graphene. 2008.

26 A. H. Castro Neto, F. Guinea, N. M. R. Peres, K. S. Novoselov, and A. K. Geim. The electronic properties of graphene. Rev. Mod. Phys. 81, 109 (2009), 81 (2009), 109.

27 Jie Song, Fong-Yu Kam, Rui-Qi Png, Wei-Ling Seah, Jing-Mei Zhuo, Geok-Kieng Lim, Peter K. H. Ho & Lay-Lay Chua. A general Method for Transferring Graphene onto Soft Surfaces. Nature Nanotech., 8 (2013), 356–362.

28 Sreekar Bhaviripudi, Xiaoting Jia, Mildred S. Dresselhaus, and Jing Kong. Role of Kinetic Factors in Chemical Vapor Deposition Synthesis of Uniform Large Area Graphene Using Copper Catalyst. Nano Lett., 10, 10 (2010), 4128–4133.

29 Roberto Muñoz and Cristina Gómez-Aleixandre. Review of CVD Synthesis of Graphene. Chemical Vapor Deposition, 19, 10-11-12 (2013), 297–322.

30 K. F. Jensen and W. Kern. Thin Film Processes II. Academic Press, New York, 1991.

31 James D. Plummer, Michael Deal, Peter D. Griffin. Silicon VLSI Technology: Fundamentals, Practice, and Modeling. NJ: Prentice Hall, Upper Saddle River, 2000.

32 W. Kossel. Zur Theorie des Kristallwachstums. Nachr. Ges. Wiss. Goettingen Math. Phys, K1 11A (1927), 135-143.

33 M. Volmer. Die Kinetik der Phasenbildung. Steinkopff, Dresden, 1939.

34 I. N. Stranski. Zur Theorie der Kristallwachstums. Z. Phys. Chem., 136 (1928), 259–277.

35 J. W. Gibbs. "Collected Works". Longmans, Green and Co., New York, 1928.

36 G. Wulff. On The Question Of The Rate Of Growth And Dissolution Of Crystal Surfaces. Kristallogr. Mineral., 34 (1901), 449–530.

37 Hokwon Kim, Cecilia Mattevi, M. Reyes Calvo, Jenny C. Oberg, Luca Artiglia, Stefano Agnoli, Cyrus F. Hirjibehedin, Manish Chhowalla, And

Eduardo Saiz. Activation Energy Paths for Graphene Nucleation and Growth on Cu. ACS Nano, 6, 4 (2012), 3614–23.

38 Y. Liu, A. Dobrinsky and B. Yakobson. Graphene edge from armchair to zigzag: the origins of nanotube chirality? Phys. Rev. Lett., 105 (2010), 235502.

39 H. Lüth. Surfaces and Interfaces of Solid. Springer, 1993.

40 Cyriac Joseph. Growth and characterization of mixed rare earth oxalate crystals. Mahatma Gandhi University, 2010.

41 W.K. Burton, N. Cabrera, F.C. Frank. The growth of crystals and the equilibrium structure of their surfaces. In Ser. A 243 (1951), 299-358.

42 Olivier Pierre-Louis. Dynamics Of Crystal Steps. Comptes Rendus Physique, 6, 1 (2005), 11-21.

43 Chaouqi Misbah, Olivier Pierre-Louis, Yukio Saito. Crystal surfaces in and out of equilibrium: A modern view. Reviews Of Modern Physics, 82 (2010), 981.

44 Paul N. Patrone, T.L. Einstein, Dionisios Margetis. From atoms to steps: The microscopic origins of crystal evolution. Surface Science , 625 (2014), 37-43.

45 Hyeong-Chai Jeong, Ellen D. Williams. Steps on surfaces: experiment and theory. Surface Science Reports, Volume 34 (1999), 175-294.

46 J. A. Venables, G. D. T. Spiller And M. Hanbucken. Nucleation and growth of thin films. Rep. Prog. Phys., 47 (1984), 399-459.

47 Andrew Zangwill and Dimitri D. Vvedensky. Novel Growth Mechanism of Epitaxial Graphene on Metals. Nano Lett. (2011), 2092–2095.

48 Elena Loginova, Norman C. Bartelt, Peter J. Feibelman and Kevin F. McCarty. Evidence for graphene growth by C cluster attachment. New J. Phys., 10 (2008), 093026.

49 H. Amara, C. Bichara, and F. Ducastelle. Formation of carbon nanostructures on nickel surfaces: A tight-binding grand canonical Monte Carlo study. Phys. Rev. B, 73 (2006), 113404.

50 B. Wang, X. Ma, M. Caffio, R. Schaub and W.-X. Li. Size-selective carbon nanoclusters as precursors to the growth of epitaxial graphene. Nano Lett., 11 (2011), 424–430.

51 P. Lenzsolomun, M. C. Wu, W. Goodman. Methane coupling at low temperatures on Ru(0001) and Ru(11¯20) catalysts. Catal. Lett., 25, 1-2 (1994), 75-86.

52 A. Reina, X. Jia, J. Ho, D. Nezich, H. Son, V. Bulovic, M. S. Dresselhaus, J. Kong. Large Area, Few-Layer Graphene Films on Arbitrary Substrates by Chemical Vapor Deposition. Nano Lett., 9, 1 (2009), 30-35.

53 M. Losurdo, M. M. Giangregorio, P. Capezzuto, G. Bruno. Graphene CVD growth on copper and nickel: role of hydrogen in kinetics and structure. Phys Chem Chem Phys, 14;13, 46 (2011), 20836-43.

54 W. Zhang, P. Wu, Z. Li, J. Yang. First-Principles Thermodynamics of Graphene Growth on Cu Surfaces. J. Phys. Chem. C, 115 (2011), 17782-17787.

55 H. Chen, W. Zhu, Z. Zhang. Contrasting behavior of carbon nucleation in the initial stages of graphene epitaxial growth on stepped metal surfaces. Phys. Rev. Lett, 104, 18 (2010), 186101.

56 G. Henkelman, A. Arnaldsson, H. Jónsson. Theoretical calculations of CH_4 and H_2 associative desorption from Ni(111): Could subsurface hydrogen play an important role? J. Chem. Phys., 124 (2006), 044706.

57 Chak-Tong Au, Ching-Fai Ng, Meng-Sheng Liao. Methane Dissociation and Syngas Formation on Ru, Os, Rh, Ir, Pd, Pt, Cu, Ag, and Au: A Theoretical Study. J. Catal., 185, 1 (1999), 12-22.

58 N. R. Avery. Adsorption And Reactivity Of Acetylene On A Copper(110) Surface. J. Am. Chem. Soc., 107 (1985), 6711–6712.

59 S. Riikonen, A. V. Krasheninnikov, L. Halonen, R. M. Nieminen. The Role of Stable and Mobile Carbon Adspecies in Copper-Promoted Graphene Growth. J. Phys. Chem. C., 116 (2012), 5802.

60 P. Wu, W. Zhang, Z. Li, J. Yang, J. G. Hou. Coalescence Of Carbon Atoms On Cu (111) Surface: Emergence Of A Stable Bridging-Metal Structure Motif. J. Chem. Phys., 133 (2010), 071101.

61 Qinghong Yuan, Junfeng Gao, Haibo Shu, Jijun Zhao, Xiaoshuang Chen and Feng Ding. Magic Carbon Clusters in the Chemical Vapor Deposition Growth of Graphene. J. Am. Chem. Soc., 134, 6 (2012), 2970–2975.

62 J. Gao, J. Zhao, F. Ding. Transition metal surface passivation induced graphene edge reconstruction. J Am Chem Soc., 134, 14 (2012), 6204-9.

63 Abdeladim Guermoune, Tarun Chari, Filip Popescu, Shadi S. Sabri, Jonathan Guillemette, Helgi s. Skulason, Thomas Szkopek, Mohamed Siaj. Chemical vapor deposition synthesis of graphene on copper. Carbon, 49 (2011), 4204–4210.

64 X. Dong, P. Wang, W. Fang, C-Y Su, Y-H Chen, L-J Li, et al. Growth of large-sized graphene thin-films by liquid precursor-based chemical vapor deposition under atmospheric pressure. Carbon, 49, 11 (2011), 3672-8.

65 Tianru Wu, Guqiao Ding, Honglie Shen, Haomin Wang, Lei Sun, Da Jiang, Xiaoming Xie, Mianheng Jiang. Triggering the Continuous Growth of Graphene Toward Millimeter-Sized Grains. Advanced Functional Materials, 23, 2 (2013), 198–203.

66 Zhancheng Li, Ping Wu, Chenxi Wang, Xiaodong Fan, Wenhua Zhang, Xiaofang Zhai, Changgan Zeng, Zhenyu Li, Jinlong Yang, Jianguo Hou. Low-temperature growth of graphene by chemical vapor deposition using solid and liquid carbon sources. ACS Nano, 5, 4 (2011), 3385-90.

67 Jin-Ho Choi, Zhancheng Li, Ping Cui, Xiaodong Fan, Hui Zhang, Changgan Zeng, Zhenyu Zhang. Drastic reduction in the growth temperature

of graphene on copper via enhanced London dispersion force. Scientific Reports, 3 (2012).

68 Q. K. Yu, J. Lian, S. Siriponglert, H. Li, Y. P. Chen and S. S. Pei. Graphene Segregated on Ni Surfaces and Transferred to Insulators. Appl. Phys. Lett., 93 (2008), 113103.

69 E. Loginova, N. C. Bartelt, P. J. Feibelman, K. F. McCarty. Factors influencing graphene growth on metal surfaces. New J. Phys., 11 (2009), 063046.

70 S. Y. Kwon, C. V. Ciobanu, V. Petrova, V. B. Shenoy, J. Bareño, Gambin V, Petrov I, Kodambaka S. Growth of semiconducting graphene on palladium. Nano Lett., 9, 12 (2009), 3985-90.

71 L. Gao, W. Ren, H. Xu, L. Jin, Z. Wang, T. Ma, L.-P. Zhiyong Zhang, Q. Fu, L.-M. Peng, X. Bao, H.-M. Cheng. Repeated growth and bubbling transfer of graphene with millimetre-size single-crystal grains using platinum (2012), 699.

72 Cecilia Mattevi, Hokwon Kima and Manish Chhowalla. A Review of Chemical Vapour Deposition of Graphene on Copper. J. Mater. Chem., 21 (2011), 3324-3334.

73 Y. Zhang, Z. Li, P. Kim, L.Y. Zhang, C.W. Zhou. Review of Chemical Vapor Deposition of Graphene and Related Applications. ACS Nano, 6 (2012), 126.

74 S. Gunther, S. Danhardt, B. Wang, M. L. Bocquet, S. Schmitt, and J. Wintterlin. Single Terrace Growth of Graphene on a Metal Surface. Nano Lett., 11 (2011), 1895–1900.

75 W. W. Mullins and R. F. Sekerka. Morphological Stability of a Particle Growing by Diffusion or Heat Flow. J. Appl. Phys., 34 (1963), 323.

76 Luiz Gustavo de Oliveira Lopes Cançado. Raman Spectroscopy Of Nanographites. Universidade Federal de Minas Gerais, 2006.

77 Leandro Malard Moreira. Raman spectroscopy of graphene: probing phonons, electrons and electron-phonon interactions. Universidade Federal de Minas Gerais, 2009.

78 M. S. Dresselhaus R. Saito, G. Dresselhaus. Physical Properties of Carbon Nanotubes. Imperial College Press (1998).

79 N. V. Popov, P. Lambin. Radius and chirality dependence of the radial breathing mode and the G-band phonon modes of single-walled carbon nanotubes. Physical Review B, 73 (2006), 085407.

80 T. M. G. Mohiuddin, A. Lombardo, R. R. Nair, A. Bonetti, G. Savini, R. Jalil, N. Bonini, D. M. Basko, C. Galiotis, N. Marzari, K. S. Novoselov, A. K. Geim, and A. C. Ferrari. Uniaxial strain in graphene by Raman spectroscopy: G peak splitting, Grüneisen parameters, and sample orientation. Phys. Rev. B, 79, 205433.

81 L. Malard, R. Moreira, D. Elias, F. Plentz, E. Alves, M. Pimenta. Thermal enhancement of chemical doping in graphene: a Raman spectroscopy study. J Phys Condens Matter, 22, 33 (2010), 334202.

82 Tim Maitland and Scott Sitzman. Electron Backscatter Diffraction (EBSD) Technique and Materials Characterization Examples. In Scanning Microscopy for Nanotechnology: Techniques and Applications. Springer, 2007.

83 Wolfgang Wisniewski. Crystal Orientations in Glass- Ceramics determined using Electron Backscatter Diffraction (EBSD). Otto-Schott-Institut of the Jena University, 2011.

84 Oxford Instruments, "EBSD," [Online]. Available: http://www.ebsd.com/. [Accessed 2014].

85 César J. Lockhart de la Rosa, Jie Sun, Niclas Lindvall, Matthew T. Cole, Youngwoo Nam, Markus Löffler, Eva Olsson, Kenneth B. K. Teo and August Yurgens. Frame assisted H_2O electrolysis induced H_2 bubbling transfer of

large area graphene grown by chemical vapor deposition on Cu. Appl. Phys. Lett., 102 (2013), 022101.

86 Schwierz Frank. Graphene Transistors. nat. nanotech., 5 (2010).

87 E. H. Hwang, S. Adam, S. Das Sarma. Transport in chemically doped graphene in the presence of adsorbed molecules. Phys. Rev. B, 76 (2007), 195421.

88 Donald A. Neamen. Semiconductor Physics And Devices: Basic Principles. McGraw-Hill, New York, NY, 2003.

89 Alexander V. Klekachev, Amirhasan Nourbakhsh, Inge Asselberghs, Andre L. Stesmans, Marc M. Heyns, and Stefan De Gendt. Graphene Transistors and Photodetectors. The Electrochemical Society Interface (Spring 2013).

90 J. Singh, Electronic and Optoelectronic properties of semiconductor structures. Cambridge University Press, 2007.

91 F. Fratini and F. Guinea. Substrate-limited electron dynamics in graphene. Phys. Rev. B., 77 (2008), 195415-6.

92 F. Giannazzo, V. Raineri, e E. Rimini. Lateral homogeneity of the electronic properties in pristine and ion-irradiated graphene probed by scanning capacitance spectroscopy. Nano. Res. Lett., 6, 1 (2011), 247.

93 R. E. Willians. Gallium Arsenide Processing Techniques. Artech House, 1984.

94 Gang Hee Han, Fethullah Güneş, Jung Jun Bae, Eun Sung Kim, Seung Jin Chae, Hyeon-Jin Shin, Jae-Young Choi, Didier Pribat, and Young Hee Lee. Influence of Copper Morphology in Forming Nucleation Seeds for Graphene Growth. Nano Lett., 11, 10 (2011), 4144–4148.

95 L. M. Malard, J. Nilsson, D. L. Mafra, D. C. Elias, J. C. Brant, F. Plentz, E. S. Alves, A. H. Castro Neto, M. A. Pimenta. Electronic properties of bilayer

graphene probed by Resonance Raman Scattering. Physica Status Solidi. B, Basic Research (2008), p. NA-NA.

96 Kemal Celebi, Matthew T. Cole, Jong Won Choi, Frederic Wyczisk, Pierre Legagneux, Nalin Rupesinghe, John Robertson, Kenneth B. K. Teo, and Hyung Gyu Park. Evolutionary Kinetics of Graphene Formation on Copper. Nano Letters, 13, 3 (2013), pp 967–974.

97 Xuesong Li, Carl W. Magnuson, Archana Venugopal, Rudolf M. Tromp, James B. Hannon, Eric M. Vogel, Luigi Colombo, and Rodney S. Ruoff. Large-Area Graphene Single Crystals Grown by Low-Pressure. J. Am. Chem. Soc., 133 (2011), 2816–2819.

98 F. Ding, H. Ji, Y. Chen, A. Herklotz, K. D€orr, Y. Mei, A. Rastelli, and O. G. Schmidt. Stretchable Graphene: A Close Look at Fundamental Parameters through Biaxial Straining. Nano Lett., 10 (2010), 3453.

99 Xiuli Yin, Yilei Li, Fen Ke, Chenfang Lin, Huabo Zhao, Lin Gan, Zhengtang Luo, Ruguang Zhao, Tony F. Heinz, Zonghai Hu. Evolution of the Raman spectrum of graphene grown on copper upon oxidation of the substrate. Nano Research, 7, 11 (2014), 1613-1622.

100 M. Vanin, J.J. Mortensen, A.K. Kelkkanen, J.M. Garcia-Lastra, K.S. Thygesen, K.W. Jacobsen. Graphene on metals: A van der Waals density functional study. Phys. Rev. B, 81 (2010), 081408.

101 P. Lacovig, M. Pozzo, D. Alfe, P. Vilmercati, A. Baraldi, S. Lizzit. Growth of Dome-Shaped Carbon Nanoislands on Ir(111): The Intermediate between Carbidic Clusters and Quasi-Free-Standing Graphene. Phys. Rev. Lett., 103 (2009), 166101.

102 D. B. Farmer, R. Golizadeh-Mojarad, V. Perebeinos, Y. M. Lin, G. S. Tulevski, J. C. Tsang, P. Avouris. Chemical Doping And Electron-Hole Conduction Asymmetry In Graphene Devices. Nano Lett., 9, 1 (2009), 388-92.

103 J. Moser, A. Barreiro and A. Bachtold. Current-induced cleaning of graphene. Applied Physics Letters, 91 (2007), 163513.

104 Carl W. Magnusona, Xianghua Konga, Hengxing Jia, Cheng Tana, Huifeng Lia, Richard Pinera, Carl A. Ventrice Jr. and Rodney S. Ruoff. Copper oxide as a “self-cleaning” substrate for graphene growth. Journal of Materials Research, 29, 03 (2014), 403-409.

105 T. H. R. Cunha, J. Ek-Weis, R. G. Lacerda and A. S. Ferlauto. Graphene chemical vapor deposition at very low pressure: The impact of substrate surface self-diffusion in domain shape. Appl. Phys. Lett. , 105 (2014), 073104.

106 J. D. Wood, S. W. Schmucker, A. S. Lyons, E. Pop, J. W. Lyding. Effects of polycrystalline cu substrate on graphene growth by chemical vapor deposition. Nano Lett., 11, 11 (2011), 4547-54.

107 P. M. Agrawala, B. M. Rice and D. L. Thompson. Predicting Trends in Rate Parameters for Self-Diffusion on FCC Metal Surfaces. Surface Science, 515 (2002), 21-35.

108 R. Apel, D. Farías, H. Tröger and K. Rieder. He-Diffraction Studies of Hydrogen Chemisorption on Rhodium (311). Surface Science, 331–333 (1995), 57–61.

109 Bert Müller, Lorenz Nedelmann, Bjørn Fischer, Harald Brune, Johannes V. Barth and Klaus Kern. Island Shape Transition in Heteroepitaxial Metal Growth on Square Lattices. Phys. Rev. Lett., 80, 12 (1998).

110 Johannes V. Barth, Giovanni Costantini & Klaus Kern. Engineering atomic and molecular nanostructures at surfaces. Nature, 437 (2005), 671-679.

111 G. Rojas, X. Chen, D. Kunkel, M. Bode, A. Enders. Temperature dependence of metal-organic heteroepitaxy. Langmuir, 27, 23, 14267-71.

112 N. C. Bartelta and K. F. McCartya. Graphene growth on metal surfaces. MRS Bulletin, 37, 12 (2012), pp 1158-1165.

113 V. N. E. Robinson and J. L. Robins Nucleation Kinetics of Gold Deposited onto UHV Cleaved Surfaces of NaCl and KBr. Thin Solid Films, 20 (1974), 155–175.

114 Ivan Vlassiouk, Sergei Smirnov, Murari Regmi, Sumedh P. Surwade, Nishtha Srivastava, Randall Feenstra, Gyula Eres, Chad Parish, Nick Lavrik, Panos Datskos, Sheng Dai, and Pasquale Fulvio. Graphene Nucleation Density on Copper: Fundamental Role of Background Pressure. The Journal of Physical Chemistry C, 117, 37 (2013), 18919-18926.

115 Daniel B. Butrymowicz, John R. Manning, and Michael E. Read. Diffusion in copper and copper alloys - part 1- Volume and surface self-diffusion on copper. Journal of Physical and Chemical Reference Data, 2, 3 (1973), 643-655.

116 H. Bonzel and N. Gjostein. Surface self-diffusion measurements on copper. physica status solidi (b), 25, 1 (1968), 209–222.

117 G. E. Rhead. On Surface Diffusion and the Existence of Two-Dimensional Liquids. Surf. Sci, 15 (1969), 353-357.

118 J. Henrion and G. Rhead. On High surface diffusivities of solid metals in the presence of adsorbed metallic vapours Diffusion Processes. In J. N. Sherwood, A. V. Chadwick, W. M. Muir, and F. L. Swinton, ed., Diffusion Processes. Gordon and Breach, New York, 1971.

119 J. Henrion and G. Rhead. Increase in the surface diffusion of copper Pb alloys as function of Pb vapor Pressure. Evidence of Surface Melting. C. R. Acad. Sci., B 267 (1968), 958-961.

120 Norman Hackerman and Norman H. Simpson. Rates of surface self-diffusion over the principal planes of a single crystal of copper. Trans. Faraday Soc, 52 (1956), 628-633.

121 N. A. Gjostein, Measurement of surface diffusion coefficient of copper by thermal grooving technique. Trans. Metall. Soc. AIME, 221 (1961), 1039-1046.

122 H. P. Bonzel. A surface diffusion mechanism at high temperature. Surf. Sci., 21 (1970), 45-60.

123 V. T. Binh and P. Melinon. On viscous mechanism for surface diffusion at high temperatures (T/Tm > 0.75) due to formation of a 2D dense fluid on metallic surfaces. Surf. Sci., 161 (1985), 234-244.

124 L.L. Suni, E.G. Seebauer. A new physical picture for surface diffusion at high temperatures. Surf. Sci., 301 (1994), L235-L238.

125 P.D. Ditlevsen, P. Stoltze and J.K. Norskov. Anharmonicity and disorder on the Cu(110) surface. Phys. Rev. B, 44 (1991), 13002.

126 M. Karimi, T. Tomkowski, G. Vidali and O. Biham. Diffusion of Cu on Cu Surfaces. Phys. Rev. B, 52 (1995), 5364.

127 Yufeng Hao, M. S. Bharathi, Lei Wang, Yuanyue Liu, Hua Chen, Shu Nie, Xiaohan Wang, Harry Chou, Cheng Tan, B. Fallahazad, H. Ramanarayan, Carl W. Magnuson, Emanuel Tutuc, B. I. Yakobson, K. F. McCarty, Yong-Wei Zhang, P. Kim, J. Hone, L. Colombo, R. Ruoff. The Role of Surface Oxygen in the Growth of Large Single-Crystal Graphene on Copper. Science, 342, 6159 (2013), 720-723.

128 A. Pimpinelli, I. Elkinani, A. Karma, C. Misbah and J. Villain. Step motions on high-temperature vicinal surfaces. J. Phys. Condens. Matter, 6 (1994), 266-2680.

129 F. Delamare, G. E. Rhead. Increase in the surface self-diffusion of copper due to the chemisorption of halogens. Surface Science, 28, 1 (1971), 267–284.